國立臺灣大學電機資訊學院電信工程學研究所

博士論文

Graduate Institute of Communication Engineering
College of Electrical Engineering and Computer Science
National Taiwan University
Doctoral Dissertation

基於多鐵性材料之 GHz 頻段電氣小天線之設計與實驗驗證及其操作機制之探究

Design, Experimental Validation, and Operational Mechanism Investigation of GHz-Band Electrically Small Antennas Based on Multiferroic Materials

許瑞福

Rui-Fu Xu

指導教授：陳士元 博士

Advisor: Shih-Yuan Chen, Ph.D.

中華民國 114 年 5 月

May, 2025

doi:10.6342/NTU202501094

國立臺灣大學博士學位論文
口試委員會審定書
DOCTORAL DISSERTATION ACCEPTANCE CERTIFICATE
NATIONAL TAIWAN UNIVERSITY

（論文中文題目）(Chinese title of Doctoral Dissertation)

基於多鐵性材料之 GHz 頻段電氣小天線之設計與實驗驗證及其操作機制之探究

（論文英文題目）(English title of Doctoral Dissertation)

Design, Experimental Validation, and Operational Mechanism Investigation of GHz-Band Electrically Small Antennas Based on Multiferroic Materials

本論文係許瑞福(姓名) d09942001（學號）在國立臺灣大學電信工程學研究所完成之博士學位論文，於民國 114 年 5 月 7 日承下列考試委員審查通過及口試及格，特此證明。

The undersigned, appointed by the Graduate Institute of Communication Engineering on Seventh (date) May (month) 2025 (year) have examined a Doctoral Dissertation entitled above presented b Rui-Fu Xu (name) d09942001 (student ID) candidate and hereby certify that it is worthy of acceptance.

口試委員 Oral examination committee:

陳士元
（指導教授 Advisor）

吳文中

劉建豪

李尉彰

所長 Director: 魏宏宇

doi:10.6342/NTU202501094

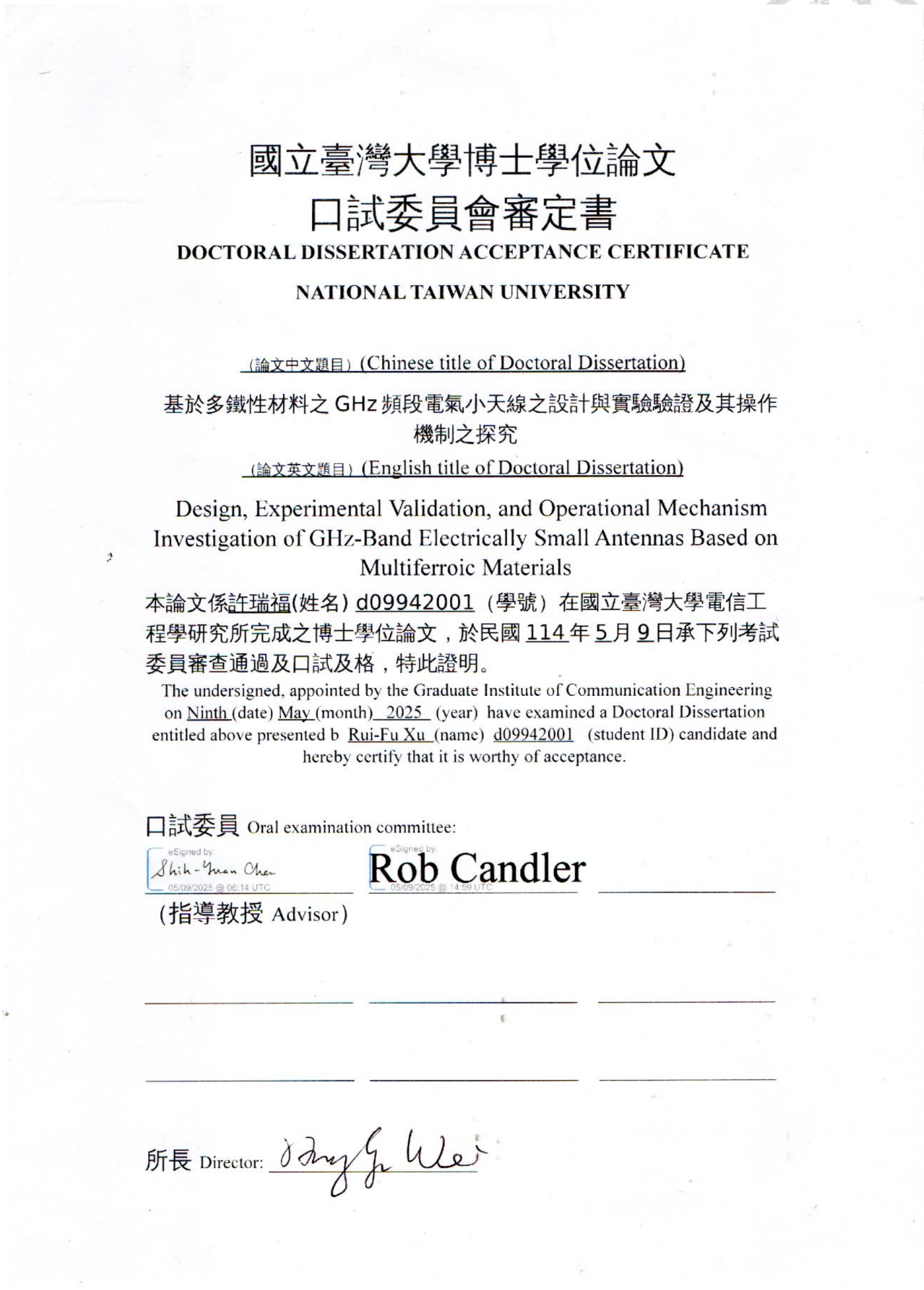

國立臺灣大學博士學位論文
口試委員會審定書

DOCTORAL DISSERTATION ACCEPTANCE CERTIFICATE

NATIONAL TAIWAN UNIVERSITY

（論文中文題目）(Chinese title of Doctoral Dissertation)

基於多鐵性材料之 GHz 頻段電氣小天線之設計與實驗驗證及其操作機制之探究

（論文英文題目）(English title of Doctoral Dissertation)

Design, Experimental Validation, and Operational Mechanism Investigation of GHz-Band Electrically Small Antennas Based on Multiferroic Materials

本論文係許瑞福(姓名) d09942001（學號）在國立臺灣大學電信工程學研究所完成之博士學位論文，於民國 114 年 5 月 9 日承下列考試委員審查通過及口試及格，特此證明。

The undersigned, appointed by the Graduate Institute of Communication Engineering on Ninth (date) May (month) 2025 (year) have examined a Doctoral Dissertation entitled above presented b Rui-Fu Xu (name) d09942001 (student ID) candidate and hereby certify that it is worthy of acceptance.

口試委員 Oral examination committee:

eSigned by: Shih-Yuan Chen 05/09/2025 @ 06:14 UTC

eSigned by: Rob Candler 05/09/2025 @ 14:59 UTC

（指導教授 Advisor）

所長 Director:

doi:10.6342/NTU202501094

誌謝

能完成這個研究真的非常非常不容易，一路走來不知道有多少個難熬的孤獨歲月，我總是不斷告訴我自己要努力堅持下去直到完成為止。這個題目在我碩士班2016 年時，全世界還沒有任何的實驗數據，要在如一片漆黑伸手不見五指的嶄新領域探索題目，真的是需要極大的熱忱和勇氣。因此我想好好謝謝我自己，一路走來都沒有放棄，不管面對再多的未知始終願意繼續走下去。然後我衷心地感謝我的指導教授陳士元老師、UCLA 的 Rob Candler 教授，是他們讓我得以自由且富有想像力地探索多鐵性天線材料的這個題目。若沒有他們的鼓勵和引導，我不可能開始也無法完成這一份研究。我想感謝我的家人，是他們的支持和包容，讓我得以安心地完成博士班的學業，能夠在這個年紀放心地衝刺學術研究是一種不可多得的奢侈。我特別想好好感謝在博士班尾聲，在我面臨人生低潮時不斷鼓勵我的女朋友令昀，在我失去信心和勇氣迷失方向的時候，是妳的笑容和陪伴讓我能繼續走下去。我也想感謝我的實驗室同學好朋友們，包含慕召、昀廷、士銘、聖偉、Louis、欣融、士允，和你們一起做事情、討論研究、出去玩和吃飯，真的很快樂很美好，你們真的都是有能力又無私願意付出做事情的好夥伴。最後我也想感謝我的學術合作夥伴韋廷、Sidhant、Jackie，能夠有這些跨領域國內外的合作，不管是製程、實驗還是理論上的討論，沒有你們的幫助我也無法完成這些研究，謝謝你們。

doi:10.6342/NTU202501094

中文摘要

多鐵性材料因其獨特的磁電耦合特性，在GHz頻段微型化天線設計深具應用潛力。本論文探討多鐵性天線的設計、開發與性能表現，最後得到的實驗結果與既有的理解與理論預測迥異。本研究的主要貢獻在於提供一個全新的實驗觀點，挑戰既有的假設與研究結論，進一步開啟對多鐵性天線輻射機制深入探討之可能性。論文中，我們首先回顧了電氣小天線(ESA)的基本理論，包括其理論限制、頻寬與效率之間的權衡，及其在生醫遙測與軍事通訊等領域之應用。ESA設計的主要挑戰在於如何克服尺寸縮小、頻寬及輻射效率之間的折衷，為了解決此問題，近年來學界提出一種新型機械驅動天線，稱為「機械天線」。這類天線透過機械運動來產生電磁輻射，而非依賴傳統的電流驅動機制，提供了一種可接近天線效能理論極限的新方法。然而，在GHz頻段實現機械激發仍面臨挑戰，因此需要尋求替代策略多鐵性天線。本論文進一步介紹以體聲波為驅動機制的多鐵性天線，這類天線利用壓電-磁致伸縮複合結構，在GHz頻率範圍內實現機械共振，若結合鐵磁性共振，這種設計能有效降低歐姆損耗並進而提升電磁輻射效率。最後，我們的實驗結果表明，相較於以往的研究成果，多鐵性天線在GHz頻段展現出根本性的差異，顯示出磁電輻射機制仍有待進一步深入探討，以利推動未來的研究發展。

ABSTRACT

Multiferroic materials have emerged as a promising solution for antenna miniaturization in GHz-band applications, leveraging their unique magnetoelectric coupling properties. This dissertation explores the design, development, and performance of multiferroic antennas. Our experimental results presented herein are among the few existing experimental verifications in the open literature, and they represent entirely new findings that differ significantly from existing theoretical predictions and understanding. The key contribution of this work lies in presenting a new experimental perspective that challenges prevailing assumptions and established conclusions, thereby paving the way for deeper inquiry into the underlying mechanisms of radiation from multiferroic antennas.

The thesis begins with a review of electrically small antenna (ESA) fundamentals, including their theoretical limitations, bandwidth-efficiency constraints, and various practical applications in biomedical telemetry and military communications. A key challenge in ESA design is overcoming the inherent trade-off between size, bandwidth, and radiation efficiency. To address this, a new class of mechanically actuated antennas, known as “mechtennas,” was proposed. These antennas generate electromagnetic radiation through mechanical motion rather than conventional current-based mechanisms, offering a novel approach to approaching the Chu’s limit.

Yet, GHz-frequency actuation remains a challenge, necessitating alternative strategies, such as strain-mediated antennas. The dissertation introduces bulk acoustic wave (BAW)-driven multiferroic antennas, which utilize a piezoelectric-magnetostrictive composite structure to achieve resonances at GHz frequencies. The design allows for efficient electromagnetic radiation with reduced ohmic losses. Finally, our experimental

validation reveals that multiferroic antennas demonstrate fundamental differences in the GHz band compared to the previous findings. These findings call for further investigation into the underlying mechanism of magnetoelectric radiation in the future.

CONTENTS

doi:10.6342/NTU202501094

LIST OF FIGURES

doi:10.6342/NTU202501094

doi:10.6342/NTU202501094

doi:10.6342/NTU202501094

doi:10.6342/NTU202501094

doi:10.6342/NTU202501094

doi:10.6342/NTU202501094

LIST OF TABLES

doi:10.6342/NTU202501094

LIST OF SYMBOLS

T	Stress tensor	d	Thickness or corresponding resonance dimensions
S	Strain tensor	Q_s	Quality factor at series resonance
c	Elastic stiffness coefficient	Q_p	Quality factor at parallel resonance
s	Elastic compliance coefficient	ϕ	Z parameter phase
D	Electric displacement	S_{11}	Reflection coefficient
E	Electric field	P_{inc}	Incident power
ε	Permittivity	k_{eff}	Effective coupling coefficient
u	Displacement vector	M_r	Remanent magnetization
L_m	Motional inductance	H_c	Coercive field
C_m	Motional capacitance	H_{sat}	Saturating field
C_0	Static capacitance	M_s	Saturation magnetization
f_s	Series resonance frequency	$\bar{m}$	Spin magnetic moment
f_p	Parallel resonance frequency	$\hbar$	Planck's constant divided by 2π
v_a	Phase velocity of a propagating wave	q	Electron charge
k	Wavenumber	m_e	Electron mass
ω	Angular frequency	$\bar{s}$	Spin angular momentum
ρ	Density	γ	Gyromagnetic ratio
v_o	Stiffened phase velocity	$\bar{H}$	Magnetic field
K	Piezoelectric coupling constant	$\bar{\tau}$	Torque
k_t	Electromechanical coupling	μ_0	Vacuum magnetic permeability

	coefficient
$\overline{M}$	Total magnetization
χ	Susceptibility tensor
μ	Permeability tensor
f_0	Larmor frequency
α	Magnetic damping factor
ΔH	Magnetic linewidth
λ_{si}	Saturation magnetostriction measured from its ideal demagnetized state
λ_{θ}	Saturation magnetostriction at an angle θ relative to the direction of magnetization
k_H	Magnetomechanical coupling figures of merits

Chapter 1 Introduction

1.1 Definition of Electrically Small Antennas

Antenna miniaturization has been a central topic in antenna design and related fields. Since early days, the demand for compact and versatile antennas has continually increased. Today's multifunctional systems further intensify this demand, as devices such as cell phones, portable wireless devices, and both short- and long-range communication modules all benefit from smaller antenna footprints. Additionally, compact antennas are essential for data transmission and navigation systems, highlighting the ongoing challenge for researchers to develop smaller, more functional antennas as wireless technology advances.

Throughout the thesis, I will refer to these miniaturized designs as "electrically small antennas" (ESAs), indicating that they are significantly smaller than the electromagnetic wavelength of the frequency they operate at [1]. The concept of an ESA was introduced by Wheeler and Chu, who defined it as an antenna with a maximum dimension smaller than half a wavelength, referred to as a radian-length [2],[3]. A common definition for an ESA is based on the condition: $ka < 0.5$, where k is the wavenumber $2\pi/\lambda$, and a is the radius of the smallest sphere (the "Chu sphere") that encloses the antenna, as shown in Fig. 1.1. Typically, ESAs behave like a Hertzian dipole and exhibit radiation efficiency

doi:10.6342/NTU202501094

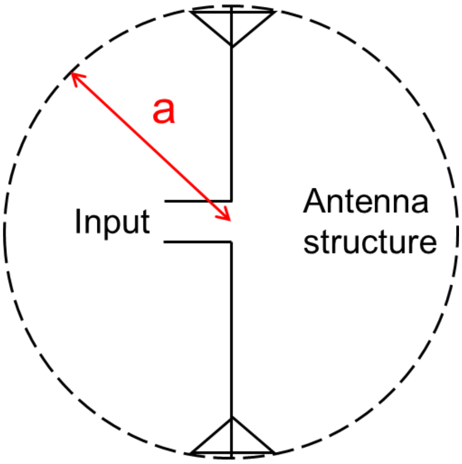

Fig. 1.1. Antenna within a sphere of radius *a* [3].

as well as bandwidth that tend to decrease with electrical size ka length. In this chapter, the background and motivation of ESAs research will be reviewed. The new type of ESAs, mechanical antennas, will be introduced at the end of this chapter. Among various types of mechanical antennas, multiferroic antennas, which are the core contribution of this dissertation, show great potential in applications within and beyond ultra high frequency (300 MHz to 3 GHz, UHF) band applications.

1.2 Applications for Electrically Small Antennas

The demand for antenna miniaturization is driven by diverse applications. These applications range from very low frequency (3 kHz to 30 kHz, VLF) band to UHF band. In this chapter, I will review applications of interest of ESAs, including biomedical antennas and military communications.

One of the important applications of ESAs lies in the biomedical engineering. The recent progress in microelectromechanical systems (MEMS) and microfluidics, combined with the continual miniaturization of electronic technologies, has catalyzed transformative innovations. These advances have broadened the horizons of medical practice, clinical research and wellness monitoring applications. Beyond the capacity to monitor critical diagnostic metrics—such as endoscopic imaging, temperature, pressure, pH, and glucose levels—state-of-the-art biotelemetry encompasses sophisticated in-body systems, including brain-machine interfaces, visual prostheses, cardiac pacemakers, defibrillators, precision drug delivery mechanisms, and hyperthermic therapeutic devices [4].

Biomedical devices, particularly implantable medical devices, often operate in frequency bands such as the Industrial, Scientific, and Medical (ISM) band and the Medical Radio (MedRadio) band, with specific considerations for their design and functionality. The ISM band at 2.45 GHz and the MedRadio band between 401 and 406 MHz are commonly used for medical telemetry to transmit power through biological tissues. These frequency ranges have led to the need for heavily miniaturized antennas, given that the free-space wavelength in the MedRadio band is approximately 74 cm, while in the ISM band, it is around 12 cm. For implantable devices, typical dimensions range from 1 to 10 mm in diameter and from 5 to 35 mm in length to ease surgical implantation. Hence, this size constraint necessitates the design of electrically small antennas (ESAs) with dimensions that are fractions of the free-space wavelength, typically $\lambda_0/30$ for the MedRadio band and $\lambda_0/5$ for the ISM band [5].

In addition to the inherently electrically small characteristics, the unique environment of implantable antennas—surrounded by biological tissue—shifts the primary design focus from bandwidth and radiation efficiency to the power transmission efficiency through the host body. To achieve effective performance, antenna designs must account for the high dielectric constant of tissues, which concentrates the near field

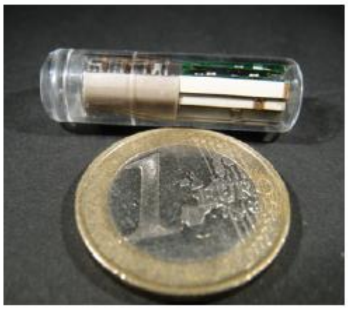

Fig. 1.2. Dual band spiral antenna integrated with circuitry inside a capsule. Reproduced from [5].

around the antenna while minimizing power losses [5].

A representative implantable device consists of a cylindrical module with a 10 mm diameter and a height of 32 mm, encapsulated in a biocompatible shell. Inside, it houses electronic components, a power source, a sensor, and an antenna, as illustrated in Fig. 1.2. The communication system operates on the MedRadio band (401–406 MHz) for data transmission and the ISM band (2.45 GHz) for wake-up signals. Simulations indicate a gain of -17.5 dB in the ISM band and -29.4 dB in the MedRadio band.

This device, incorporating a temperature sensor, was evaluated in a pig model to monitor post-surgical temperature variations after a graft procedure using autologous stem cells. Two implants were positioned—one just beneath the skin and another embedded 30 mm deep within muscle tissue. The system successfully maintained telemetry over a 10-meter range, ensuring reliable data transmission without disrupting the medical study [5].

Radiation into lossy media, such as biological tissues, has parallels to studies in underwater communication and communication over lossy ground. When an antenna radiates into a lossy medium like the sea water, the radiation intensity depends on the radial coordinate through the term $exp(2\alpha r)$, which α stands for attenuation constant and r represents distance to the origin, making the resulting radiation pattern highly

doi:10.6342/NTU202501094

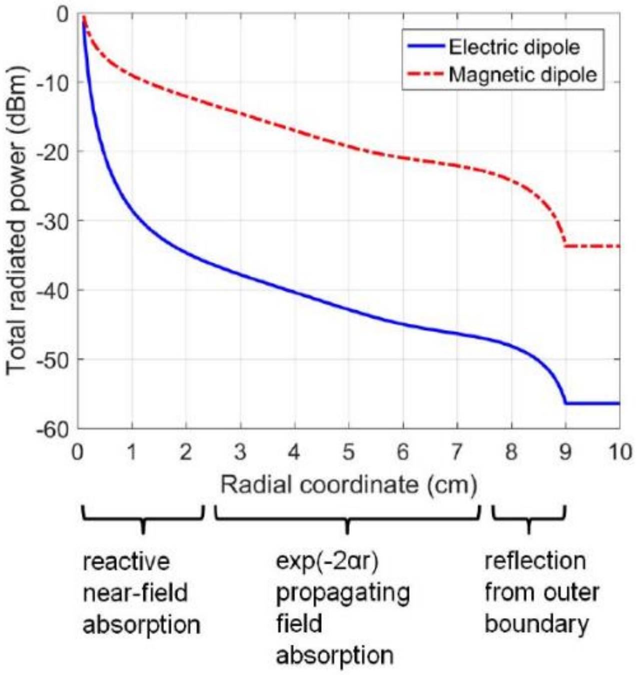

Fig. 1.3. The total radiated power from an electric or magnetic source positioned at the center of a phantom, measured as it exits a spherical boundary with a radius r (radial coordinate), is calculated at a frequency of 403 MHz. Reproduced from [6].

sensitive to the choice of the origin of the coordinate system. For implantable antennas, defining the frequency bandwidth based solely on a low input reflection coefficient has limited relevance because a low reflection coefficient does not guarantee effective power radiation; much of the power could be dissipated within the host body [6]. The radiation properties of an implantable antenna are influenced not only by the antenna itself but also by the shape, dimensions, and composition of the host body. The critical performance metric for such antennas is the amount of power that successfully exits the body. As shown in Fig. 1.3, loss mechanisms in this context can be divided into three categories: near-field losses caused by coupling with the lossy biological tissue surrounding the implant, losses from the field propagating through the body and reflection losses at the interface between the body and free space. While the last two are inevitable for transmitting signals to free space, minimizing the first type of loss is crucial for optimizing antenna performance [6].

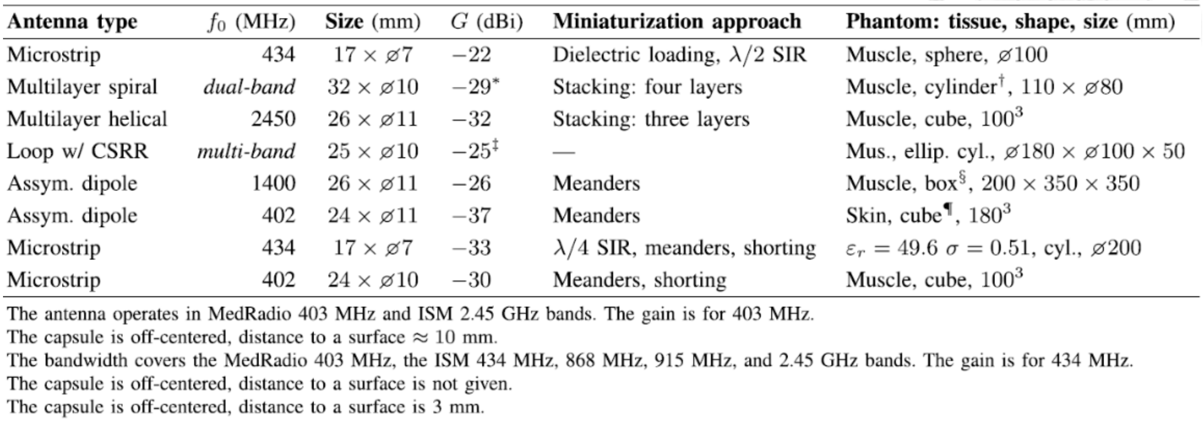

Antenna type	f_0 (MHz)	**Size** (mm)	G (dBi)	**Miniaturization approach**	**Phantom: tissue, shape, size** (mm)
Microstrip	434	$17 \times \varnothing 7$	-22	Dielectric loading, $\lambda/2$ SIR	Muscle, sphere, $\varnothing 100$
Multilayer spiral	*dual-band*	$32 \times \varnothing 10$	-29^*	Stacking: four layers	Muscle, cylinder†, $110 \times \varnothing 80$
Multilayer helical	2450	$26 \times \varnothing 11$	-32	Stacking: three layers	Muscle, cube, 100^3
Loop w/ CSRR	*multi-band*	$25 \times \varnothing 10$	$-25^\ddagger$	—	Mus., ellip. cyl., $\varnothing 180 \times \varnothing 100 \times 50$
Assym. dipole	1400	$26 \times \varnothing 11$	-26	Meanders	Muscle, box§, $200 \times 350 \times 350$
Assym. dipole	402	$24 \times \varnothing 11$	-37	Meanders	Skin, cube¶, 180^3
Microstrip	434	$17 \times \varnothing 7$	-33	$\lambda/4$ SIR, meanders, shorting	$\varepsilon_r = 49.6$ $\sigma = 0.51$, cyl., $\varnothing 200$
Microstrip	402	$24 \times \varnothing 10$	-30	Meanders, shorting	Muscle, cube, 100^3

The antenna operates in MedRadio 403 MHz and ISM 2.45 GHz bands. The gain is for 403 MHz.
The capsule is off-centered, distance to a surface $\approx$ 10 mm.
The bandwidth covers the MedRadio 403 MHz, the ISM 434 MHz, 868 MHz, 915 MHz, and 2.45 GHz bands. The gain is for 434 MHz.
The capsule is off-centered, distance to a surface is not given.
The capsule is off-centered, distance to a surface is 3 mm.

Fig. 1.4. Comparison between miniaturized biomedical antennas. Reproduced from [4].

Since biological tissue significantly influences impedance matching and radiation patterns, it is necessary for antenna designs that remain resilient to environmental variations. For example, in [4] the author addressed this challenge by developing an ultraminiature 434 MHz antenna designed to withstand impedance detuning caused by the diverse electromagnetic properties of surrounding biological environments. Their approach involved differentiating regions based on their dielectric properties and establishing tailored matching standards. The specified impedance robustness constraints include $|S_{11}| < -10$ dB for maximum electromagnetic (EM) properties, $|S_{11}| < -3$ dB for minimum EM properties, and $|S_{11}| < -10$ dB across the remaining EM range. To achieve these specifications, they designed an antenna enclosed within a 17 mm × 7 mm insulating capsule. This design possesses a realized gain of −22 dBi within a muscle phantom, with comparative chart presented in Fig. 1.4 [4]. The biomedical ESAs' show common realized

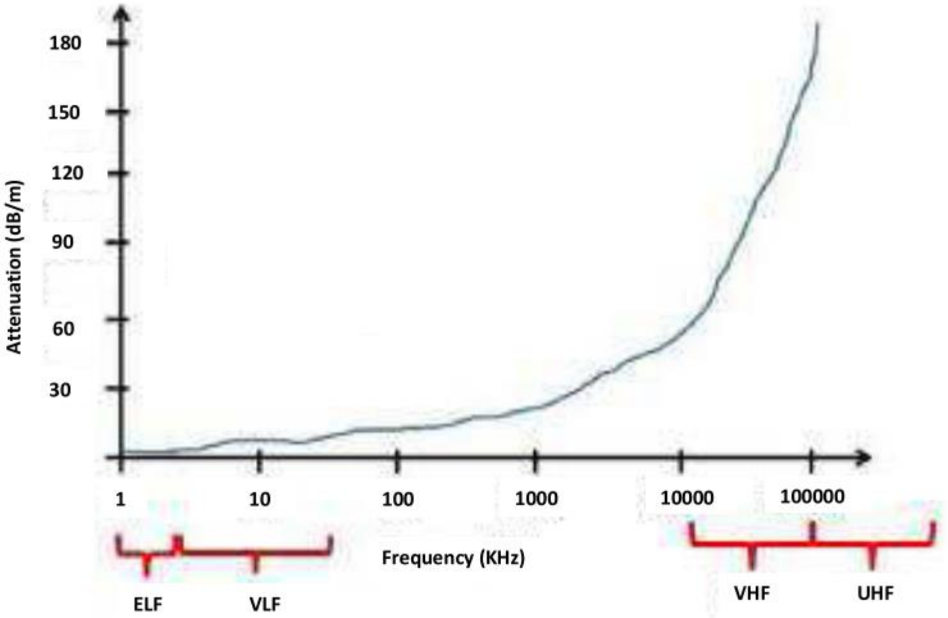

Fig. 1.5. Attenuation constant for sea water in different frequency bands. Reproduced from [8].

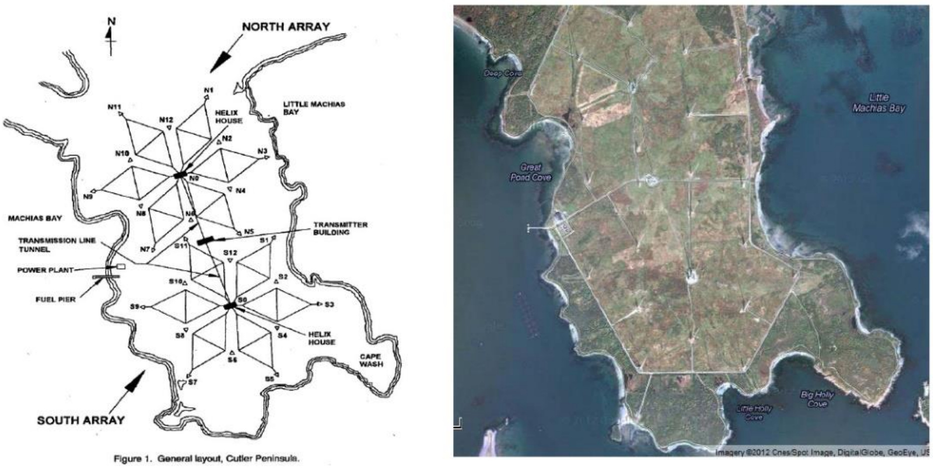

Fig. 1.6. Antenna configurations at Cutler Peninsula. Reproduced from [9].

gain located in the range between -20 dBi to -40 dBi.

In addition to the high-frequency commercial applications for ESAs, low-frequency communications using ESAs are also widely discussed for military purposes. These include various forms of low-frequency communications, such as transcontinental communication utilizing the ionosphere. Ionospheric low-frequency communication specifically involves the use of very low-frequency (3 kHz to 30 kHz, VLF) and low-

doi:10.6342/NTU202501094

Fig. 1.7. 26 towers 850 to 1000 ft height. Reproduced from [9].

frequency (30 kHz to 300 kHz, LF) electromagnetic waves, which leverage the ionosphere's reflective properties. This atmospheric layer, situated approximately 60 to 1,000 kilometers above the Earth's surface, contains charged particles (ions and electrons) capable of reflecting and refracting radio waves. This characteristic enables reliable long-distance communication without the need for satellites [7].

Another significant advantage of low-frequency electromagnetic waves is their ability to penetrate lossy mediums such as soil, seawater, and caves. This makes them particularly valuable for underwater communication, as shown in Fig. 1.5 [8]. For instance, the Cutler transmitter operates at 24 kHz and facilitates one-way coded text message communication with submarines. However, the use of low-frequency communication comes with challenges. The large free-space wavelength necessitates massive infrastructure; for example, the Cutler transmitter spans an entire peninsula and consumes enormous amounts of power (see Fig. 1.6 and Fig. 1.7). These challenges have driven ongoing efforts to develop more efficient solutions, including electrically small antennas optimized for low-frequency communication, to reduce infrastructure size and energy consumption [9].

doi:10.6342/NTU202501094

1.3 Theoretical Limits in Miniaturization Theory

This section provides an overview of fundamental theoretical limits in antenna miniaturization. Before the end of the chapter, current state-of-the-art progress of antenna miniaturization will also be discussed. The basic concept of emerging ESAs, mechanical antennas as well as multiferroic antennas, will also be introduced.

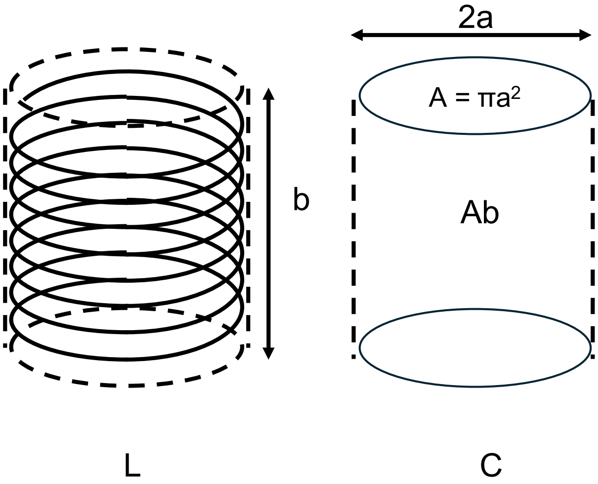

Fig. 1.8. Small electric dipole resembles a capacitor, and small magnetic dipole resembles a loop inductor. The two dipoles occupy the same volume [2].

The study of small antennas began with Wheeler's pioneering work in 1947 [2]. He explored the fundamental constraints on small antennas by developing a simple model that represented them using lumped capacitance or inductance alongside a radiation resistance. To better understand the relationship between antenna size and radiation characteristics, Wheeler introduced the concept of the radiation power factor (RPF)—the ratio of radiated power to reactive power [2]. He observed that as antennas decrease in size, there is an inherent limitation on bandwidth, concluding that RPF is directly proportional to the antenna’s physical volume, as shown in Fig 1.8. This concept of RPF was, in essence, an early version of what is now commonly referred to as Q, which is the

doi:10.6342/NTU202501094

inverse of the power factor in Wheeler's model and links RPF to bandwidth for small antennas.

However, Wheeler's approach was an approximation that held only for very small antennas, as it did not account for the influence of radiated spherical modes that become more significant as antenna size increases. Despite its limitations, Wheeler's work represented the first in-depth exploration of small antennas, inspiring numerous researchers to investigate the fundamental principles and limitations he proposed. His findings advanced both theoretical understanding and the practical development of small antennas [1].

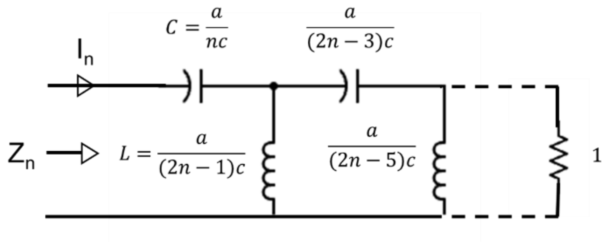

Fig. 1.9. Equivalent circuit representing TM_{n0} spherical mode. If n=1, the circuit becomes a small electric dipole. With higher order modes, more energy is stored in the capacitor and inductor, which is equivalent to the effect of more reactive near field being stored [3].

In 1948, Chu expanded on these ideas by calculating the minimum achievable Q for an omnidirectional antenna enclosed within a "Chu sphere" (refer to Fig. 1.1). Chu used spherical mode wavefunction expansions outside this mathematical boundary to express the radiated field as a sum of spherical modes. Each mode was represented through an equivalent circuit, enabling him to determine the Q of each mode through circuit analysis. Although Chu's focus was on a specific type of omnidirectional antenna, his work set a foundation for future studies that further refined these theoretical limits [3].

doi:10.6342/NTU202501094

After Chu's work, many researchers pursue more rigorous limitations between quality factor, Q, and electrical size of the ESAs. A generally accepted lower limit of Q can be expressed as the following relations:

$$Q > \frac{1}{(ka)^3} + \frac{1}{ka} \tag{1.1}$$

This equation reveals that for electrical size $ka << 1$, the cubic term of $1/ka$ will dominate the lower bound of Q. Hence, it will make Q inevitably high; while for electrical size $ka > 1$, the linear term $1/ka$ will slowly decrease the lower bound of Q as the size becomes larger. It basically states that ESAs will inevitably possess high quality factor and narrow bandwidth. In 1996, McLean revisited Chu's limit and derived it in a more concise manner [10]. To start with, quality factor can be commonly defined as:

$$Q = \begin{cases} \dfrac{2\omega W_e}{P_{rad}}, W_e > W_m \\ \dfrac{2\omega W_m}{P_{rad}}, W_m > W_e \end{cases} \tag{1.2}$$

, where W_e is the time-average, non-propagating stored electric energy, W_m is the time-average, non-propagating stored magnetic energy, ω is the radian frequency and P_{rad} is the radiated power. This formula already excludes any form of losses with purely real input impedance. Then, McLean writes the fields of TM_{01} spherical mode, which is the same as a short electric linear dipole:

$$A_r = -\cos\theta\, e^{-jkr}\left(1 - \frac{j}{kr}\right) \tag{1.3}$$

$$H_\phi = \sin\theta\, e^{-jkr}\left(\frac{j}{kr^2} - \frac{1}{r}\right) \tag{1.4}$$

$$E_\theta = \frac{1}{j\omega\epsilon}\sin\theta\, e^{-jkr}\left(-\frac{1}{r^2} - \frac{jk}{r} + \frac{j}{kr^3}\right) \tag{1.5}$$

doi:10.6342/NTU202501094

$$E_r = \frac{1}{\omega\epsilon} 2\cos\theta \, e^{-jkr} \left(\frac{1}{kr^3} + \frac{j}{r^2} \right) \tag{1.6}$$

These fields are root-mean-square (RMS) values. The electric and magnetic energy densities w_e and w_m is:

$$\begin{aligned} w_e &= \frac{1}{2}\epsilon \, \vec{E} \cdot \vec{E}^* \\ &= \frac{1}{2}\epsilon \left(|E_r|^2 + |E_\theta|^2 \right) \\ &= \frac{1}{2\omega}\eta[\sin^2\theta \left(\frac{1}{k^3r^6} - \frac{1}{kr^4} + \frac{k}{r^2} \right) \\ &\quad + 4\cos^2\theta \left(\frac{1}{k^3r^6} + \frac{1}{kr^4} \right)] \end{aligned} \tag{1.7}$$

$$\begin{aligned} w_m &= \frac{1}{2}\mu \, \vec{H} \cdot \vec{H}^* \\ &= \frac{1}{2}\mu \left(\left| H_\phi \right|^2 \right) \\ &= \frac{1}{2}\mu \sin^2\theta \left(\frac{1}{k^2r^4} + \frac{1}{r^2} \right) \end{aligned} \tag{1.8}$$

, where $\eta_i = \sqrt{\frac{\mu}{\epsilon}}$. Next, we consider only propagating term E_θ and H_ϕ. They compose propagating electric energy density, w_e^{rad}:

$$H_\phi^{rad} = -\sin\theta \frac{e^{-jkr}}{r} \tag{1.9}$$

$$E_\theta^{rad} = -\eta_i \sin\theta \frac{e^{-jkr}}{r} \tag{1.10}$$

$$w_e^{rad} = \frac{1}{2}\epsilon |E_\theta^{rad}|^2 = \frac{{\eta_i}^2}{r^2} \sin^2\theta \tag{1.11}$$

We can subtract (1.7) by (1.11), which means that the total energy density subtracts propagating energy density. This will be the term representing non-propagating energy density $w_e' = w_e - w_e^{rad}$. Then, we can integrate this term over the entire region outside

doi:10.6342/NTU202501094

the sphere. The total non-propagating stored electric energy:

$$W_e' = \frac{4\pi\eta_i}{3\omega}\left[\frac{1}{k^3a^3} + \frac{1}{ka}\right] \tag{1.12}$$

The total radiated power can be obtained by integrating real part of the Poynting vector over the spherical surface:

$$\begin{aligned} P_{rad} &= \int_0^{2\pi}\int_0^{\pi} Re\left(\vec{E} \times \vec{H}^*\right) \cdot \widehat{a_r} r^2 \sin\theta \, d\theta d\phi \\ &= \frac{8\pi}{3}\eta_i \end{aligned} \tag{1.12}$$

Finally, the Q can be determined:

$$Q = \frac{2\omega W_e'}{P_{rad}} = \frac{1}{k^3a^3} + \frac{1}{ka} \tag{1.13}$$

This equation is also called Wheeler-Chu or Chu’s limit.

In 2012, D. F. Sievenpiper gives a comprehensive review of Chu’s limit validation [11]. He begins with the definition of bandwidth-efficiency product. The bandwidth B can be linked to quality factor Q by the work of A. D. Yaghjian and S. R. Best in [14]:

$$B \cong \frac{1}{Q}\left(\frac{s-1}{\sqrt{s}}\right) \tag{1.14}$$

, where s stands for maximum allowable voltage standing wave ratio VSWR. By assuming an ideal lossless antenna, the efficiency is equal to 1. Then, inserting lower limit Q (1.13) into (1.14) and assuming VSWR or s to be 2, the upper limit of bandwidth-efficiency product can be described as:

$$B\eta = \frac{1}{\sqrt{2}}\left(\frac{1}{ka} + \frac{1}{k^3a^3}\right)^{-1} \tag{1.15}$$

(1.15) can also be extended to include circularly polarized or dual-mode antennas:

$$B\eta = \frac{1}{\sqrt{2}}\left(\frac{1}{ka} + \frac{1}{2k^3a^3}\right)^{-1} \tag{1.16}$$

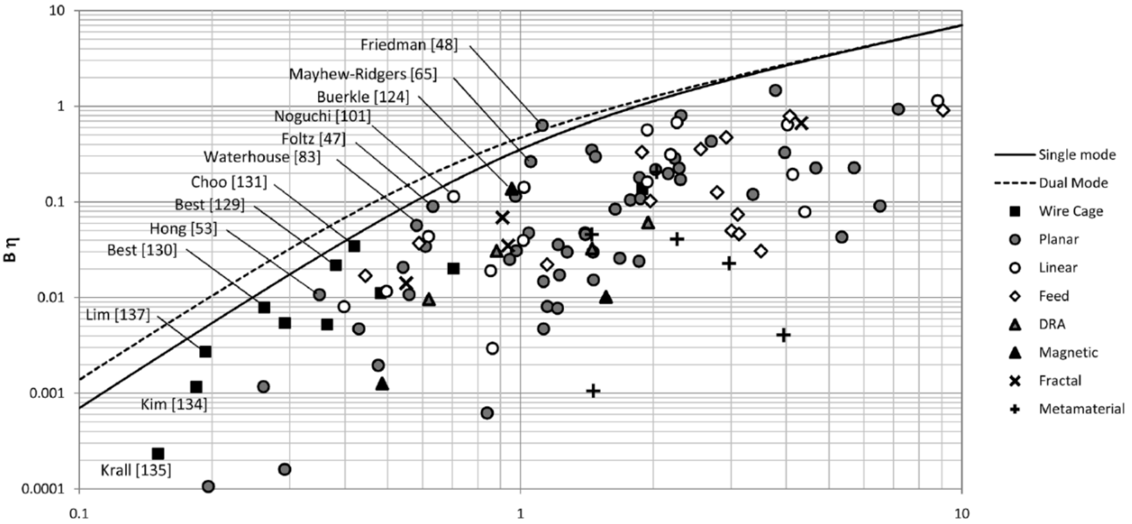

Fig. 1.10. The measured bandwidth efficicnecy product versus electrical size ka. The upper limit is plotted by (1.15) and (1.16). Reproduced from [11].

Reference [11] analyzes the theoretical performance limits of various antenna designs using equations (1.15) and (1.16) and compares them with existing designs up to 2010, as illustrated in Figure 1.10. The antennas are categorized based on the classification system given in [11]. Designs incorporating a ground plane, such as patch antennas and planar inverted-F antennas (PIFAs), with a width greater than their height, fall under the "Planar" category. Structures resembling dipoles, including those exhibiting dipole-like modes on metal surfaces regardless of aspect ratio, are classified as "Linear." A subset of linear antennas, labeled "Feed" antennas, consists of compact resonant structures that excite larger ground planes, often found in mobile devices. Other notable categories include dielectric resonator antennas (DRAs) and antennas utilizing materials with relative permeability μ_r>1, grouped as "Magnetic." Traditional high-performance designs featuring intricate wire structures with near-spherical shapes are classified as "Wire Cage," while modern antenna concepts leveraging "Fractal" or "Metamaterial" principles form another distinct category.

Key observations from Figure 1.10 regarding antenna performance include the following:

1. No electrically small antenna has exceeded the theoretical performance limit.
2. The theoretical limit reliably predicts the maximum achievable bandwidth, even for antennas with moderate to large electrical sizes.
3. Wire cage antennas offer a clear performance advantage for electrically small designs.
4. Standard planar and linear antennas can approach the theoretical limit when designed for moderate electrical sizes.
5. Dielectric resonator antennas, as expected, exhibit poor performance due to their dependence on high-dielectric materials.
6. Magnetic antennas theoretically outperform other designs by a factor of three, but they remain underutilized. One particular design shows promising results, indicating a potential research opportunity if low-loss magnetic materials become viable.
7. Despite their popularity, fractal and metamaterial-based antennas do not demonstrate a significant performance advantage over conventional designs [11].

These observations lead to important conclusions about antenna performance and its relationship with established design principles. High-performing wire cage designs align with theoretical guidelines, featuring low permittivity, low aspect ratios, and evenly distributed fields across their volume or surface. Conversely, dielectric resonator antennas exhibit poor bandwidth performance relative to size due to the use of high-permittivity materials. Additionally, the underwhelming performance of fractal and metamaterial

doi:10.6342/NTU202501094

designs supports the principle that antenna fields should uniformly fill the smallest enclosing sphere. These designs often involve highly resonant structures that concentrate fields in specific regions, thereby underutilizing the available volume.

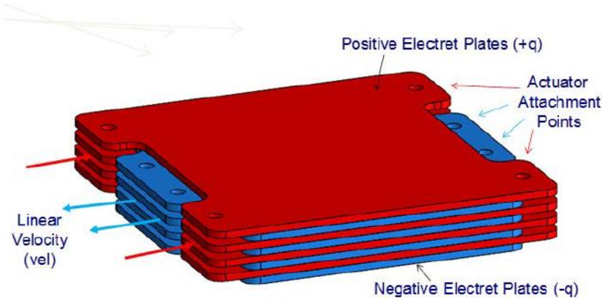

Fig. 1.11. Example of linear mechtenna. Reproduced from [13].

1.4 Mechanical Antennas

Bandwidth-efficiency product improvement has been a central topic of ESAs. The relevant discussion continues after the work of [11]. In [11], some of the emerging types of antennas, such as magnetic antennas, are capable of boosting bandwidth-efficiency products for ESAs. In this section, I will introduce the recently introduced new type of antenna, mechanical antennas or mechtenna.

Mechanical antennas, often referred to as "mechtennas," are a class of antennas that generate electromagnetic radiation through mechanical motion [13]. This concept, introduced by Bickford et al. in 2019, encompasses three primary types: linear mechtennas, rotational mechtennas, and body mode mechtennas. A linear mechtenna operates by moving spatial charges in a straight-line motion, whereas a rotational mechtenna functions as its circularly driven counterpart. The body mode mechtenna, on the other hand, utilizes asymmetric molecular motion to create dipole moment sources.

Several techniques enable the mechanical excitation of electromagnetic sources with minimal damping loss. These include ball bearings, gas bearings, magnetic and electromagnetic suspension, high-Q resonators, and flux-pinned superconductors [13]. The excitation mechanism can be integrated with a range of radiating structures.

A practical example of a linear mechtenna is depicted in Fig. 1.11. In this design, charge is confined within layers of interleaved electret material, which moves in a coordinated linear fashion to establish an electric dipole. While a fixed asymmetric charge distribution in a material generates only an electrostatic field, the dynamic motion of this structure results in charge acceleration, producing electromagnetic radiation. Since electric current is defined as the movement of charge over time (measured in coulombs per second), the relative motion of a dielectric material can induce both linear and loop currents [13]. The resulting net electric dipole moment, M_e, can be mathematically expressed as follows:

$$M_e = I_e x_e = Q_{tot} v_e = \sigma_v V_e v_e \tag{1.17}$$

, where I_e is generated current, x_e is the dielectric slab length, Q_{tot} is the total charge and v_e is linear velocity of actuating dielectric slab.

As for rotational mechtennas, the schematic representation is shown in Fig. 1.12. The rotating electric dipole can be seen as the composition of two orthogonal Hertzian dipoles that are 90° out-of-phase with one another. The electric dipole moment can be

doi:10.6342/NTU202501094

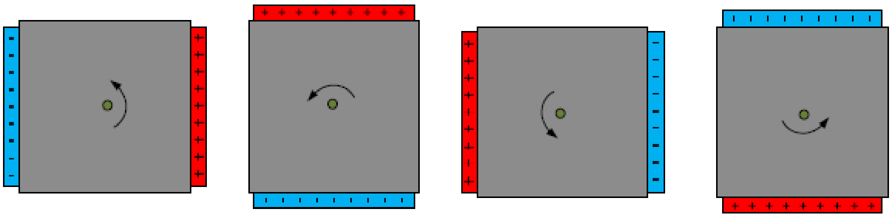

Fig. 1.12. Example of rotational mechtenna. Reproduced from [13].

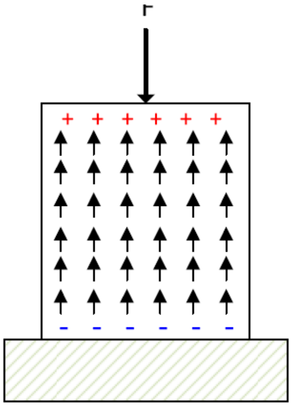

Fig. 1.13. Example of body mode mechtenna. Reproduced from [13].

defined similarly as:

$$M_e = -q_e \pi f d \tag{1.18}$$

, where d is the diameter of the cuboid, f is the circular motion frequency and q_e is polarized charges. The third kind of mechtenna is the body mode antenna. The schematic representation is shown in Fig. 1.13. For example, piezoelectric materials can be excited by applying forces onto the structure. If the structure deforms, the effective current can be generated. The effective electric dipole moment can be defined as:

$$M_e = d_x E_x \varepsilon_{max} V_{bm} 2\pi f \tag{1.19}$$

, where d_x is the piezoelectric charge constant, E_x is the modulus, ε_{max} is the maximum strain, V_{bm} is the total piezoelectric material volume and f is the excitation frequency. These electric dipole moments can be inserted into Hertzian dipole field equation. The corresponding radiation efficiency can then be evaluated and compared, as

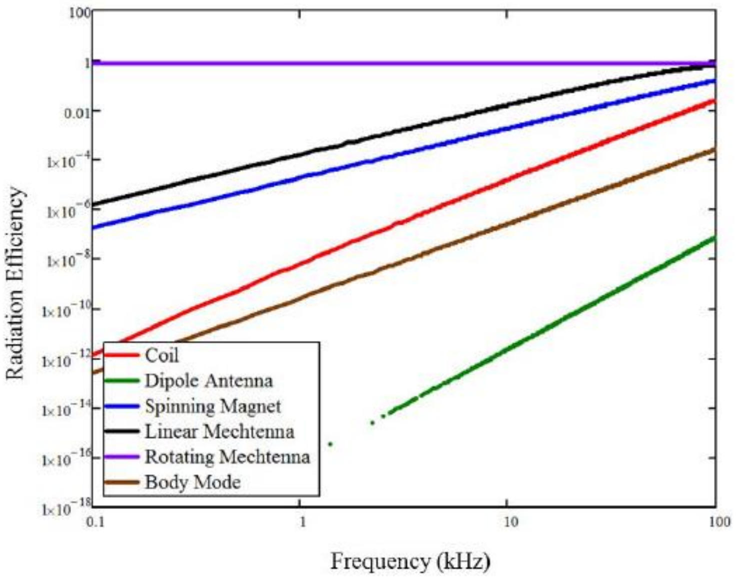

Fig. 1.14. Compasiron of mechtenna performances. Reproduced from [13].

shown in Fig. 1.14. For low frequency applications, the rotating mechtenna possesses best performance. However, this design will still be ultimately limited by mechanical driving speed. For mechanical excitation method, only mechanical resonators can work in such a high frequency range, which refers to body mode antenna. The magnetic material responses for GHz frequency are also more complicated than kHz range. Hence, more complicated modelling for the dipole moment should be considered when the GHz mechtenna application is needed.

The body mode antenna or the bulk acoustic wave (BAW)-mediated antenna is first theoretically proposed by Yao in 2015 [14]. Antenna is constructed with three layers: a bottom piezoelectric layer, a middle magnetostrictive layer, and a top dielectric layer, which acts as an acoustic buffer. When a voltage is applied to the bottom piezoelectric layer via the two electrodes shown in Fig. 1.15, periodic vertical deformations are generated. At the resonance frequency, these deformations result in BAW resonance, creating dynamic strain that extends across all three layers [15].

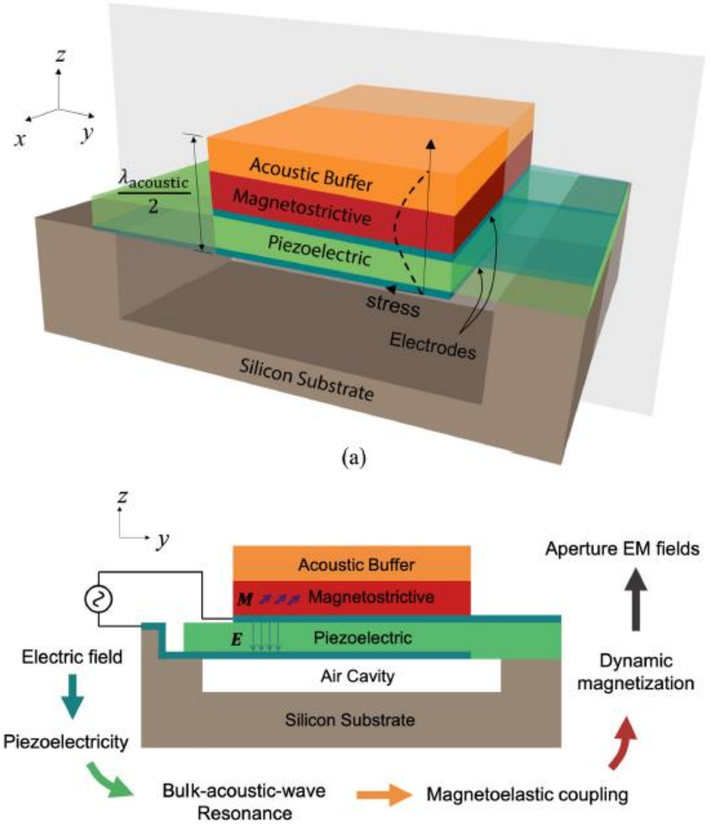

(a)

(b)

Fig. 1.15. Basic operating concept of multiferroic antenna. (a) Schematic structure and (b) mechanisms of dynamic magnetic flux generation. Reproduced from [15].

The varying mechanical strain within the central magnetostrictive layer alters the magnetization (M), causing it to oscillate. This oscillation generates a time-varying magnetic field within the layer, which in turn radiates an electromagnetic (EM) wave into free space. The strong magnetoelectric interaction between the magnetostrictive and piezoelectric layers significantly surpasses the coupling seen in single-phase multiferroic materials [15].

This antenna concept draws inspiration from the film bulk acoustic resonator

doi:10.6342/NTU202501094

(FBAR), a structure where a single suspended piezoelectric layer is placed between two metallic electrodes. Like bulk acoustic wave (BAW) antennas, FBARs operate based on BAW resonance, which is excited by an external voltage. The demonstrated high performance of FBARs suggests that BAW antennas can also achieve high-Q resonance, provided that the acoustic properties of the top two layers are carefully optimized to match those of the underlying piezoelectric layer.

Strain-mediated antennas, including BAW antennas, offer several key advantages over conventional current-driven antennas. First, they eliminate Ohmic losses from current conduction, leading to higher radiation efficiency. Second, since the radiation source relies on strain-induced in-plane magnetic flux rather than electric current, these antennas avoid platform effects—unlike traditional antennas, where conductive surfaces cause signal cancellation, the presence of a conducting platform actually enhances radiation in strain-mediated designs. Lastly, these antennas can be engineered with minimal or no conductive components above the ground plane, reducing their visibility and improving resistance to interference [14].

1.5 Dissertation Outline

This dissertation explores the design, development, and performance of multiferroic antennas. The experimental results presented in this work are among the few existing experimental verifications in the world, and they represent entirely new findings that differ significantly from existing theoretical predictions and understanding. According to previous theory, the magnetoelastic effect is considered the principal source of radiation in multiferroic antennas. However, prior experimental studies have largely overlooked this assumption and have not rigorously examined its validity. Most comparisons have been limited to multiferroic antennas and purely piezoelectric materials, without isolating the role of the magnetoelastic effect. In contrast, our experimental investigations reveal a novel phenomenon: even in the absence of a magnetoelastic effect, devices can still exhibit radiation characteristics. Furthermore, these radiation behaviors vary significantly across different frequencies, and in certain cases, even the absorption of radiated energy is observed. These findings deviate markedly from both theoretical expectations and prior experimental results. Consequently, the key contribution of this work lies in presenting a new experimental perspective that challenges prevailing assumptions and established conclusions, thereby paving the way for deeper inquiry into the underlying mechanisms of radiation in such systems.

Chapter 2 Theoretical Framework of Multiferroic Antennas

Chapter 1 introduced the fundamentals of electrically small antennas and the basic principles of multiferroic antenna operation. In this chapter, we delve further into the material science behind piezoelectric and magnetoelastic materials. When these two materials are combined, they can demonstrate an enhanced two-phase magnetoelectric effect. By exploring both ferromagnetic and bulk acoustic resonances, we can establish performance benchmarks for multiferroic antennas, providing a foundation for the experimental designs discussed in the following chapters.

2.1 Basic Properties of Piezoelectric Materials

In this chapter, the basic theory regarding piezoelectric materials is mainly based on [16]. Piezoelectricity, a well-established and extensively applied physical phenomenon, derives its name from the Greek word "to press." Certain crystals exhibit piezoelectric properties, generating charges when subjected to compression, twisting, or other distortions, a characteristic unique to crystals lacking a center of symmetry. This chapter begins with the basic principles of piezoelectricity, introducing the core equations governing piezoelectric transduction. The second half provides a comparative analysis of frequently used piezoelectric materials in electro-acoustic devices.

Piezoelectricity refers to the generation of electric polarization or charge in a material when mechanical stress is applied. Conversely, applying an electric field to a piezoelectric material induces mechanical deformation, as illustrated in Fig. 2.1 [16]. This

doi:10.6342/NTU202501094

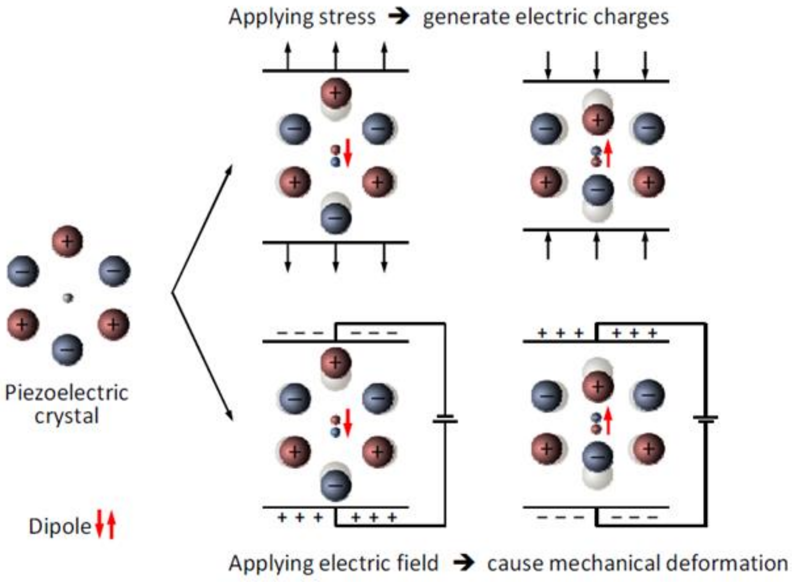

Fig. 2.1. Schematic diagram illustrating the piezoelectric effect. This behavior is a fundamental property of materials that lack a central symmetry in their structure. Reproduced from [16].

phenomenon is inherent to materials with a crystallographic structure that lacks a center of symmetry, enabling efficient conversion between electrical and mechanical oscillations. In contrast, crystals with symmetrical structures, like cubic crystals, do not exhibit piezoelectricity, as the net electric dipole in each unit cell remains zero regardless of deformation. A typical experimental setup is depicted in Fig. 2.2, where voltage is applied along one of the principal axes. The piezoelectric coefficient e_{ii} describes the relationship between the applied electric field and the resulting stress in the same direction, while e_{ij} represents the coupling between the electric field and stress induced along perpendicular axes.

When an alternating electric field is acting on a piezoelectric substrate, it triggers mechanical vibrations, producing mechanical waves within the material. The deformation of the crystal lattice is met with internal elastic restoring forces that work to return the system to its original state. The combination of stored potential energy from these

doi:10.6342/NTU202501094

distortions and the inertia of the particles results in oscillatory motion [16].

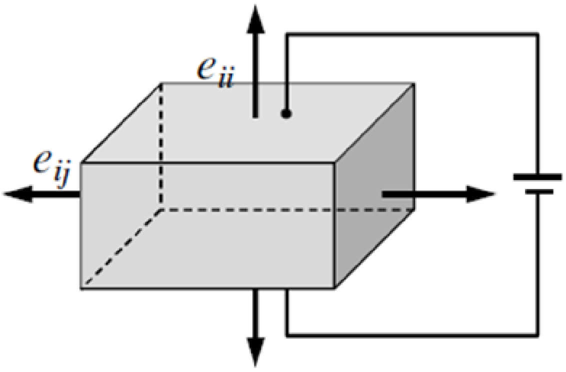

Fig. 2.2. Assessment of piezoelectric constants: e_{ii} associates the electric field with stress in the same direction, while e_{ij} links the electric field to stress in perpendicular directions. Reproduced from [16].

In a linearly elastic material, the relationship between stress T and strain S is described by the well-known Hooke's Law, expressed as:

$$T = cS \text{ or } S = sT \tag{2.1}$$

In this context, c refers to the elastic stiffness coefficient, while s corresponds to the elastic compliance coefficient. Both strain (S) and stress (T) are second-order tensors, yet they each possess only six independent components. To simplify their representation, they are often expressed as 6×1 column vectors using a condensed index notation.:

$$S = \begin{bmatrix} S_{11} & S_{12} & S_{13} \\ S_{21} & S_{22} & S_{23} \\ S_{31} & S_{32} & S_{33} \end{bmatrix} = \begin{bmatrix} S_1 \\ S_2 \\ S_3 \\ S_4 \\ S_5 \\ S_6 \end{bmatrix}, \text{ where } \begin{matrix} S_1 = S_{11} \\ S_2 = S_{22} \\ S_3 = S_{33} \\ S_4 = 2S_{23} = 2S_{32} \\ S_5 = 2S_{13} = 2S_{31} \\ S_6 = 2S_{12} = 2S_{21} \end{matrix} \tag{2.2}$$

doi:10.6342/NTU202501094

$$T = \begin{bmatrix} T_{11} & T_{12} & T_{13} \\ T_{21} & T_{22} & T_{23} \\ T_{31} & T_{32} & T_{33} \end{bmatrix} = \begin{bmatrix} T_1 \\ T_2 \\ T_3 \\ T_4 \\ T_5 \\ T_6 \end{bmatrix}, \text{ where } \begin{matrix} T_1 = T_{11} \\ T_2 = T_{22} \\ T_3 = T_{33} \\ T_4 = 2T_{23} = 2T_{32} \\ T_5 = 2T_{13} = 2T_{31} \\ T_6 = 2T_{12} = 2T_{21} \end{matrix} \tag{2.3}$$

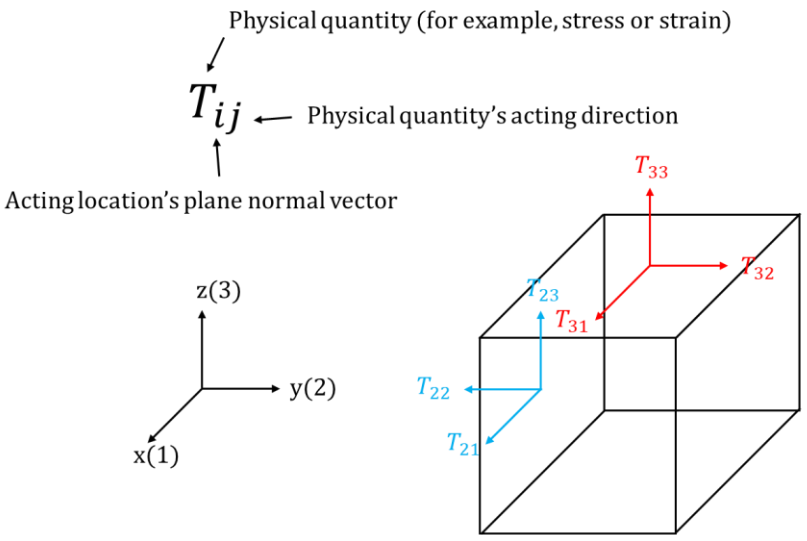

Fig. 2.3. Schematic diagram illustrating the sign convention of the stress tensor [17].

The sign convention of strain S_{ij} or stress T_{ij} can be illustrated as Fig. 2.3. The first index i refers to the vector normal of the plane location of acting stress, while the second index j refers to the direction of acting stress. For example, T_{31} refers to the acting stress to the direction $x(1)$ on the $z(3)$ plane. As a result, T_{31} will be the shear stress; T_{33} refers to the acting stress to the direction $z(3)$ on the $z(3)$ plane. As a result, T_{33} will be the longitudinal normal stress.

Equation (2.4) similarly describes the relationship between electric displacement D and electric field E:

$$D = \varepsilon E \tag{2.4}$$

Here, where ε represents the permittivity. The electric field and dielectric displacement are defined as vectors.

Piezoelectricity results from the combined effects of Hooke's Law and the material's electrical properties. Depending on the selected variables—mechanical stress T, mechanical strain S, electric field E, and electric displacement D—Equation (2.5) expresses the constitutive relations for piezoelectricity. The superscript of the constants means that they're measured under fixed variables. For example, s^E means that elastic compliance constant s is measured under the constant electric field.

$$\begin{cases} T = c^D S - hD \\ E = \beta^S D - hS \end{cases} \quad \text{h-form}$$

$$\begin{cases} S = s^E T + dE \\ D = \varepsilon^T E + dT \end{cases} \quad \text{d-form}$$

$$\begin{cases} S = s^D T + gD \\ E = \beta^T D - gT \end{cases} \quad \text{g-form} \qquad (2.5)$$

$$\begin{cases} T = c^E S - eE \\ D = \varepsilon^S E + eS \end{cases} \quad \text{e-form}$$

These equations represent the same underlying phenomenon but are expressed in different forms, each associated with a specific type of piezoelectric coefficient. The coefficients h, d, g, and e are interrelated and can be converted between different formulations [18]. Equation (2.6) establishes these four piezoelectric coefficients in terms of stress (T), strain (S), electric displacement (D), and electric field (E) as follows:

doi:10.6342/NTU202501094

$$h_{ij} = -(\frac{\partial E_i}{\partial S_j})^D = -(\frac{\partial T_j}{\partial D_i})^D$$

$$d_{ij} = -(\frac{\partial D_i}{\partial T_j})^E = -(\frac{\partial S_i}{\partial E_j})^T$$

$$g_{ij} = -(\frac{\partial E_i}{\partial T_j})^D = -(\frac{\partial S_j}{\partial D_i})^T \tag{2.6}$$

$$e_{ij} = -(\frac{\partial D_i}{\partial S_j})^E = -(\frac{\partial T_j}{\partial E_i})^S$$

The so-called e-form and d-form constitutive equations are the most widely used, the e-form can be used when stress is mainly analyzed, which is called stress-charge form; while d-form can be used for strain, which is called strain-charge form. The e-form can be expressed in tensor index notation in (2.7).

$$\begin{cases} T_{ij} = c_{ijkl}^{E} S_{kl} - e_{kij}^{T} E_k \\ D_i = \varepsilon_{ik}^{S} E_k - e_{ikl} S_{kl} \end{cases} \tag{2.7}$$

The full expression of (2.7) can be shown below

$$\begin{bmatrix} T_1 \\ T_2 \\ T_3 \\ T_4 \\ T_5 \\ T_6 \end{bmatrix} = \begin{bmatrix} c_{11} & c_{12} & c_{13} & c_{14} & c_{15} & c_{16} \\ & c_{22} & c_{23} & c_{24} & c_{25} & c_{26} \\ & & c_{33} & c_{34} & c_{35} & c_{36} \\ & & & c_{44} & c_{45} & c_{46} \\ & & & & c_{55} & c_{56} \\ & & & & & c_{66} \end{bmatrix} \begin{bmatrix} S_1 \\ S_2 \\ S_3 \\ S_4 \\ S_5 \\ S_6 \end{bmatrix} - \begin{bmatrix} e_{11} & e_{21} & e_{31} \\ e_{12} & e_{22} & e_{32} \\ e_{13} & e_{23} & e_{33} \\ e_{14} & e_{24} & e_{34} \\ e_{15} & e_{25} & e_{35} \\ e_{16} & e_{26} & e_{36} \end{bmatrix} \begin{bmatrix} E_1 \\ E_2 \\ E_3 \end{bmatrix}$$

$$\begin{bmatrix} D_1 \\ D_2 \\ D_3 \end{bmatrix} = \begin{bmatrix} \varepsilon_1 & \varepsilon_6 & \varepsilon_5 \\ & \varepsilon_2 & \varepsilon_4 \\ & & \varepsilon_3 \end{bmatrix} \begin{bmatrix} E_1 \\ E_2 \\ E_3 \end{bmatrix} - \begin{bmatrix} e_{11} & e_{12} & e_{13} & e_{14} & e_{15} & e_{16} \\ e_{21} & e_{22} & e_{23} & e_{24} & e_{25} & e_{26} \\ e_{31} & e_{32} & e_{33} & e_{34} & e_{35} & e_{36} \end{bmatrix} \begin{bmatrix} S_1 \\ S_2 \\ S_3 \\ S_4 \\ S_5 \\ S_6 \end{bmatrix} \tag{2.8}$$

In the case of a piezoelectric material with hexagonal structure, such as AlN or ZnO with c-axis-oriented columnar growth, the constitutive relation can be simplified as:

$$\begin{bmatrix} T_1 \\ T_2 \\ T_3 \\ T_4 \\ T_5 \\ T_6 \end{bmatrix} = \begin{bmatrix} c_{11} & c_{12} & c_{13} & 0 & 0 & 0 \\ & c_{11} & c_{23} & 0 & 0 & 0 \\ & & c_{33} & 0 & 0 & 0 \\ & & & c_{44} & 0 & 0 \\ & & & & c_{55} & 0 \\ & & & & & c_{66} \end{bmatrix} \begin{bmatrix} S_1 \\ S_2 \\ S_3 \\ S_4 \\ S_5 \\ S_6 \end{bmatrix} - \begin{bmatrix} 0 & 0 & e_{31} \\ 0 & 0 & e_{32} \\ 0 & 0 & e_{33} \\ 0 & e_{15} & 0 \\ e_{15} & 0 & 0 \\ 0 & 0 & 0 \end{bmatrix} \begin{bmatrix} E_1 \\ E_2 \\ E_3 \end{bmatrix} \tag{2.9}$$

$$, c_{66} = \frac{c_{11} - c_{12}}{2}$$

$$\begin{bmatrix} D_1 \\ D_2 \\ D_3 \end{bmatrix} = \begin{bmatrix} \varepsilon_1 & 0 & 0 \\ & \varepsilon_1 & 0 \\ & & \varepsilon_3 \end{bmatrix} \begin{bmatrix} E_1 \\ E_2 \\ E_3 \end{bmatrix} - \begin{bmatrix} 0 & 0 & 0 & 0 & e_{15} & 0 \\ 0 & 0 & 0 & e_{15} & 0 & 0 \\ e_{31} & e_{31} & e_{33} & 0 & 0 & 0 \end{bmatrix} \begin{bmatrix} S_1 \\ S_2 \\ S_3 \\ S_4 \\ S_5 \\ S_6 \end{bmatrix}$$

There are 10 independent non-zero coefficients: $c11$, $c12$, $c13$, $c33$, $c44$, $e15$, $e31$, $e33$, $\varepsilon 1(\varepsilon 11)$, and $\varepsilon 3(\varepsilon 33)$. For instance, the piezoelectric coefficient $e31$ connects the thickness electric field to the lateral stress field. This corresponds to the shear excitation, while $e33$ represents the longitudinal excitation. The displacement vector can be related to the strain tensor through (2.10) [19].

$$S = \begin{bmatrix} S_1 \\ S_2 \\ S_3 \\ S_4 \\ S_5 \\ S_6 \end{bmatrix} = \begin{bmatrix} \frac{\partial}{\partial x} & 0 & 0 \\ 0 & \frac{\partial}{\partial y} & 0 \\ 0 & 0 & \frac{\partial}{\partial z} \\ 0 & \frac{\partial}{\partial z} & \frac{\partial}{\partial y} \\ \frac{\partial}{\partial z} & 0 & \frac{\partial}{\partial x} \\ \frac{\partial}{\partial y} & \frac{\partial}{\partial x} & 0 \end{bmatrix} \begin{bmatrix} u_x \\ u_y \\ u_z \end{bmatrix} \tag{2.10}$$

As for material for PZT-5H, they can be written as:

doi:10.6342/NTU202501094

$$\begin{bmatrix} T_1 \\ T_2 \\ T_3 \\ T_4 \\ T_5 \\ T_6 \end{bmatrix} = \begin{bmatrix} c_{11} & c_{12} & c_{13} & 0 & 0 & 0 \\ c_{12} & c_{11} & c_{13} & 0 & 0 & 0 \\ c_{13} & c_{13} & c_{33} & 0 & 0 & 0 \\ & & & c_{44} & 0 & 0 \\ & & & & c_{44} & 0 \\ & & & & & c_{66} \end{bmatrix} \begin{bmatrix} S_1 \\ S_2 \\ S_3 \\ S_4 \\ S_5 \\ S_6 \end{bmatrix} - \begin{bmatrix} 0 & 0 & e_{31} \\ 0 & 0 & e_{31} \\ 0 & 0 & e_{33} \\ 0 & e_{15} & 0 \\ e_{15} & 0 & 0 \\ 0 & 0 & 0 \end{bmatrix} \begin{bmatrix} E_1 \\ E_2 \\ E_3 \end{bmatrix}$$

(2.11)

$$\begin{bmatrix} D_1 \\ D_2 \\ D_3 \end{bmatrix} = \begin{bmatrix} \varepsilon_1 & 0 & 0 \\ & \varepsilon_2 & 0 \\ & & \varepsilon_3 \end{bmatrix} \begin{bmatrix} E_1 \\ E_2 \\ E_3 \end{bmatrix} - \begin{bmatrix} 0 & 0 & 0 & 0 & e_{15} & 0 \\ 0 & 0 & 0 & e_{15} & 0 & 0 \\ e_{31} & e_{31} & e_{33} & e_{34} & 0 & 0 \end{bmatrix} \begin{bmatrix} S_1 \\ S_2 \\ S_3 \\ S_4 \\ S_5 \\ S_6 \end{bmatrix}$$

The numerical values for AlN and PZT-5H are given in (2.12) and (2.13) respectively [22].

$$[c] = \begin{bmatrix} 4.1 & 1.49 & 0.99 & 0 & 0 & 0 \\ 1.49 & 4.1 & 0.99 & 0 & 0 & 0 \\ 0.99 & 0.99 & 3.89 & 0 & 0 & 0 \\ & & & 1.25 & 0 & 0 \\ & & & & 1.25 & 0 \\ & & & & & 1.305 \end{bmatrix} (10^{11}\frac{N}{m^2})$$

$$[e] = \begin{bmatrix} 0 & 0 & 0 & 0 & -0.48 & 0 \\ 0 & 0 & 0 & -0.48 & 0 & 0 \\ -0.58 & -0.58 & 1.55 & 0 & 0 & 0 \end{bmatrix} (\frac{C}{m^2})$$

(2.12)

$$[\varepsilon] = \begin{bmatrix} 9 & 0 & 0 \\ & 9 & 0 \\ & & 9 \end{bmatrix}$$

$$[c] = \begin{bmatrix} 1.27205 & 8.02122 & 8.46702 & 0 & 0 & 0 \\ 8.02122 & 1.27205 & 8.46702 & 0 & 0 & 0 \\ 8.46702 & 8.46702 & 1.17436 & 0 & 0 & 0 \\ & & & 2.29885 & 0 & 0 \\ & & & & 2.29885 & 0 \\ & & & & & 2.34742 \end{bmatrix} (10^{11}\frac{N}{m^2})$$

$$[e] = \begin{bmatrix} 0 & 0 & 0 & 0 & 17.0345 & 0 \\ 0 & 0 & 0 & 17.0345 & 0 & 0 \\ -6.62281 & -6.62281 & 23.2403 & 0 & 0 & 0 \end{bmatrix} (\frac{C}{m^2})$$

(2.13)

$$[\varepsilon] = \begin{bmatrix} 1704.4 & 0 & 0 \\ & 1704.4 & 0 \\ & & 1433.6 \end{bmatrix}$$

After reviewing some of the basic theory of Piezoelectric materials, I will then introduce some of the basic properties of piezoelectric materials. Since the discovery of the piezoelectric effect in quartz crystals, numerous materials exhibiting piezoelectric properties have been identified and extensively studied. Key considerations in developing new piezoelectric materials include high electromechanical coupling coefficients, low electromechanical losses and integratable with CMOS processes. Two of the most used piezoelectric materials in electro-acoustic applications will be introduced and used in this dissertation: lead zirconium titanate and aluminum nitride [16].

Lead zirconate titanate ($Pb[Zr_xTi_{1-x}]O_3$, $0 \leq x \leq 1$), commonly referred to as PZT, is a ferroelectric ceramic known for its exceptional piezoelectric and pyroelectric properties. Thick PZT films can be fabricated using two primary methods: by pressing and sintering powders at 1,350°C or through the sol-gel process. Both techniques need a poling step, where a strong DC electric field is applied to the PZT substrate to induce polarization. Yet, the material may lose its piezoelectric properties (de-poling) if exposed to a strong AC field or temperatures exceeding its Curie point. Hence, it is also adjustable to the AC field.

Since the late 1950s, PZT has been extensively utilized, particularly in medical imaging technologies. Table 1 provides a comparison between PZT, ZnO, and AlN, highlighting PZT's notably high dielectric constant. One of its key advantages is its superior piezoelectric coupling coefficient, which plays a crucial role in affecting energy transfer efficiency. This property makes PZT especially suitable for applications requiring significant displacements, such as ultrasound transducers and actuators. Additionally, its voltage-dependent coupling coefficient enhances its potential for use in tunable intermediate frequency (IF) resonators and filters. However, PZT experiences significant losses at high frequencies, limiting its application to low-frequency systems where maintaining a high Q is less critical. Despite these challenges, advancements in fabrication techniques, such as the sol-gel process, have facilitated its integration into

MEMS devices [21]-[23].

Table 1. Comparison of piezoelectric materials [24]-[26]. Reproduced from [16].

Property	PZT	AlN	ZnO
Density (kg/m^3)	7600	3260	5670
Young's Modulus (10^{11}N/m^2)	0.49	3.94	2.11
Thermal Conductivity (W/m·K)	1.8	200-320	60
Thermal Expansion (10^{-6}/K)	-	4.15	2.92
Dielectric Constant (F/m)	80-400	8.2-8.9	9.2
Longitudinal Acoustic Velocity (m/s)	~5000	~11000	~6350
Temperature Coefficient of Frequency or TCF(ppm/°C)	-	-25	-60
d_{33} piezoelectric Coefficient (10^{-12}C/N)	200	5.6	12.4
d_{33} piezoelectric Coupling Coefficient k_t^2(%)	~15-35	2.6	5
d_{31} piezoelectric Coefficient (10^{-12}C/N)	120	2.6	5
d_{31} piezoelectric Coupling Coefficient k_t^2(%)	~10	~2.5	~2.5
Intrinsic Loss	High	Very low	Low
CMOS Compatibility	No	Yes	Okay

Aluminum nitride (AlN) is a non-ferroelectric material that lacks a Curie point. Its distinct structural characteristics enable its use across diverse applications. One of its notable properties is exceptional thermal stability in inert environments. When exposed to air, AlN starts to oxidize at approximately 700°C, forming a protective aluminum oxide layer that helps preserve the material's integrity up to temperatures as high as 1,370°C [27], [28].

In recent years, hexagonal polycrystalline AlN thin films have gained attention for their high-quality piezoelectric properties, particularly for acoustic wave transduction in RF applications. AlN provides a unique combination of high acoustic phase velocity, low

doi:10.6342/NTU202501094

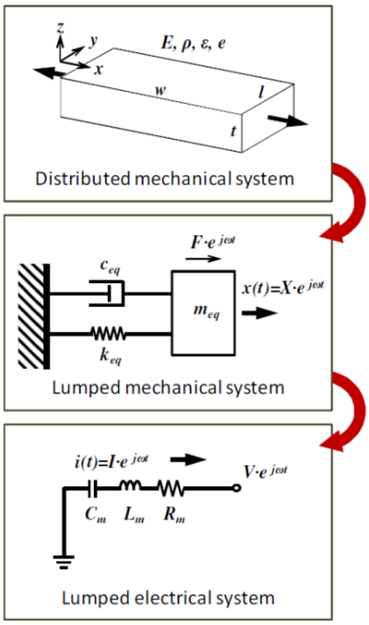

Fig. 2.4. Schematic diagram illustrating the relation between mechanical system and electrical system. Reproduced from [16].

motional resistance, and CMOS compatibility. AlN offers nearly twice the acoustic wave velocity compared to other materials, making it superior for high-frequency applications. Additionally, AlN's lower temperature coefficient of the piezoelectric layer, compared to ZnO, minimizes thermal drift in resonators. However, AlN exhibits slightly lower piezoelectric coupling than ZnO or $LiNbO_3$, limiting its use in synthesizing bandpass filters for modern mobile communication systems that typically require 2–5% fractional bandwidths. Nevertheless, AlN excels in narrowband filter applications for channel-select architectures. Its excellent properties make AlN a key material for CMOS-compatible RF resonator and filter technologies [30],[31].

2.2 Equivalent Circuits and Design Principles of Piezoelectric Resonators

A resonator can be described using a distributed mechanical system, which can be further simplified into a lumped mechanical model consisting of mass, a spring, and a damper. This mechanical representation has an electrical counterpart, where the behavior of the system can be modeled using resistors, inductors, and capacitors, as illustrated in Fig. 2.4. By analyzing measurement data, material properties can be extracted through lumped parameter modeling. Two widely used equivalent models for this purpose are the Mason model and the Butterworth Van Dyke (BVD) model.

The Mason model conceptualizes a piezoelectric material as having two acoustic ports and one electrical port, with energy transfer occurring through an ideal electromechanical transformer characterized by a turn ratio, Γ. Fig. 2.5 presents the Mason model for a piezoelectric layer [32]. A further reduction of the Mason model is shown in Fig. 2.6, where impedance elements are substituted with R-L-C components. When an AC signal is applied, the resulting electric field generates mechanical strain. If the frequency of the applied signal coincides with the resonator's natural frequency, the system enters resonance, causing a distinct vibrational mode. Additionally, the structure exhibits a static capacitance ($C0$) due to the dielectric properties between electrodes, which exists in parallel with the electromechanical resonator.

The equivalent circuit in Fig. 2.6 can be further simplified into the BVD model, illustrated in Fig. 2.7. In this representation, the resonator is characterized by a motional

doi:10.6342/NTU202501094

branch consisting of a motional resistor (Rm), a motional inductor (Lm), and a motional capacitor (Cm). These elements are placed in parallel with the geometric capacitance ($C0$), which is independent of vibrational behavior. The motional branch components—Rm, Lm, and Cm—are derived from the resonator's acoustic properties. Under ideal conditions where resistive losses are negligible (Rm=0), the system reaches infinite admittance at the series resonance frequency (fs), commonly known as the "resonance frequency." This frequency is governed by the motional inductance (Lm) and motional capacitance (Cm),

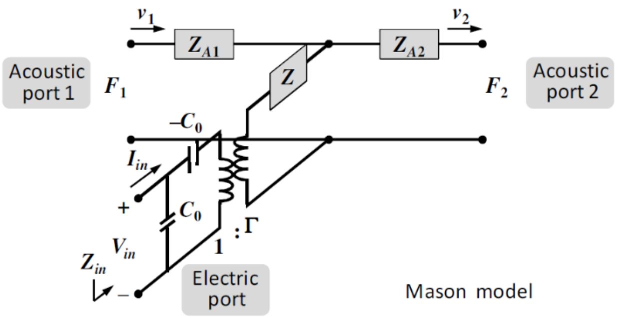

Fig. 2.5. Schematic diagram of Mason model. Reproduced from [16].

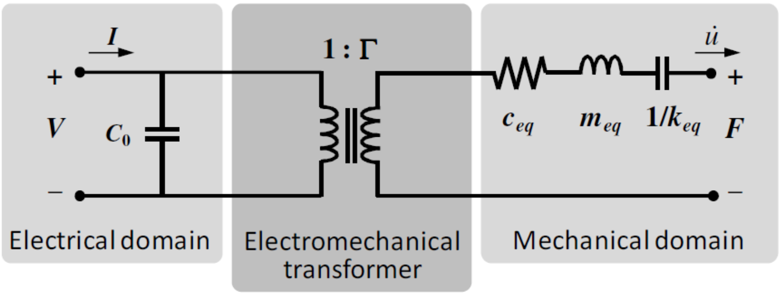

Fig. 2.6. Schematic diagram of simplified Mason model. Reproduced from [16].

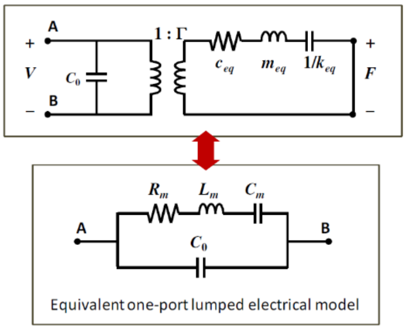

Fig. 2.7. Schematic diagram of 1-port BVD model. Reproduced from [16].

as defined in Equation (2.14).

$$f_s = \frac{\omega_s}{2\pi} = \frac{1}{2\pi}\frac{1}{\sqrt{L_m C_m}} \tag{2.14}$$

The parallel resonance frequency (fp), often referred to as the "anti-resonance frequency," is the point where the admittance reaches zero. This frequency is influenced by the motional inductance (Lm), motional capacitance (Cm), and static capacitance $(C0)$, as described in Equation (2.15).

$$f_p = \frac{\omega_p}{2\pi} = \frac{1}{2\pi}\sqrt{\frac{C_m + C_0}{L_m C_m C_0}} = f_s \cdot \sqrt{1 + \frac{C_0}{C_m}} \approx f_s \cdot \left(1 + \frac{C_m}{2C_0}\right) \tag{2.15}$$

The approximation holds true when $Cm \ll C0$, a condition that is typically satisfied for micromechanical resonators at most relevant frequencies.

Another important parameter is acoustic phase velocity. They can be derived from the Christoffel matrix [16]. In the piezoelectric materials, the effective stiffness matrix will be rewritten as:

$$c_{eff}^{E} = c^{E} + \frac{e^2}{\varepsilon^S} \tag{2.16}$$

The original phase velocity of a propagating wave is:

$$v_a = \frac{\omega}{k} = \sqrt{\frac{c^E}{\rho}} \tag{2.17}$$

The stiffened phase velocity of a propagating wave is:

$$v_o = \sqrt{\frac{c_{eff}^{E}}{\rho}} = \sqrt{\frac{c^E + \frac{e^2}{\varepsilon^S}}{\rho}} \tag{2.18}$$

The difference in phase velocity depends on the strength of the piezoelectric coupling and the direction of propagation. The relation can be formulated as:

$$v_o = v_a\sqrt{1 + \frac{e^2}{c^E \varepsilon^S}} = v_a\sqrt{1 + K^2} \tag{2.19}$$

$$K^2 = \frac{e^2}{c^E \varepsilon^S} \tag{2.20}$$

(2.20) is the *piezoelectric coupling constant*. It represents the enhancement of stiffness constant for a specific propagation direction. Another term named *electromechanical coupling coefficient* k_t^2 can be defined as:

$$k_t^2 = \frac{K^2}{1+K^2} = \frac{v_o^2 - v_a^2}{v_o^2} \tag{2.21}$$

$$k_t^2 = \frac{e^2}{c^D \varepsilon^S} \tag{2.22}$$

It represents the conversion between mechanical and electrical energy. For most of the case with moderate and low K^2, the K^2 and k_t^2 are very close [19].

Once knowing the phase velocity, the relation between fundamental mode frequency and corresponding dimensions can be written as:

$$f_s = \frac{v_0}{\left(\frac{n+1}{2}\right) \times (2d)}, n = 1,2 \ldots etc \tag{2.23}$$

, where d is the thickness or corresponding resonance dimensions and n the mode number. Another important benchmark for resonator design is the mechanical quality factor (Q). There has been a lot of discussion about detailed calculations for different Q. The most common one is the 3dB bandwidth:

$$Q = \frac{f_0}{BW_{3dB}} \tag{2.24}$$

For more recent and comprehensive discussion on accurate Q extraction, [33] compares

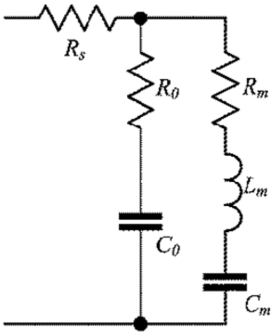

Fig. 2.8. mBVD model. Reproduced from [34].

and improves the relative formulas. The Time-Averaged Stored Energy (TASE) in bulk acoustic wave (BAW) resonators is critical for calculating the Quality Factor (Q), a key performance metric for resonators. Earlier formulations for estimating TASE based on S_{11} parameters often failed in regions where spurious modes were present, leading to inaccurate or even negative Q values. [33] addresses these limitations by proposing an improved TASE formula derived from an extended Butterworth-Van Dyke (eBVD) model. [34] builds on previous research, including methods by Larson, Lakin, and Feld, which use various approaches like modified Butterworth-Van Dyke (mBVD) models and Z-parameter analysis to estimate Q. mBVD model is the one improved from Fig. 2.7, as shown in Fig. 2.8. It can be divided into two arms: motional branch and static branch. The motional branch includes R_m, L_m and C_m, which corresponds to motional resistance, inductance and capacitance. They account for series resonance frequency. The static branch includes C_0, which corresponds to static capacitance from parallel plate capacitance. These terms comprise BVD model and additional term R_s and R_0 represents metal electrode and substrate losses.

In Larson's work [34], Q can be extracted from mBVD model. One can first fit S_{11} parameter into mBVD equivalent circuit model and identify the location of series and parallel resonant frequency from the measurement data. Then, the quality factor at series resonance (Q_{s0}) and at parallel resonance (Q_{p0}) can be extracted by the following formula:

$$\frac{1}{Q_{s0}} = \frac{1}{Q_s}\left(1 + \frac{R_s}{R_m}\right), \frac{1}{Q_s} = \omega_s R_m C_m \tag{2.25}$$

$$\frac{1}{Q_{p0}} = \frac{\omega_p}{\omega_s}\left(\frac{1}{Q_s} + \frac{1}{Q_e}\right), \frac{1}{Q_e} = \frac{\omega_s R_0 C_0}{r}, r = \frac{C_0}{C_m} \tag{2.26}$$

In another work by Lakin [35], Q can also be extracted from measured Z parameter phase difference:

$$Q_s = \frac{1}{2} f_s \left| \frac{d\phi}{df} \right|_{,fs} \tag{2.27}$$

$$Q_p = \frac{1}{2} f_p \left| \frac{d\phi}{df} \right|_{,fp} \tag{2.28}$$

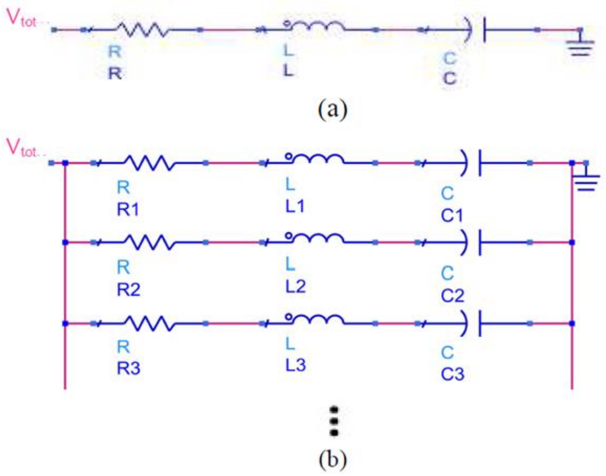

Fig. 2.9. (a) Single main resonance and (b) that including multiple spurious resonances. Reproduced from [33].

However, only quality factor at resonance and anti-resonance can be evaluated from (2.25) to (2.28). Feld proposed another general method of Q calculation in [36]. For low loss resonator, the quality factor near the resonance frequency range can be calculated from measured S_{11} parameter:

$$Q = \frac{time\ averaged\ stored\ energy\ (TASE)}{time\ averaged\ dissapated\ energy\ (TADE)} \tag{2.29}$$

$$TASE = P_{inc} \cdot |S_{11}| \cdot \frac{d\phi}{d\omega} \tag{2.30}$$

$$TADE = P_{inc} \cdot \frac{(1 - |S_{11}|^2)}{\omega} \tag{2.31}$$

While these methods provided insights into resonator behavior, they exhibited deficiencies in accurately computing TASE in spurious mode regions. The proposed method leverages the extended BVD (eBVD) model to improve on these earlier approaches. The improved TASE formula was derived by analyzing the admittance of a multibranch R-L-C circuit modeled after the eBVD structure. As shown in Fig. 2.9, the one-port resonator connected to ground can be represented by a branch of R-L-C network. The study assumes that, at any frequency, the overall admittance is dominated by a single branch. This allows for a precise computation of TASE using S11 parameter derivatives. The improved formula also accounts for the spurious-mode regions by decomposing TASE into components representing phase delay and magnitude variation with frequency. It was shown that Q is equal to:

$$Q = \frac{time\ averaged\ stored\ energy\ (TASE)}{time\ averaged\ dissapated\ energy\ (TADE)} \tag{2.32}$$

$$TASE = P_{inc} \cdot \left|\frac{dS_{11}}{d\omega}\right| = P_{inc} \cdot \sqrt{\left\{|S_{11}| \cdot \frac{d\phi}{d\omega}\right\}^2 + \left\{\frac{d|S_{11}|}{d\omega}\right\}^2} \tag{2.33}$$

$$TADE = P_{inc} \cdot \frac{(1 - |S_{11}|^2)}{\omega} \tag{2.33}$$

After obtaining Q, the figure of merit (FOM) is defined together with *effective coupling coefficient* k_{eff}^2 for the practical filter design based on resonator structure:

$$k_{eff}^2 = \frac{f_p^2 - f_s^2}{f_p^2} \tag{2.34}$$

$$FOM = \frac{k_{eff}^2 \cdot Q}{\left(1-k_{eff}^2\right)} \text{ or simply } k_{eff}^2 Q \text{ if } k_{eff}^2 \ll 1 \tag{2.35}$$

The physical meaning of FOM can be interpreted as combination of energy conversion amplification. k_{eff}^2 represents electrical and mechanical energy conversion efficiency and Q represents energy amplification factor near the resonance.

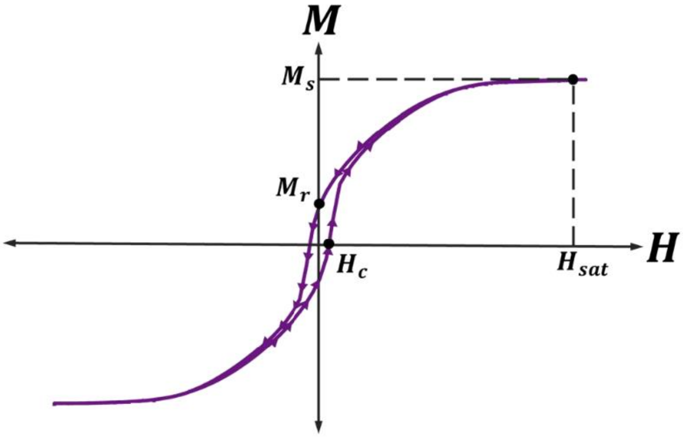

Fig. 2.10. Typical hysteresis curve. Reproduced from [37].

2.3 Basic Properties of Ferromagnetic and Magneoelastic Materials

In this section, the basic theory regarding ferromagnetic materials is reviewed based on [38]. Ferromagnetic materials exhibit a unique characteristic where their permeability follows hysteretic behavior. This means that instead of a simple, linear response, their permeability depends on the specific path taken by the applied magnetic field. Several important properties can be derived from these hysteresis curves. First, the remanent magnetization (Mr) represents the magnetization remaining when the external field is removed. Second, the coercive field (Hc) indicates the strength of the applied field needed to reduce the magnetization to zero. Third, the saturating field ($Hsat$) refers to the field strength required to align all magnetic moments within the material. However, due to thermal variations, absolute saturation is unattainable, so an approximate value is used. Lastly, the saturation magnetization (Ms) is the magnetization level the material approaches as the applied field increases indefinitely, though perfect measurement is impractical due to thermal effects. Their relation can be illustrated in Fig. 2.10 [37].

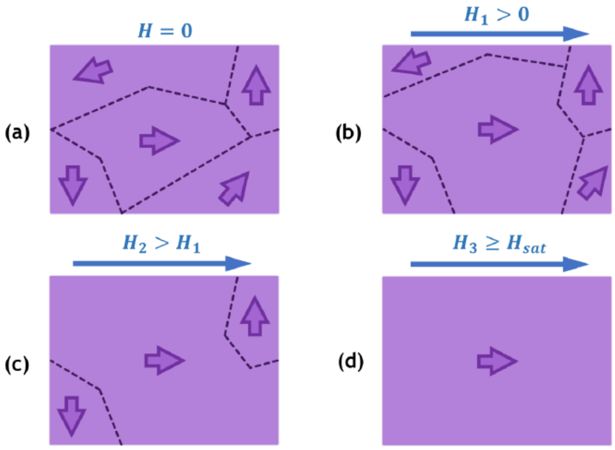

Fig. 2.11. Gradual change inside the domain structure under an applied magnetic field Reproduced from [37].

Inside a ferromagnetic material, individual magnetic dipoles are influenced by random thermal fluctuations, local interactions, and external magnetic fields [38]. These dipoles typically group together into regions called domains, as shown in Fig. 2.11. The boundary between two domains, known as a domain wall, exhibits a gradual change in magnetization as it transitions between the orientations of neighboring domains.

When an external magnetic field is applied, the material’s response depends on the field strength. At low fields, changes in net magnetization are primarily driven by the change of domain walls, as shown in Fig. 2.11(b). These walls are highly mobile, resulting

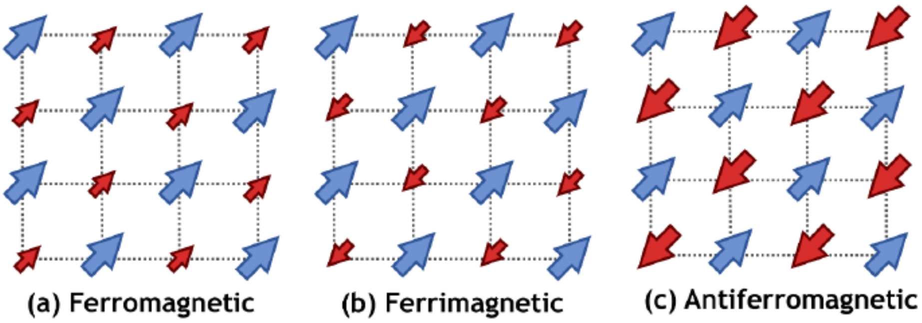

Fig. 2.12. (a) Ferromagnetic material. (b) Ferrimagnetic material. (c) Antiferromagnetic material. Reproduced from [37].

in large instantaneous susceptibility and contributing to the steep portions of the hysteresis loop. At higher fields, magnetization changes occur due to the rotation of magnetic dipoles within the remaining domains, which are often oriented perpendicular to the applied field, as shown in Fig. 2.11(c). These changes are smaller, leading to lower instantaneous susceptibility as the material nears saturation. Beyond saturation (Fig. 2.11(d)), all dipoles are fully aligned, and no further magnetization changes occur. Additionally, when the material's dimensions approach the size of individual domains, unique domain structures can form [39]-[43].

Ferrimagnetic materials are like ferromagnetic materials but consist of at least two forms of atomic-scale magnetic dipoles aligned antiparallel to each other. As shown in Fig. 2.12(b), these dipoles differ in magnitude, resulting in a net magnetization. Ferrimagnetic materials are commonly used in radio frequency applications due to their insulating nature, which eliminates eddy current losses [44]-[50]. In modeling, only net magnetization is considered, ignoring atomic-scale variations. When the opposing dipoles cancel out, yielding no net magnetization, as shown in Fig. 2.12(c), the material is classified as antiferromagnetic [47]. Antiferromagnetic materials, with their unique internal dynamics, show potential for future terahertz systems.

doi:10.6342/NTU202501094

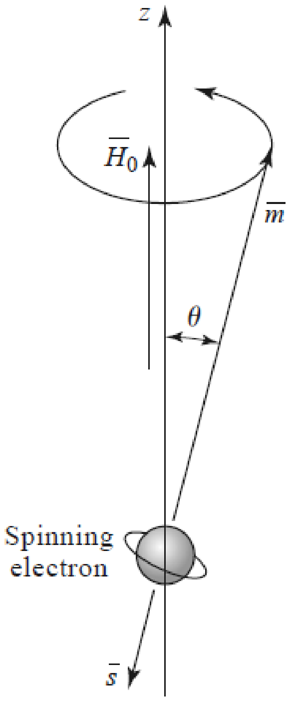

Fig. 2.13. Spinning electron with magnetic dipole moment and angular momentum. Reproduced from [51].

Different from the DC magnetic field response, the dynamic response to an oscillating AC magnetic field requires additional micromagnetic modelling based on electron spin precession [51]. To begin with general spin precession models, one should consider the magnetic dipole moment of an electron for its spin:

$$m = \frac{q\hbar}{2m_e} = 9.27 \times 10^{-24}\ (A{-}m^2) \tag{2.36}$$

In this context, $\hbar$ represents Planck's constant divided by 2π, q is the electron charge, and m_e is the electron mass. When an electron orbits around a nucleus, it contributes an additional magnetic dipole moment. However, for most microwave ferrite materials, this effect is relatively small compared to the electron spin itself [51]. In most solid materials, electron spins are paired with opposite orientations, which results in a negligible overall magnetic moment. However, in magnetic materials, a significant portion of electron spins remain unpaired, with an imbalance between left- and right-handed spins. These spins typically point in random directions, leading to a small net magnetic moment. When an external magnetic field is applied, these individual dipoles align, producing a much larger net magnetic moment. Exchange forces can then maintain the alignment of these electron spins even after the external field is removed, causing the material to remain magnetized [51].

Each electron has a spin angular momentum ($\bar{s}$), and its magnitude is related to Planck's constant. The ratio of the spin magnetic moment ($\bar{m}$) to the angular momentum is called the gyromagnetic ratio, as outlined in equations (2.36) and (2.37), and illustrated in Fig. 2.13.

$$s = \frac{\hbar}{2} \tag{2.37}$$

$$\gamma = \frac{m}{s} = \frac{q}{m_e} = 1.759 \times 10^{11}\ (C/kg) \tag{2.38}$$

$$\bar{m} = -\,\gamma\bar{s} \tag{2.39}$$

When an additional magnetic bias field $\overline{H_0} = \hat{z}H_0$ is present, it will exert a torque onto magnetic dipole:

$$\bar{\tau} = \mu_0\bar{m} \times \overline{H_0} = -\mu_0\gamma\bar{s} \times \overline{H_0} \tag{2.40}$$

$$\frac{d\bar{s}}{dt} = -\,\frac{1}{\gamma}\frac{d\bar{m}}{dt} = \bar{\tau} = \mu_0\bar{m} \times \overline{H_0} \tag{2.41}$$

$$\frac{d\bar{m}}{dt} = -\mu_0\gamma\bar{m} \times \overline{H_0} \tag{2.42}$$

(2.42) is called the equation of motion of magnetic dipole moment and it can be decomposed into scalar form:

$$\frac{dm_x}{dt} = -\mu_0 \gamma m_y H_0 \tag{2.43}$$

$$\frac{dm_y}{dt} = \mu_0 \gamma m_x H_0 \tag{2.44}$$

$$\frac{dm_z}{dt} = 0 \tag{2.45}$$

Then use both (2.43) and (2.44), we have:

$$\frac{d^2 m_x}{dt^2} + \omega_0^2 m_x = 0 \tag{2.46}$$

$$\frac{d^2 m_y}{dt^2} + \omega_0^2 m_y = 0 \tag{2.47}$$

$$\omega_0 = \mu_0 \gamma H_0 \tag{2.48}$$

and ω_0 is called *Larmor* or *precession* frequency. This phenomenon, known as electron spin resonance (ESR), occurs when the applied magnetic field resonates with the atom's net magnetic moment, which typically arises solely from electron spin. One of the solutions to (2.46) and (2.47) are:

$$m_x = A cos \omega_0 t \tag{2.49}$$

$$m_y = A sin \omega_0 t \tag{2.50}$$

(2.49) and (2.50) indicate that the magnetic dipole moment is circling around the z axis. In the real world, the additional damping term needs to be considered. So, a DC bias field magnetization will ultimately cause spin gradually aligned with its direction instead of precession indefinitely. Now consider in the bulk materials with a total magnetization $\bar{M}$ and a total amount of N spins,

doi:10.6342/NTU202501094

$$\overline{M} = N\overline{m} \tag{2.51}$$

$$\frac{d\overline{M}}{dt} = -\mu_0 \gamma \overline{M} \times \overline{H_0} \tag{2.52}$$

It should be noted that all these operations are assumed to be under saturated state. Otherwise, the ferrite materials are too lossy for RF signals to interact effectively. The saturated magnetization is $4\pi M_s = 300 - 5000\, Gauss$ [51]. If we apply AC signal perturbation $\overline{H}$ in addition to DC bias magnetic field $\overline{H_0}$ with $\overline{H} \ll \overline{H_0}$. M_s is the DC s saturation magnetization and $\overline{M}$ is the AC magnetization affected by $\overline{H}$ with $\frac{dM_s}{dt} = 0$:

$$\overline{H_t} = \hat{z}H_0 + \overline{H} \tag{2.53}$$

$$\frac{d\overline{M}}{dt} = -\mu_0 \gamma \overline{M} \times \overline{H_0} \tag{2.54}$$

$$\overline{M_t} = \hat{z}M_s + \overline{M} \tag{2.55}$$

$$\frac{dM_x}{dt} = -\mu_0 \gamma M_y (H_0 + H_z) + \mu_0 \gamma H_y (M_s + M_z) \tag{2.56}$$

$$\frac{dM_y}{dt} = \mu_0 \gamma M_x (H_0 + H_z) - \mu_0 \gamma H_x (M_s + M_z) \tag{2.57}$$

$$\frac{dM_z}{dt} = -\mu_0 \gamma M_x H_y + \mu_0 \gamma M_y H_x \tag{2.58}$$

Then considering $|\overline{H}| \ll H_0$, by applying that $|\overline{M}||\overline{H}| \ll |\overline{M}|H_0$ and $|\overline{M}||\overline{H}| \ll M_s|\overline{H}|$ with $\omega_0 = \mu_0 \gamma H_0$ and $\omega_m = \mu_0 \gamma M_s$,

$$\frac{dM_x}{dt} = -\omega_0 M_y + \omega_m H_y \tag{2.59}$$

$$\frac{dM_y}{dt} = \omega_0 M_x - \omega_m H_x \tag{2.60}$$

$$\frac{dM_z}{dt} = 0 \tag{2.61}$$

doi:10.6342/NTU202501094

Solving (2.59) and (2.60) we have:

$$\frac{d^2M_x}{dt^2}+\omega_0^2M_x=\omega_m\frac{dH_y}{dt}+\omega_0\omega_mH_x \tag{2.62}$$

$$\frac{d^2M_y}{dt^2}+\omega_0^2M_y=-\omega_m\frac{dH_x}{dt}+\omega_0\omega_mH_y \tag{2.63}$$

Consider AC field $\bar{H}$ in $e^{j\omega t}$ time-harmonic form, we can transform (2.62) and (2.63) into steady state AC phasor form:

$$(\omega_0^2-\omega^2)M_x=j\omega\omega_mH_y+\omega_0\omega_mH_x \tag{2.62}$$

$$(\omega_0^2-\omega^2)M_y=-j\omega\omega_mH_x+\omega_0\omega_mH_y \tag{2.63}$$

From (2.62) and (2.63), it can be observed that z component of $\bar{H}$ will not affect magnetic dipole moment. They can be rewritten into matrix form with a susceptibility tensor $[\chi]$:

$$\bar{M}=[\chi]\bar{H}=\begin{bmatrix}\chi_{xx} & \chi_{xy} & 0\\ \chi_{yx} & \chi_{yy} & 0\\ 0 & 0 & 0\end{bmatrix}\bar{H} \tag{2.64}$$

$$\chi_{xx}=\chi_{yy}=\frac{\omega_0\omega_m}{\omega_0^2-\omega^2} \tag{2.65}$$

$$\chi_{xy}=-\chi_{yx}=\frac{j\omega\omega_m}{\omega_0^2-\omega^2} \tag{2.66}$$

Susceptibility can be related to permeability with:

$$\bar{B}=\mu_0(\bar{M}+\bar{H})=[\mu]\bar{H} \tag{2.67}$$

$$[\mu]=\mu_0([U]+[\chi])=\begin{bmatrix}\mu & j\kappa & 0\\ -j\kappa & \mu & 0\\ 0 & 0 & \mu_0\end{bmatrix}\text{ with }\hat{z}\text{ bias} \tag{2.68}$$

doi:10.6342/NTU202501094

$$\mu = \mu_0(1+\chi_{xx}) = \mu_0\left(1+\chi_{yy}\right) = \mu_0\left(1+\frac{\omega_0\omega_m}{\omega_0^2-\omega^2}\right) \tag{2.69}$$

$$\kappa = -j\mu_0\chi_{xy} = j\mu_0\chi_{yx} = \mu_0\left(\frac{\omega\omega_m}{\omega_0^2-\omega^2}\right) \tag{2.70}$$

Permeability tensors in (2.68) form is called *gyrotropic*. It can also be biased in $\hat{x}$ or $\hat{y}$ directions:

$$[\mu] = \begin{bmatrix} \mu_0 & 0 & 0 \\ 0 & \mu & j\kappa \\ 0 & -j\kappa & \mu \end{bmatrix} \text{ with } \hat{x} \text{ bias} \tag{2.71}$$

$$[\mu] = \begin{bmatrix} \mu & 0 & j\kappa \\ 0 & \mu_0 & 0 \\ -j\kappa & 0 & \mu \end{bmatrix} \text{ with } \hat{y} \text{ bias} \tag{2.72}$$

It should be noted that magnetization $\bar{M}$ is typically measured in gauss (1 gauss [G] = 10^{-4} weber/m^2) and field strength $\bar{H}$ is measured in oersted ($4\pi \times 10^{-3}$ oersted [Oe] = 1 A/m). $\bar{B}$ will have the same numerical values as $\bar{H}$ only in a nonmagnetic material with $\mu_0 = 1[\frac{G}{Oe}]$. Hence, saturation magnetization is expressed as 4πM$_s$ gauss. The Larmor frequency is $f_0 = \frac{\omega_0}{2\pi} = \frac{\mu_0\gamma H_0}{2\pi} = 2.8[\frac{MHz}{Oe}] \times H_0[Oe]$; $f_m = \frac{\omega_m}{2\pi} = \frac{\mu_0\gamma \mathrm{Ms}}{2\pi} = 2.8[\frac{MHz}{Oe}] \times 4\pi\mathrm{Ms}[G]$.

Now we can consider the effect of damping loss on the spin precession. In (2.65) and (2.66), susceptibility will increase infinitely if the frequency is equal to Larmor frequency. This is known as *gyromagnetic resonance*. Loss can be included by making the Larmor frequency complex with a damping factor α:

$$\omega_0 \leftarrow \omega_0 + j\alpha \tag{2.73}$$

Then insert (2.73) into (2.65) and (2.66):

doi:10.6342/NTU202501094

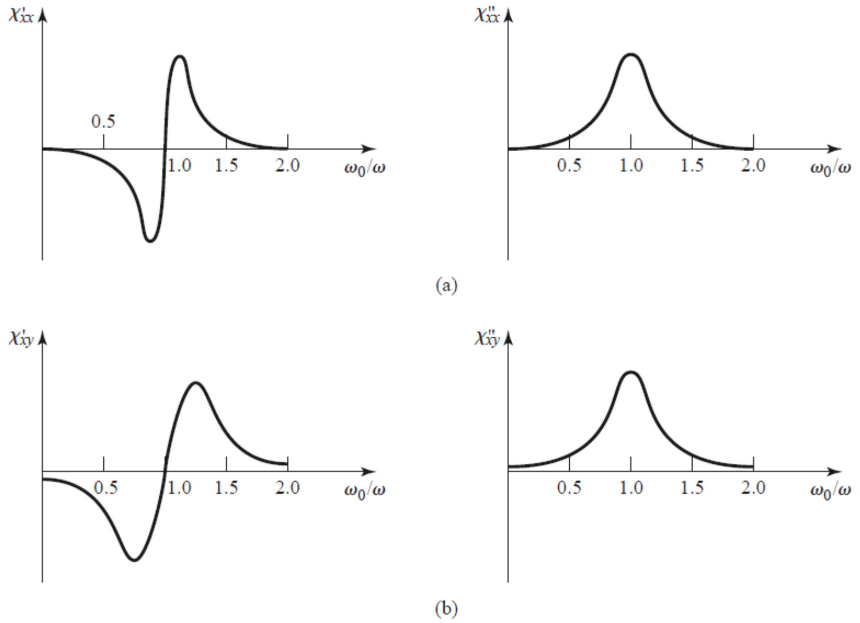

(a)

(b)

Fig. 2.14. Typical frequency response of (2.77), (2.78), (2.79) and (2.80). Reproduced from [51].

$$\omega_0 \leftarrow \omega_0 + j\alpha \tag{2.74}$$

$$\chi_{xx} = \chi'_{xx} - j\chi''_{xx} \tag{2.75}$$

$$\chi_{xy} = \chi'_{xy} + j\chi''_{xy} \tag{2.76}$$

$$\chi'_{xx} = \frac{\omega_0\omega_m(\omega_0^2 - \omega^2) + \omega_0\omega_m\omega^2\alpha^2}{[\omega_0^2 - \omega^2(1+\alpha^2)]^2 + 4\omega_0^2\omega^2\alpha^2} \tag{2.77}$$

$$\chi''_{xx} = \frac{\alpha\omega\omega_m[\omega_0^2 + \omega^2(1+\alpha^2)]}{[\omega_0^2 - \omega^2(1+\alpha^2)]^2 + 4\omega_0^2\omega^2\alpha^2} \tag{2.78}$$

$$\chi'_{xy} = \frac{\omega\omega_m[\omega_0^2 - \omega^2(1+\alpha^2)]}{[\omega_0^2 - \omega^2(1+\alpha^2)]^2 + 4\omega_0^2\omega^2\alpha^2} \tag{2.79}$$

$$\chi''_{xy} = \frac{2\omega_0\omega_m\omega^2\alpha}{[\omega_0^2 - \omega^2(1+\alpha^2)]^2 + 4\omega_0^2\omega^2\alpha^2} \tag{2.80}$$

doi:10.6342/NTU202501094

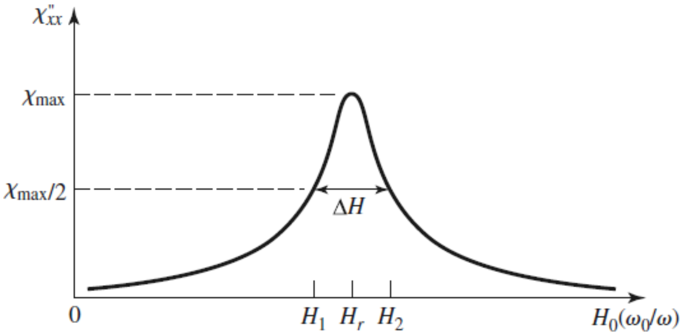

Fig. 2.15. Definition of *linewidth* ΔH. Reproduced from [51].

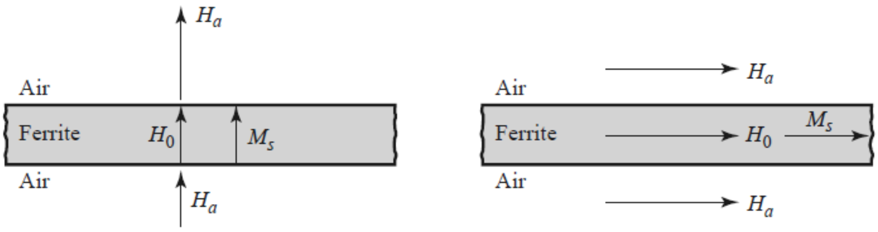

Fig. 2.16. Schematic graph of demagnetizing effect. Reproduced from [51].

The damping factor α is related to the *linewidth* ΔH, which represents the susceptibility behavior near gyromagnetic resonance. If we plot (2.78) with magnetic bias field H_0, we will have different Larmor frequency since $\omega_0 = \mu_0 \gamma H_0$. If the frequency ω is fixed, then the relation between (2.78) and H_0 is shown in Fig. 2.15. ΔH can be defined as the width of the magnetic field when the maximum χ''_{xx} decreases the to the half. If we assume that damping factor $\alpha \ll 1$ and use (2.78), then $\Delta\omega_0 \cong 2\alpha\omega$. Since $\omega_0 = \mu_0 \gamma H_0$, then $\Delta\omega_0 = \mu_0 \gamma \Delta H_0$ and $\Delta H = \frac{\Delta\omega_0}{\mu_0\gamma} = \frac{2\alpha\omega}{\mu_0\gamma}$. The bandwidth of ferromagnetic resonance (FMR) can be obtained from magnetic linewidth and depends on the material properties, particularly magnetic damping (α), and the geometry of the sample. For example, FeCoN thin film gives frequency linewidth or bandwidth around hundreds of MHz at around 2 GHz [52]. In addition, the typical bandwidth of a FBAR depends on its design, material stack, and application frequency. For example, AlN thin film gives around 70 MHz bandwidth at 2.7 GHz for a single resonator [53]. Ideally, we want both bandwidths to be as narrow as possible, which means low losses. We only want the radiation loss to be the main source of bandwidth widening.

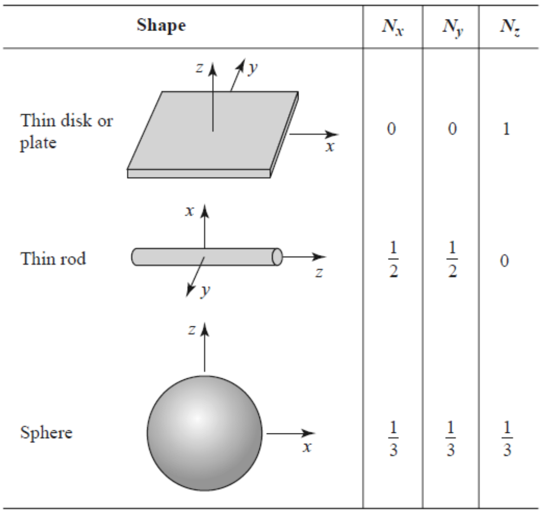

Shape	N_x	N_y	N_z
Thin disk or plate	0	0	1
Thin rod	$\frac{1}{2}$	$\frac{1}{2}$	0
Sphere	$\frac{1}{3}$	$\frac{1}{3}$	$\frac{1}{3}$

Fig. 2.17. Demagnetizing factors for different shapes. Reproduced from [51].

Another important factor should also be considered when mentioning resonance behaviors. Considering a thin plate with external magnetic bias field applied, it will respond differently to the parallel and perpendicular direction, as shown in Fig. 2.16. This is due to the continuity of magnetic field. It can be formulated as:

$$\overline{H} = \overline{H_e} - N\overline{M} \tag{2.81}$$

where N = N_x, N_y or N_z. N is called the *demagnetizing factor*. They are defined as $N_x+N_y+N_z=1$. Demagnetizing factors for different shapes are shown in Fig. 2.17. Now if we assume the magnetic field is biased and saturated in the z axis,

$$H_x = H_{xe} - N_x M_x \tag{2.82}$$

$$H_y = H_{ye} - N_y M_y \tag{2.83}$$

$$H_z = H_a - N_z M_s \tag{2.84}$$

where H_{xe} and H_{ye} is the external AC magnetic field and H_a is the external bias magnetic field. By using (2.64), (2.82) and (2.83), we have

doi:10.6342/NTU202501094

$$M_x = \chi_{xx}H_{xe} + \chi_{xy}H_{ye} - \chi_{xx}N_xM_x - \chi_{xy}N_yM_y \tag{2.85}$$

$$M_y = \chi_{yx}H_{xe} + \chi_{yy}H_{ye} - \chi_{yx}N_xM_x - \chi_{yy}N_yM_y \tag{2.86}$$

Solve (2.85) and (2.86) to find M_x and M_y, we have

$$M_x = \frac{\chi_{xx}\left(1+\chi_{yy}N_y\right) - \chi_{xy}\chi_{yx}N_y}{D}H_{xe} + \frac{\chi_{xy}}{D}H_{ye} \tag{2.87}$$

$$M_y = \frac{\chi_{yx}}{D}H_{xe} + \frac{\chi_{yy}(1+\chi_{xx}N_x) - \chi_{yx}\chi_{xy}N_x}{D}H_{ye} \tag{2.88}$$

$$D = (1+\chi_{xx}N_x)\left(1+\chi_{yy}N_y\right) - \chi_{yx}\chi_{xy}N_xN_y \tag{2.89}$$

The resonance condition can be achieved when set (2.89) = 0. Using (2.65) and (2.66) into (2.89), we have

$$\begin{aligned} D &= \left(1+\frac{\omega_0\omega_m}{\omega_0^2-\omega^2}N_x\right)\left(1+\frac{\omega_0\omega_m}{\omega_0^2-\omega^2}N_y\right) - \frac{\omega^2{\omega_m}^2}{(\omega_0^2-\omega^2)^2}N_xN_y \\ &= 0 \end{aligned} \tag{2.90}$$

Rearrange (2.90) and one can obtain resonance frequency to be

$$\omega = \omega_r = \sqrt{(\omega_0+\omega_mN_x)(\omega_0+\omega_mN_y)} \tag{2.91}$$

By using $\omega_0 = \mu_0\gamma H_0 = \mu_0\gamma(H_a - N_zM_s)$ and $\omega_m = \mu_0\gamma M_s$, finally we have

$$\omega_r = \mu_0\gamma\sqrt{[(H_a + (N_x - N_z)M_s][(H_a + \left(N_y - N_z\right)M_s]} \tag{2.92}$$

doi:10.6342/NTU202501094

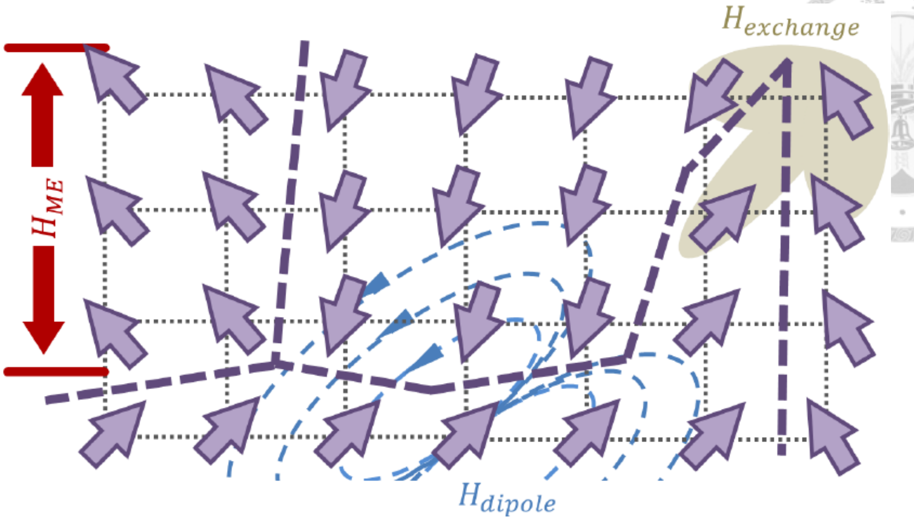

Fig. 2.18. Categories of micro-magnetic interactions in amorphous ferromagnetic materials. Reproduced from [37].

This is the famous *Kittel's equation* for deciding *ferromagnetic resonance (FMR)*. Ferromagnetic resonance in metallic ferromagnets is complicated by the effects of eddy currents. If we use the demagnetizing factor of thin plate in Fig. 2.17 with an out-of-plane z-axis directed bias magnetic field, (2.92) can be reduced to:

$$\omega_r = \mu_0\gamma\sqrt{(H_a - M_s)^2} = \mu_0\gamma(H_a - M_s) = \mu_0\gamma H_0 \tag{2.93}$$

So far, the effect of a magnetic field on a single spin is considered. However, various micro-magnetic interactions can influence spin dynamics, as shown in Fig. 2.18. Each interaction generates its own torque on the magnetic dipole. The concept of an effective field is introduced to calculate the torque for each interaction. This method utilizes the energy densities of micro interactions to derive an equivalent magnetic field [54]-[56]. For instance, an effective field caused by strain in a magnetostrictive material can reorient spins within the material but will not influence external spins. External spins only respond to the real magnetic fields generated by the material, which arise from the spins themselves. By combining the sum of DC internal and external applied fields and the sum of internal and external AC magnetic fields, the magnetization dynamics of the system can be accounted for by a new equation of motion. There will be equivalent local inertial term, restoring force term and driving force term in the second order differential equation [37].

Three kinds of microscopic interactions that should be considered, namely dipolar interactions, exchange interactions, and magneto-elastic interactions. In a magnetic material, each spin acts as a magnetic dipole, producing its own magnetic field. The field interacts with every other spin in the system. These fields are referred to as dipolar interaction. For the specific case of a uniformly magnetized ellipsoid, the dipolar field can be described by a simple expression of demagnetizing factor, as shown in Fig. 2.17. This interaction has also been called shape anisotropy.

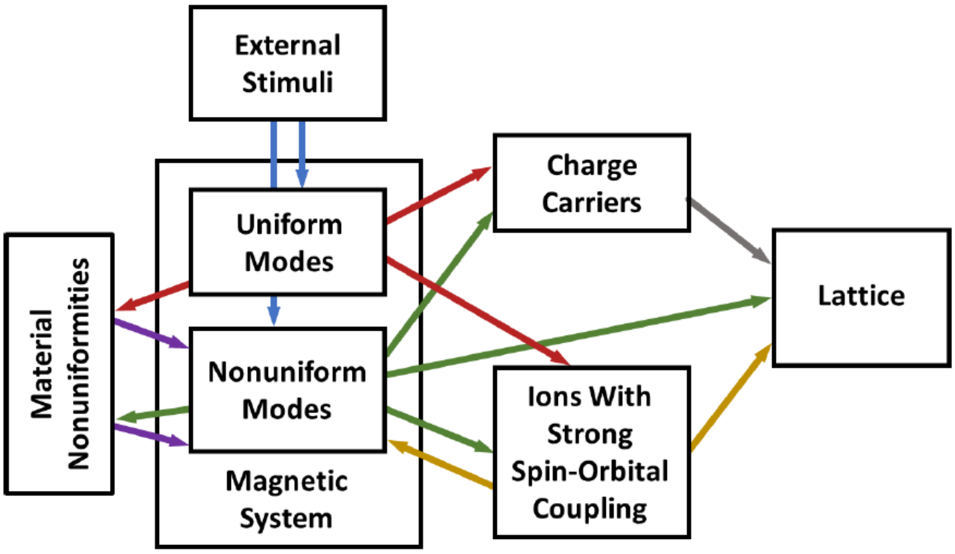

Fig. 2.19. Schematic illustrating the different mechanisms within a magnetic material. Reproduced from [55].

Electrons obey the Pauli Exclusion Principle [57]. This principle is a purely quantum mechanical phenomenon with no macro-scale equivalent. Consequently, neighboring electrons will act "force" on each other, ensuring their quantum states remain distinct.

doi:10.6342/NTU202501094

This interaction, known as the exchange interaction, determines the magnetic classification of a material, as shown in Fig. 2.12. In ferromagnetic materials, the exchange interaction energy is minimized when each dipole is aligned [38].

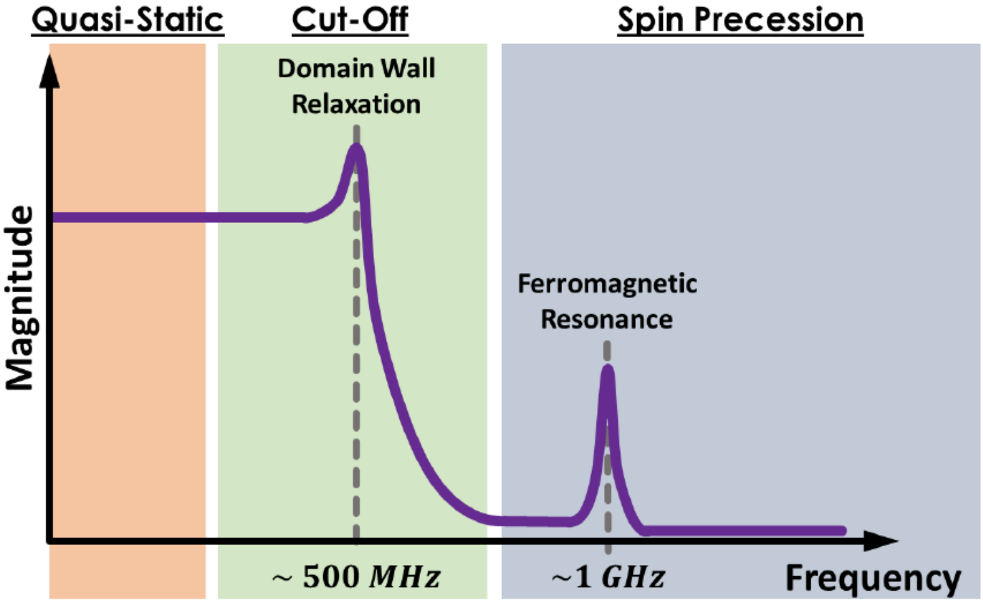

Fig. 2.20. Trend of the instantaneous susceptibility for an arbitrary magnetic material, divided into three zones based on frequency: quasi-static, cut-off, and spin precession. Reproduced from [37].

The exchange interactions discussed along depend on the relative spacing between spins within the material. If these spacings are altered, such as through crystal lattice strain, the equilibrium magnetization must adjust to account for the resulting changes in internal interactions. This phenomenon forms the basis of magneto-elastic interaction. When an external magnetic field is applied, the magnetization rotates, causing the material to deform. It is important to note that magnetostrictive stress, and the resulting strain, will saturate with increasing magnetic field. When the magnetic field strengthens, magnetization aligns with it, leading to an increase in strain along that direction. However, once the material reaches its saturation magnetization, the magnetostrictive strain also saturates at a value known as saturation magnetostriction, λs. By considering all the

doi:10.6342/NTU202501094

micromagnetic interactions as well as damping effect, magnetization dynamics can be summarized in Fig. 2.19.

As seen previously, the dynamics of magnetization strongly depend on both frequency and magnetic structure [58]. The frequency response typically follows the trend in Fig. 2.20, which can be categorized into three regions. At lower frequencies, susceptibility remains constant, matching the DC value. It is identified as quasi-static zone, mostly driven by domain wall motion. Domain walls have a cut-off frequency, usually in the hundreds of MHz, beyond which they can no longer change with the field. It is identified as the cut-off zone, where the domain wall effect becomes negligible. As the frequency goes higher, around 1 GHz or above, susceptibility is primarily influenced by spin precession. This behavior is low until it peaks near ferromagnetic resonance (FMR) frequency, after which it drops again to near zero. However, above the FMR frequency, spin waves can be driven, and domain wall motion no longer contributes when the material is fully saturated. To summarize, dynamic magnetization can be grouped into six categories based on the three zones including quasi-static, cut-off, or spin precession and the two internal states including single domain or multi-domain. It’s crucial to note that the dynamics characterized in one regime may not apply to others. Therefore, when analyzing a magnetic system, it is essential to characterize it within the category it will operate in, as measurements from one category may not predict performance accurately in another [37].

2.4 Non-magnetostrictive Materials

As discussed in the previous section, the dynamics of magnetization are significantly influenced by the magnetic structure, operating frequency, and electron spin dynamics. A

doi:10.6342/NTU202501094

more well-known manifestation of magnetoelastic coupling is the magnetostrictive effect, which is generally observed at lower frequencies. This phenomenon occurs when a material experiences a change in its dimensions upon exposure to a magnetic field, a behavior known as magnetostriction. First identified by Joule in 1842, magnetostriction was observed when an iron rod increased in length when subjected to a weak magnetic field along its length. The fractional change in length, denoted as $\lambda = \Delta l/l$, where Δl is the change in length and l is the original length, represents strain and distinguishes it from mechanical stress-induced strain. The value of λ at magnetic saturation is referred to as saturation magnetostriction, λ_s, which is commonly implied when "magnetostriction" is mentioned without further clarification [59].

Magnetostriction is a fundamental property in pure materials, but even in highly magnetic substances, the effect tends to be relatively small, with λ_s typically on the order of 10^{-5}. To provide perspective, for materials like iron or steel, which have a Young's modulus around 30×10^6 lb/in², a strain of 10^{-5} corresponds to an applied stress of approximately 300 lb/in² (about 2 MPa or 0.2 kg/mm²). When comparing magnetostrictive strain to thermal expansion, metals and alloys often exhibit thermal expansion coefficients around 20×10^{-6} per K. In weaker magnetic materials, the magnetostrictive effect is about two orders of magnitude smaller and is only noticeable under very strong magnetic fields. Our discussion will concentrate on strongly magnetic materials, as the magnetostrictive effect in weak magnetic substances is minimal [59].

The saturation longitudinal magnetostriction (λ_s) can vary, being positive, negative, or, in certain alloys at specific temperatures, zero. The value of λ is dependent on the magnetization level and, consequently, the applied magnetic field (H). As shown in Fig.

2.22, λ typically changes with H for materials exhibiting positive magnetostriction. Magnetization occurs through two mechanisms: domain-wall motion and domain rotation, with most magnetostrictive effects arising from domain rotation.

At technical saturation, where the material becomes a single-domain magnet aligned with the field, any further increase in H results in only a slight additional strain. This gradual change in λ with H is known as forced magnetostriction. The logarithmic scale of H in Fig. 2.21 emphasizes the strong field strengths required for this effect to be noticeable. Forced magnetostriction arises from an increased level of spin order that can be achieved under very high fields, a process known as the paraprocess.

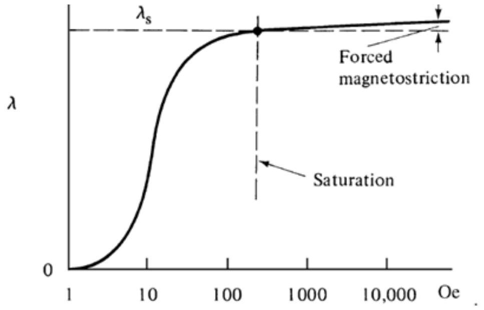

Fig. 2.21. Schematic illustrating the relationship between magnetostriction and magnetic field, with the magnetic field scale shown logarithmically. Reproduced from [59].

The ideal saturation magnetostriction, λ_{si}, of a cubic crystal, measured from its ideal demagnetized state, varies along a direction defined by the direction cosines β_1, β_2, β_3 in relation to the crystal axes. As the crystal approaches saturation, the magnetization along a direction characterized by direction cosines α_1, α_2, α_3 relative to the crystal axes can be expressed using the following formula:

:

doi:10.6342/NTU202501094

$$\lambda_{si} = \frac{3}{2}\lambda_{100}(\alpha_1^2\beta_1^2 + \alpha_2^2\beta_2^2 + \alpha_3^2\beta_3^2 - \frac{1}{3}) + 3\lambda_{111}(\alpha_1\alpha_2\beta_1\beta_2 + \alpha_2\alpha_3\beta_2\beta_3 + \alpha_3\alpha_1\beta_3\beta_1) \quad (2.94)$$

Here, λ_{100} and λ_{111} represent the saturation magnetostrictions measured when the crystal is magnetized and the strain is evaluated along the <100> and <111> directions, respectively. This equation applies to crystals with <100> or <111> as easy magnetization directions. Typically, when the strain is measured in the same direction as the magnetization, $\beta_1, \beta_2, \beta_3 = \alpha_1, \alpha_2, \alpha_3$, and the equation simplifies to:

$$\lambda_{si} = \frac{3}{2}\lambda_{100}(\alpha_1^4 + \alpha_2^4 + \alpha_3^4 - \frac{1}{3}) + 3\lambda_{111}(\alpha_1^2\alpha_2^2 + \alpha_2^2\alpha_3^2 + \alpha_3^2\alpha_1^2) \quad (2.95)$$

This can be further reduced to:

$$\lambda_{si} = \lambda_{100} + 3(\lambda_{111} - \lambda_{100})(\alpha_1^2\alpha_2^2 + \alpha_2^2\alpha_3^2 + \alpha_3^2\alpha_1^2) \quad (2.96)$$

(2.96) is referred to as the *two-constant* equation for magnetostriction. The common

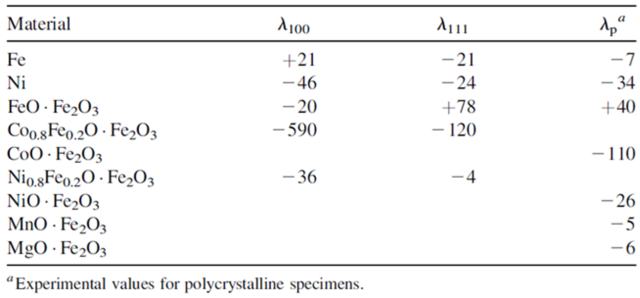

Material	λ_{100}	λ_{111}	$\lambda_p{}^a$
Fe	+21	−21	−7
Ni	−46	−24	−34
$FeO \cdot Fe_2O_3$	−20	+78	+40
$Co_{0.8}Fe_{0.2}O \cdot Fe_2O_3$	−590	−120	
$CoO \cdot Fe_2O_3$			−110
$Ni_{0.8}Fe_{0.2}O \cdot Fe_2O_3$	−36	−4	
$NiO \cdot Fe_2O_3$			−26
$MnO \cdot Fe_2O_3$			−5
$MgO \cdot Fe_2O_3$			−6

[a] Experimental values for polycrystalline specimens.

Fig. 2.22. Magnetostriction of Cubic Substances (Units of 10^{-6}). Reproduced from [59].

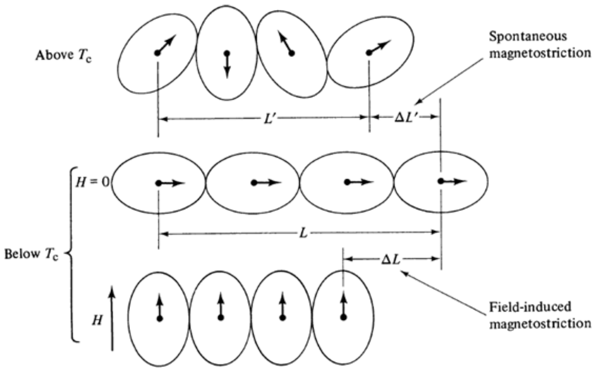

Fig. 2.23. Schematic illustrating the magnetostriction mechanism. Reproduced from [59].

magnetostriction constants for cubic materials are summarized in Fig.2.22.

If the magnetostriction of a material is isotropic, we can set $\lambda_{100} = \lambda_{111} = \lambda_{si}$, simplifying the equation from (2.94) to:

$$\lambda_\theta = \frac{3}{2}\lambda_{si}(\cos^2\theta - \frac{1}{3}) \tag{2.97}$$

λ_θ refers to the saturation magnetostriction at an angle θ relative to the direction of magnetization, as determined from the ideal demagnetized state. θ is the angle between two directions defined by cosines and $\cos\theta = \alpha_1\beta_1 + \alpha_2\beta_2 + \alpha_3\beta_3$

Magnetostriction primarily results from spin-orbit coupling, a mechanism also responsible for crystal anisotropy. While spin-orbit coupling itself is relatively weak, it can be influenced by magnetic fields as small as a few hundred oersteds. These fields are enough to cause spins to shift from their preferred orientation. The connection between magnetostriction and spin-orbit coupling can be illustrated through Fig. 2.23, which shows a sequence of atoms within a crystal lattice. In this diagram, black dots represent atomic nuclei, arrows indicate the net magnetic moment per atom, and oval shapes depict the non-spherical electron clouds around each nucleus [59].

In the upper row of the figure, atoms are depicted in a paramagnetic state above the critical temperature (Tc). If spin-orbit coupling were exceptionally strong, below Tc, spontaneous magnetization would align the spins and electron clouds in a direction determined by the crystal’s anisotropy (e.g., from left to right). This alignment would push the nuclei further apart, leading to spontaneous magnetostriction, shown as ΔL'/L'. When a strong vertical magnetic field is applied, the spins and electron clouds rotate by 90 degrees, causing the domain to undergo magnetostrictive strain, represented by ΔL/L. Although the strains shown in the diagram are significant, about 0.3, the actual magnetostrictive strain experienced in crystals or domains during magnetization changes is usually much smaller, typically on the order of 10^{-5}.

doi:10.6342/NTU202501094

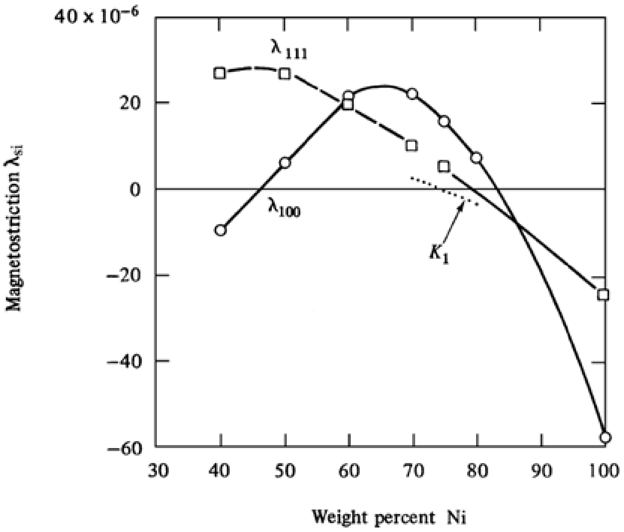

Fig. 2.24. Iron-nickel alloys: Variations in saturation magnetostriction with changes in nickel content. Reproduced from [59].

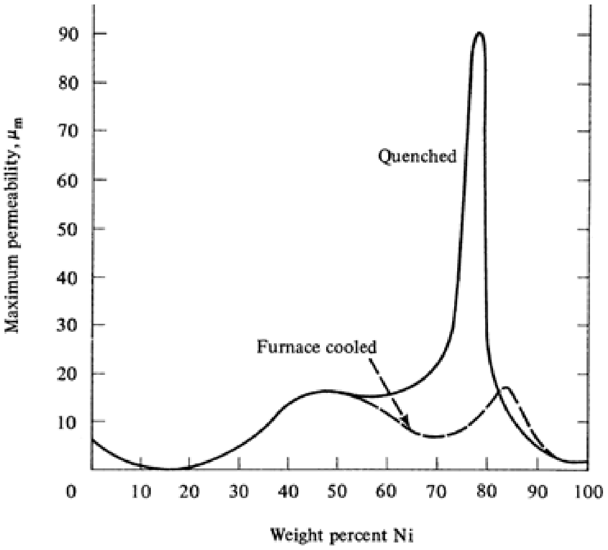

Fig. 2.25. Peak permeabilities of iron-nickel alloys under different heat treatments. Reproduced from [59].

Rare-earth metals, however, behave differently from other materials. Many of these metals exhibit ferromagnetism at temperatures significantly below room temperature and show pronounced spin-orbit coupling due to their unquenched orbital moments. Moreover, their electron clouds are notably non-spherical. When a magnetic field is applied, the rotation of spins causes substantial distortion due to the orbital motion. For example, at

22K, dysprosium (Dy) has a saturation magnetostriction of approximately 4.5×10^{-3} in its basal plane, which is nearly 100 times greater than that observed in typical metals and alloys. Additionally, some rare-earth compounds, particularly those with transition metals like Fe, Ni, and Co, exhibit Curie points above room temperature and display exceptionally large magnetostriction values.

Furthermore, Permalloys are a type of nickel-iron alloy, typically composed of either 50% or 80% nickel, with the numerical prefix in their name indicating the proportion of nickel. These alloys are well known for their high magnetic permeability at low magnetic fields, minimal energy loss, and ability to be processed into extremely thin sheets. Permalloys are often used in applications where exceptional magnetic properties are required, and cost is less of a concern. Originally developed for use in the telephone system between 1913 and 1921, Permalloys continue to be widely employed in a variety of industries. Modern applications of Permalloy include magnetic shielding, stepping motors, current sensors, and torque sensors. As shown in Fig. 2.24, the alloy's low magnetostriction and high permeability are key features. The high permeability of Permalloy is linked to its low values of magneto-crystalline anisotropy (K) and magnetostriction (λ). A reduced K value lowers domain-wall energy and increases domain-wall thickness, allowing less resistance to domain-wall movement. Likewise, a small λ value reduces the impact of micro-stresses. As depicted in Fig. 2.25, both $K1$ and $\lambda111$ approach zero when the nickel content is just below 80%, and $\lambda100$ remains relatively small, which is typical of 78 Permalloy.

doi:10.6342/NTU202501094

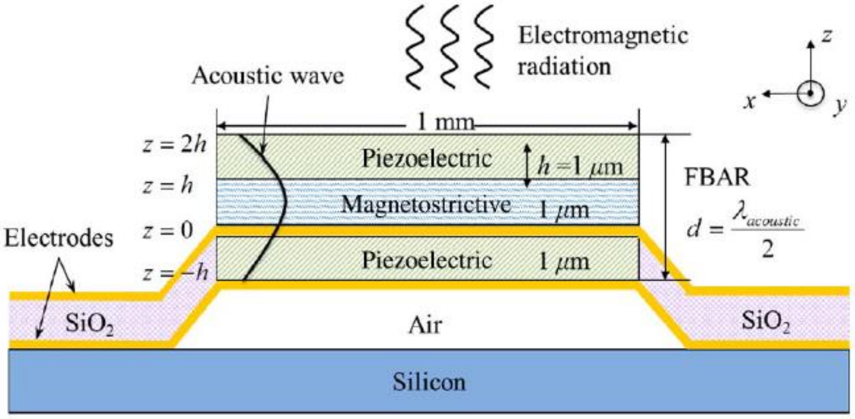

Fig. 2.26. An electric current is applied to the electrodes on either side of the bottom piezoelectric layer, initiating BAW resonance via the converse piezoelectric effect. Reproduced from [14].

2.5 Modelling on Multiferroic Antenna

For more comprehensive modelling on multiferroic antenna, there are mainly numerical and analytical efforts. The first work on numerical modelling is proposed by Yao [14], [15], [60] and later work by Cai [62]. The work on analytical modelling is done by Domann [63] and then by Ippet-Letembet [64]. In this section, I will only go through the assumptions and conclusions drawn so far by Yao.

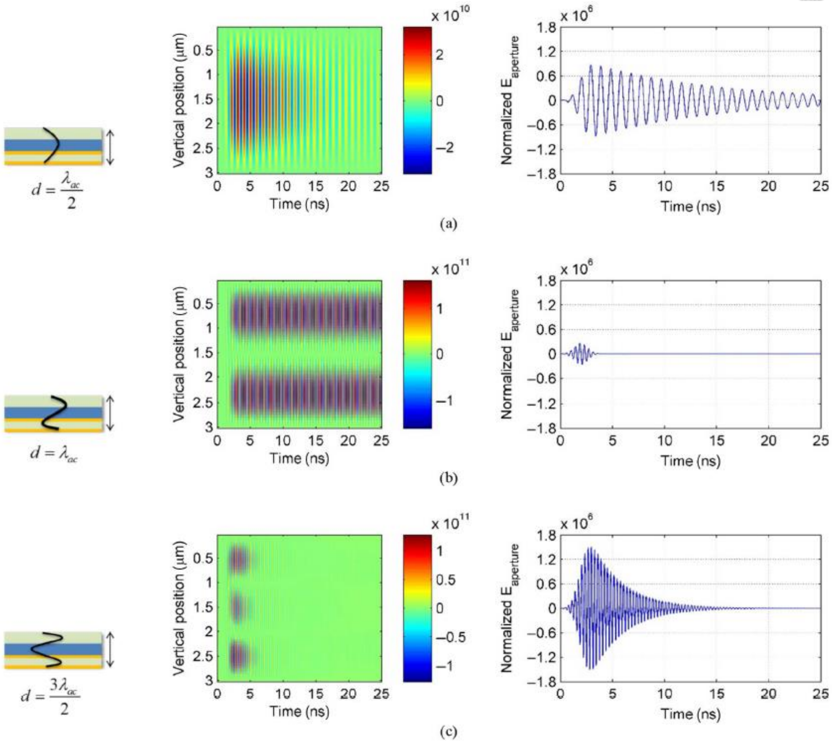

Fig. 2.27. From left to right: Standing wave distribution of the vertical stress field for the first three BAW resonant modes. Time-dependent stress profiles across the BAW structure. Third column: Normalized aperture electric field. (a) f=1.03 GHz (b) f=2.28 GHz (c) f=3.17 GHz. Reproduced from [14].

In [14], the idea of using bulk acoustic wave (BAW) technology to create multiferroic antennas is introduced for the first time. These antennas differ from conventional designs by utilizing dynamic electric flux (displacement current) or magnetic flux to generate radiation, rather than relying on conductive current. This is achieved by inducing dynamic strain in a thin piezoelectric or piezomagnetic material, which produces a dynamic flux density. This flux density, in turn, creates the aperture field on the surface of the material. Strain-mediated antennas provide several benefits over traditional antennas based on conductive current. They eliminate the Ohmic losses typically associated with current conduction, leading to improved radiation efficiency. Furthermore, by using strain-induced magnetic flux as the radiation source, these antennas can reduce platform effects, as the image effect from the conductive platform amplifies, rather than diminishes, the radiation. Additionally, these antennas can be designed with little or no conductive elements above the ground plane, which results in reduced visibility and enhanced resistance to strong interference.

The analysis uses the linear form of constitutive equations based on the coupling between piezomagnetic and piezoelectric materials. From this, the lower bound of the quality factor for a single magnetostrictive layer is derived as:

$$Q_{bound} = \omega \frac{W_{Total}}{P_{rad}} = \omega \frac{W_B / k_H^2}{P_{rad}} = \frac{1}{k_H^2} \frac{1}{\mu_r k_0 h} \tag{2.98}$$

,where Q_{bound} is the lower bound of the radiation Q factor for the antenna when the stored energy in the magnetostrictive layer is the only primary form of the stored energy. It can be observed that the quality factor can be improved by enhancing the permeability of and mechanical-to-magnetic coupling coefficient. For more practical lower bound, additional structure should be considered with the excitation source from piezoelectric layer as shown in Fig. 2.26. There will be additional mechanical energy stored in the piezoelectric layer in addition to magneostrictive layer. The topmost layer is intended to

doi:10.6342/NTU202501094

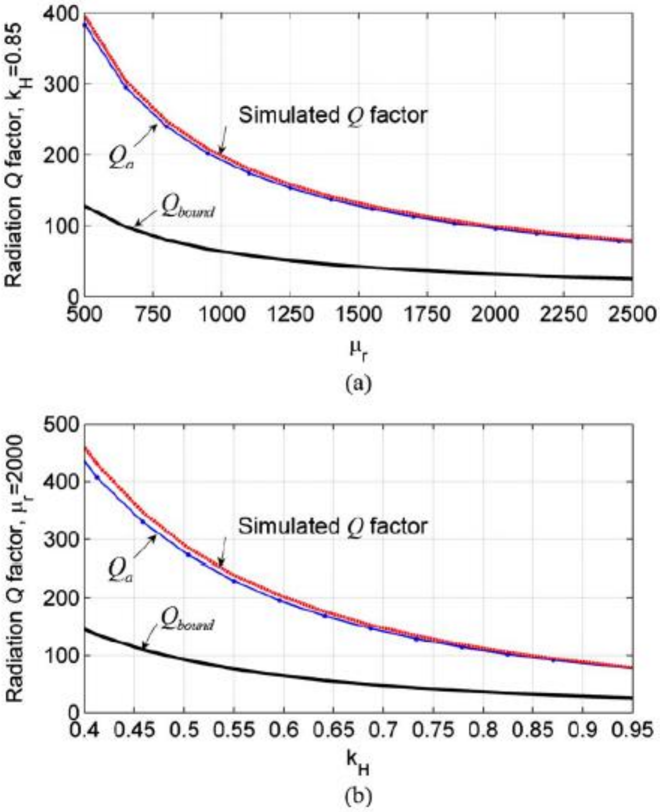

Fig. 2.28. Simulated Q factor versus analytical Q factor. Reproduced from [14].

adjust the maximum amplitude of resonant stress to be overlapped with magnetostrictive layer. With proper rescaling, the radiation quality factor of the BAW structure is derived as 3 times of (2.98).

After initial investigation of lower bound of quality factor, the one-dimensional (1D) finite difference time domain (FDTD) technique is applied. In the simulated structure, the electrical flux density with the form of Gaussian modulated pulse $D(t) = e^{\frac{-(t-t_0)^2}{2T^2}}\cos(2\pi f t)$ as the excitation source is given between the bottom piezoelectric layer. Then, the stress profile of the middle of magnetostrictive layer and the aperture electric field is shown in Fig. 2.27. Several observations can be made from Fig. 2.27. First, the slowly decaying behavior of stress profile indicates the damping effect of magnetostrictive layer. Since the simulation is assumed to be lossless, the only possible damping loss is radiation loss. Also, in the second mode of 2.28 GHz, the aperture electric

doi:10.6342/NTU202501094

field is minimized due to the inverse phase distribution of magnetostrictive layer. This indicates that the radiation is mainly due to the magnetostrictive layer. When the radiation source is with the distribution of opposite phase, the radiation will disappear. In the last part of this work, the simulated Q factor is compared to the analytical Q factor (2.98), as shown in Fig. 2.28. The simulated one from 1-D FDTD code agrees well with the analytical lower bound of such antenna. It also predicts a potential radiated power per square to be $P_{rad} = \frac{\eta_0 H_{dynamic}^2}{2} \cdot 10^{-6} = 0.3\, W/mm^2$. To summarize, this work represents a first pilot study into the feasibility of multiferroic antenna. Although this work is done under lossless, isotropic, 1-D and linearized assumptions, it shows the potential to implement such an antenna. The radiation can be enhanced by increasing permeability as well as magnetic-to-mechanical coupling constant of magnetostrictive materials.

In 2020, Yao continued the work to further include Landau–Lifshitz–Gilbert (LLG) equation which is coupled into Maxwell's equations for electromagnetic (EM) wave propagation and Newton's law for acoustic behavior [60]. In fact, all the current commercially available solver cannot predict non-linear magnetic material response together with coupled physics. For example, the traditional EM or mechanical solver can only have predefined permeability tensors. The radiation characteristics with multiferroic antenna cannot be predicted. Hence, this work deals with the fundamental challenge of three coupled physics with three equations by implementing unconditionally stable finite-difference time-domain (FDTD) method with alternating direction implicit (ADI) algorithm:

$$\frac{\partial \bar{M}}{\partial t} = \mu_0 \gamma (\bar{M} \times \bar{H}_{eff} - \frac{\alpha}{|\bar{M}|} \bar{M} \times \frac{\partial \bar{M}}{\partial t}) \tag{2.99}$$

doi:10.6342/NTU202501094

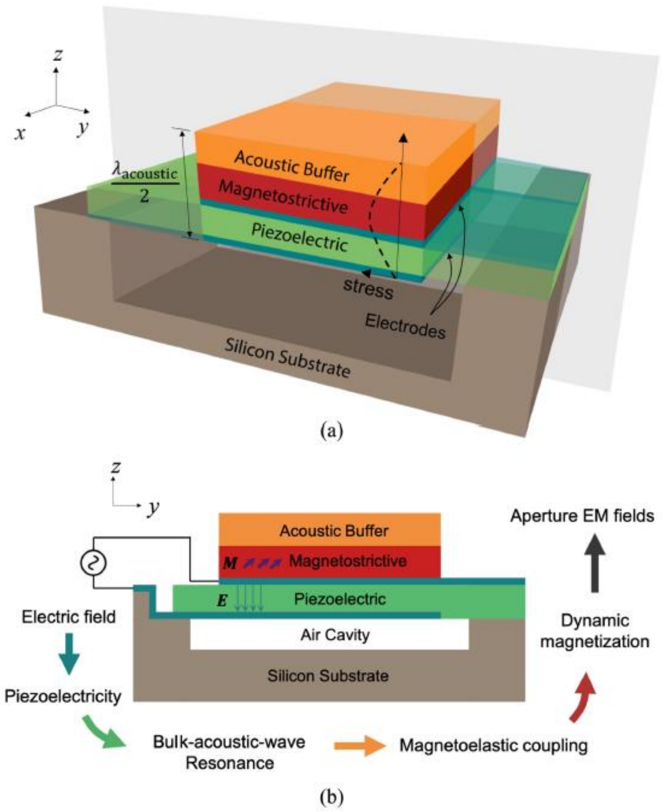

Fig. 2.29. Simulated BAW-mediated antenna. Reproduced from [60].

$$\nabla \times \bar{E} = -\frac{\partial \bar{B}}{\partial t}, \nabla \times \bar{H} = \sigma \bar{E} + \frac{\partial \bar{D}}{\partial t} \tag{2.100}$$

$$\nabla \cdot T = \rho \frac{\partial \bar{v}}{\partial t}, \nabla_S \bar{v} = \frac{\partial S}{\partial t} \tag{2.101}$$

, where T is the stress field tensor in N/m^2, S is the strain field tensor without the unit, ρ is the mass density of the material in N/m^3 and $\bar{v}$ is the particle velocity in m/s. Here, $\bar{E}$ and $\bar{D}$ are written in vector form, which is equivalent to matrix form $E = \begin{bmatrix} E1 \\ E2 \\ E3 \end{bmatrix}$ and $D = \begin{bmatrix} D1 \\ D2 \\ D3 \end{bmatrix}$ in the previous part. In this work, only longitudinal mode is considered without full tensor form of Newton's law.

Like previous work in [14], the structure of multiferroic composite based on

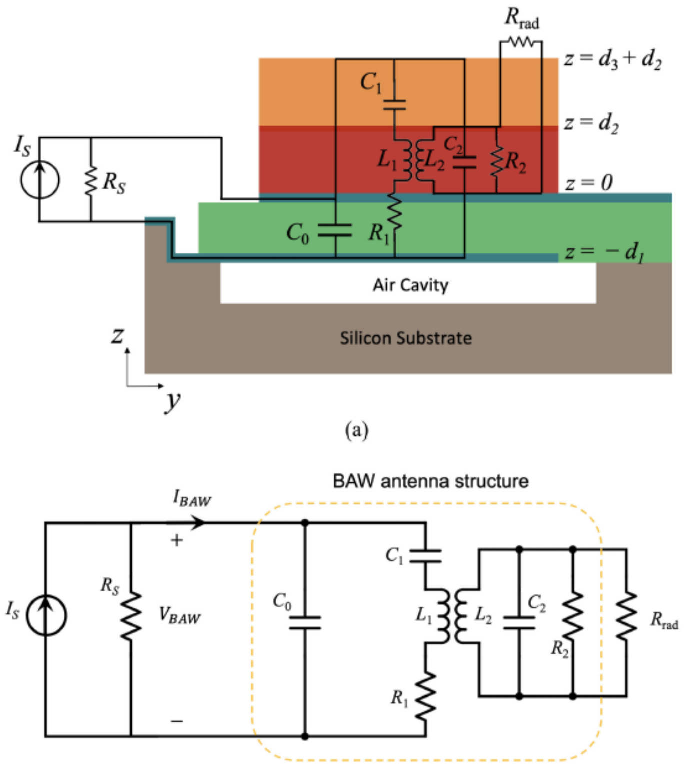

(a)

(b)

Fig. 2.30. Simulated BAW-mediated antenna. Reproduced from [60].

piezoelectric/magnetostrictive layer is shown in Fig. 2.29. The basic working principle of LLG equation indicates that when ferrite and ferromagnetic materials are exposed to an external magnetic field, the magnetization gradually aligns with the effective field. It will rotate until it reaches equilibrium, where the magnetic spin experiences minimal energy. In this work, only three terms of effective magnetic field are considered:

$$\bar{H}_{eff} = \bar{H} + \bar{H}_0 + \bar{H}_m \tag{2.102}$$

$$\bar{H}_m = d_B T \tag{2.103}$$

, where $\bar{H}$ is the dynamic magnetic field of the EM wave, $\bar{H}_0$ is the magnetic bias field, $\bar{H}_m$ is the equivalent magnetic field induced by stress and d_B is the piezomagnetic strain constant tensor. The exchange field $\bar{H}_{ext}$ and anisotropy field $\bar{H}_a$ are ignored under saturated and isotropic ferromagnetic material assumptions.

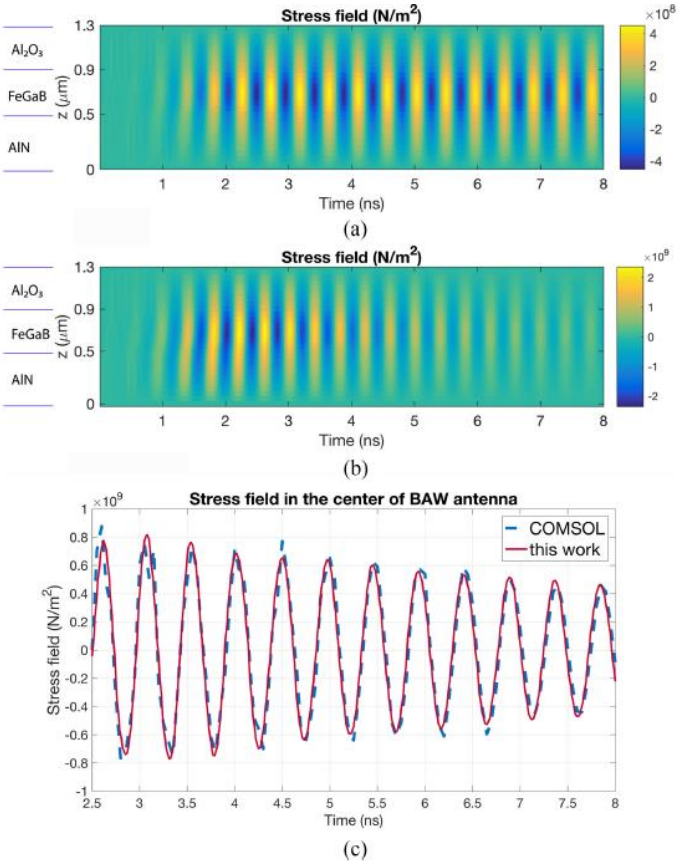

Fig. 2.31. Simulated results with on/off piezomagnetic coupling compared with COMSOL pure mechanical simulation. Reproduced from [60].

The composite under simulation is formed by AlN, FeGaB and Al_2O_3 with the thickness of 500, 400 and 400 nm respectively. The planar dimensions are 100 μm × 100 μm with a total thickness of 1300 nm. Again, the current source is set as the modulated Gaussian pulse in 50 ohms. The simulated structure and equivalent circuit are shown in Fig. 2.30. The results are validated by comparing the on/off state of piezomagnetic coupling, as shown in Fig. 2.31. When the piezomagnetic coupling is turned off and set to zero, the stress field corresponds well to the COMSOL pure mechanical simulation. Also, the field decays slowly only due to the mechanical damping. When the piezomagnetic coupling is turned on, the stress field decays fast due to radiation loss and Gilbert damping loss. The radiation efficiency is defined as $\eta_{rad} = \frac{P_{rad}}{P_{BAW}} \times 100\%$. The radiation efficiency is increased up from the planar dimension of 100 μm × 100 μm to

doi:10.6342/NTU202501094

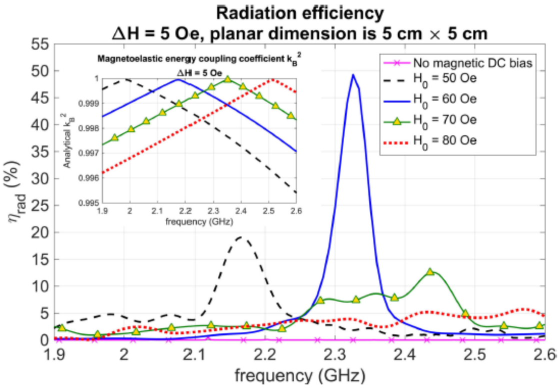

Fig. 2.32. Simulated radiation efficiency versus bias field. Reproduced from [60].

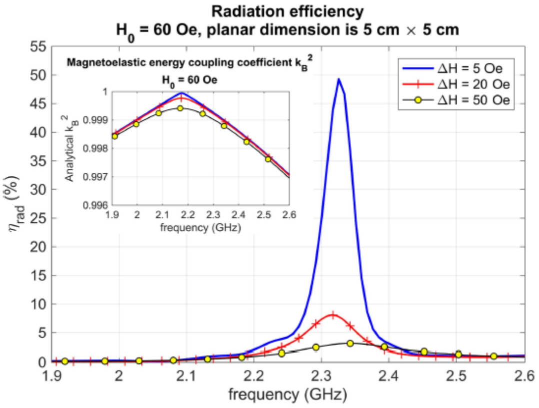

Fig. 2.33. Simulated radiation efficiency versus magnetic linewidth. Reproduced from [60].

the planar dimension of 5000 μm × 5000 μm. In Fig. 2.32, it can be found that the FMR frequency shifts from 1.98 GHz to 2.51 GHz as the magnetic DC bias field increases from 50 Oe to 80 Oe. At a magnetic bias of 60 Oe, the FMR frequency aligns with the BAW resonance frequency, resulting in a peak radiation efficiency of 49% for the BAW antenna. If there's no magnetic bias, then the spins won't align in the same direction. Hence, the total radiation will be close to zero. In Fig. 2.33, the relation between Gilbert damping coefficient α or the magnetic linewidth ΔH and radiation efficiency is shown. As anticipated, a larger linewidth leads to reduced radiation efficiency. To achieve optimal performance, minimizing magnetic losses and aligning the FMR with the BAW resonance is essential.

Additionally, when conductive materials are subjected to time-varying magnetic fields, they naturally develop internal circulating currents, commonly referred to as eddy currents. These currents can lead to significant power loss, particularly in high-permeability ferromagnetic materials, which are also typically good electrical conductors. This issue is addressed in [59], where the suppression of eddy current losses is analyzed in a specific setup.

The study begins with a theoretical model involving an infinite sheet of uniform current positioned above an ideal perfect electric conductor (PEC) ground plane. A ferromagnetic substrate is placed in between as the intermediary material. In the scenario where this substrate is considered non-conductive (i.e., its electrical conductivity is set to zero), the system achieves a radiation efficiency of about 25%. However, once the ferromagnetic material is assumed to have realistic conductive properties, significant eddy currents are induced within it, severely degrading radiation efficiency to approximately 2.2%, as illustrated in Fig. 2.34.

To address this efficiency drop, the study explores a practical solution: segmenting the ferromagnetic bulk into multiple thin laminations. This layered approach effectively interrupts the formation of large eddy current loops, thereby reducing conductive losses. Results indicate that using 10 layers can raise the radiation efficiency from 2.2% to 11.8%, as shown in Fig. 2.35.

doi:10.6342/NTU202501094

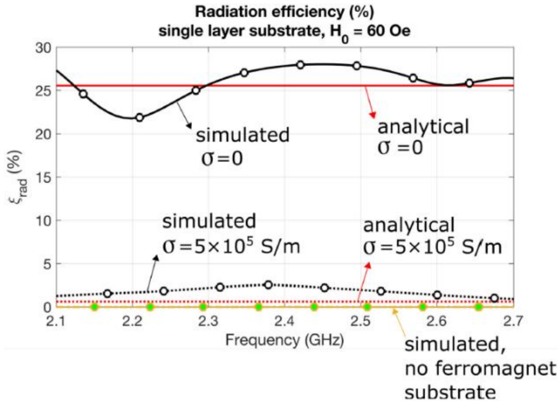

Fig. 2.34. Simulated and analytical radiation efficiency by comparing three cases. One with the ferromagnetic material without conductivity, one with the ferromagnetic material with conductivity and without ferromagnetic material. It is shown that the eddy current loss will greatly downgrade the radiation enhancement from FMR. Reproduced from [59].

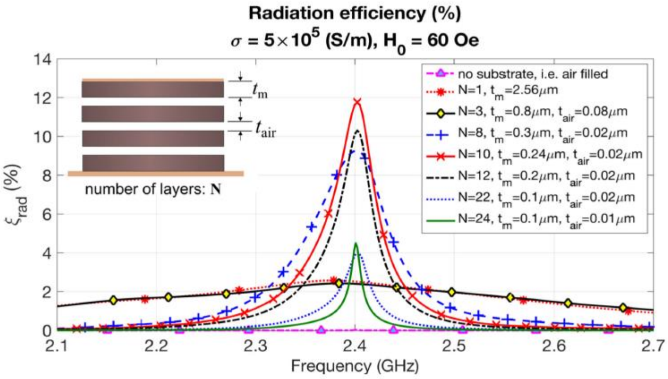

Fig. 2.35. The ferromagnetic layer is cut into thin layers to break down the eddy current loops. It is shown that the radiation efficiency can be optimized around the layer of 10. Reproduced from [59].

Chapter 3 Review Work Regarding Experimental Proof of Multiferroic Antenna

Chapter 2 covers the material fundamentals, operating principles, and theoretical modeling of multiferroic antennas. In this chapter, we focus on experimental validation of multiferroic antennas. Since early research in this field has been largely theoretical, several fundamental questions regarding experimental mechanisms remain unanswered. Accordingly, this chapter provides a review of relevant experimental evidence, focusing on magnetoelectric-coupled antennas, sensors based on the delta-E effect, and the phenomenon of acoustic wave-excited ferromagnetic resonance (FMR). These phenomena are potentially related to our experimental approach and may offer valuable insights for interpreting our results.

3.1 Magnetoelectric Antennas

The first experimental demonstration of a multiferroic antenna was conducted by Nan et al. in 2017 [65]. While they referred to it as “magnetoelectric,” the device shared the same composite structure as a multiferroic antenna. Magnetoelectric (ME) coupling describes the interaction between magnetic and electric fields, a fundamental concept, whereas multiferroic coupling specifically involves multiple ferroic materials, such as ferromagnetic and ferroelectric materials.

Their study began with a 60.68 MHz nanoplate resonator (NPR), comparing FeGaB/AlN structures with non-magnetic Cu/AlN counterparts. The measurement setup is shown in Fig. 3.1. During reception, the FeGaB magnetic layer in the ME antenna detects the H-component of EM waves, inducing oscillating strain and generating a piezoelectric

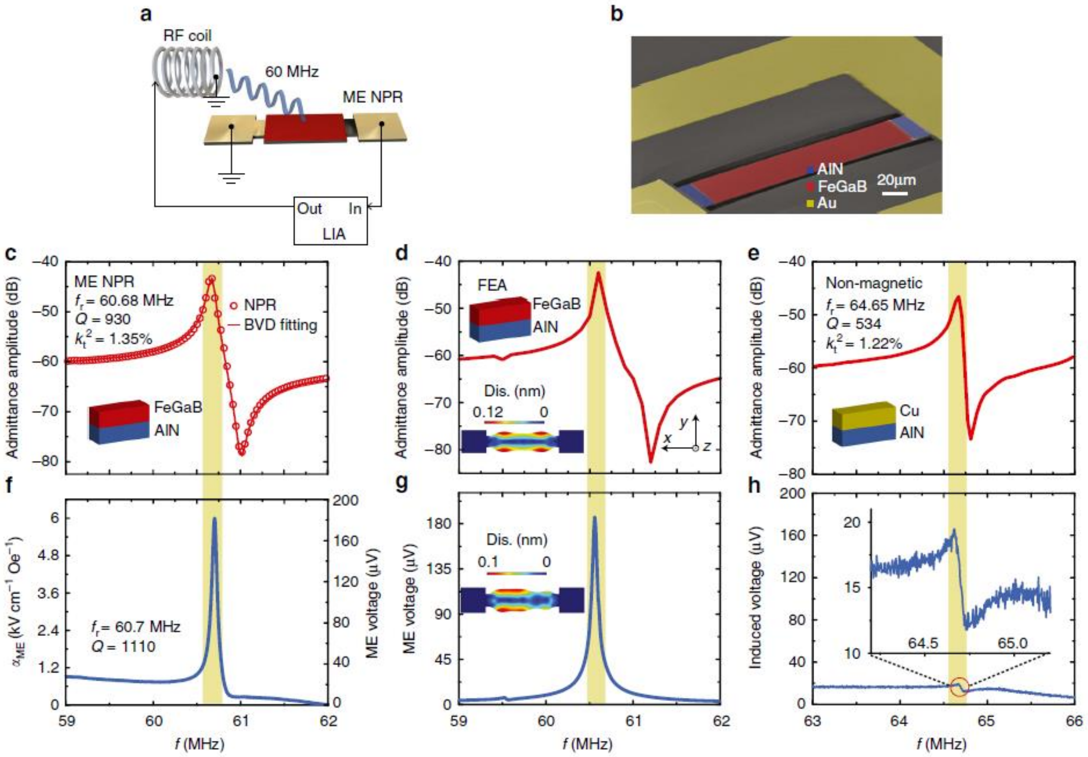

Fig. 3.1. Comparisons between magnetostrictive and non-magnetic NPR. Reproduced from [65].

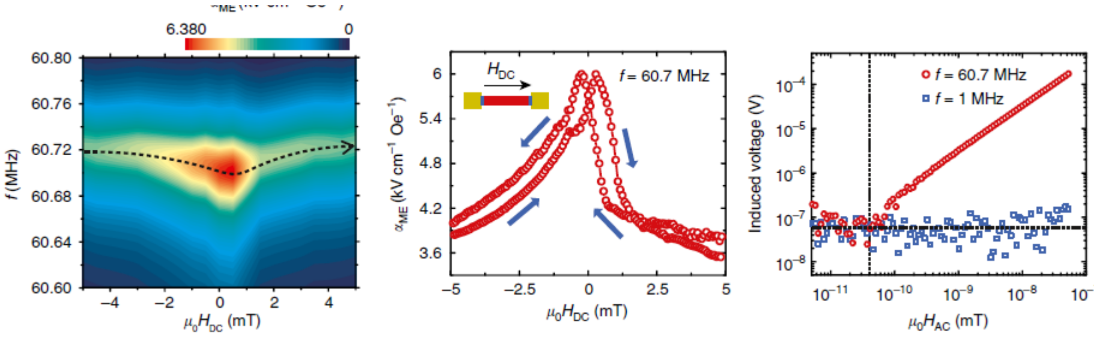

Fig. 3.2. Magnetoelectric (ME) coupling coefficient of NPR under various bias magnetic fields. Reproduced from [65].

voltage output at the electromechanical resonance frequency. The signal is then amplified using a UHF lock-in amplifier. While both magnetostrictive and non-magnetic structures exhibit similar resonance frequency behavior, their receiving voltage differs significantly, confirming that FeGaB effectively enhances signal detection through magnetoelectric coupling.

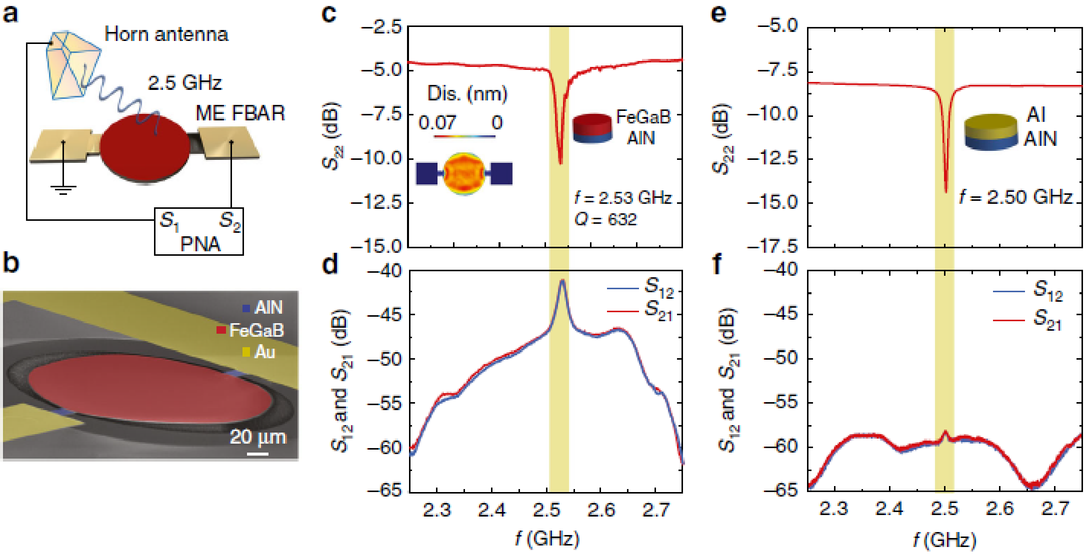

Fig. 3.3. ME antenna of magnetostrictive and non-magnetic control samples. Reproduced from [65].

Notably, this test was conducted without any DC bias magnetic field, indicating that the radiation enhancement is independent of ferromagnetic resonance. Additionally, they examined the NPR under a bias magnetic field ranging from -5 to 5 mT, as shown in Fig. 3.2. The observed variations in receiving voltage are attributed to the delta-E effect, a phenomenon further explored in Chapter 3.3. The delta-E effect occurs when changes in the bias magnetic field alter the Young’s modulus of the magnetostrictive layer, thereby shifting the resonance frequency of the resonator. Consequently, the peak of the ME coupling coefficient also shifts, with its maximum occurring at zero bias field. They explain this behavior using an edge curling wall effect, proposing a so-called self-bias condition. Building upon these receiving test results, the study extended its investigation into high-frequency magnetoelectric antennas.

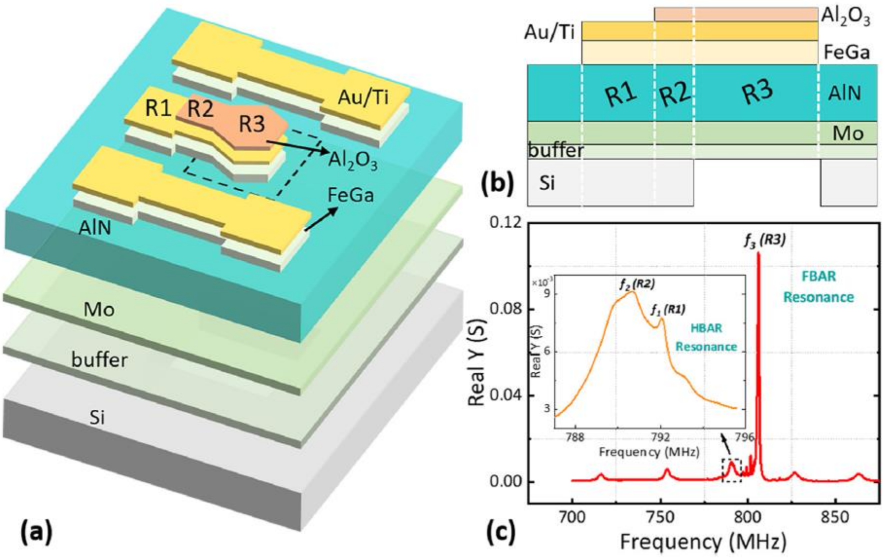

Fig. 3.4. Stackings of ME antenna for bandwidth enhancement. Reproduced from [66].

The 2.53 GHz ME antenna is also based on a FeGaB/AlN structure, while the non-magnetic counterpart utilizes Cu/AlN, as shown in Fig. 3.3. The effect of ME coupling was validated by comparing the $|S_{21}|$ transmission coefficients of the FeGaB/AlN structure to those of the non-magnetic Cu/AlN sample. However, several critical aspects remain unaddressed in their tests. First, they did not conduct bias magnetic field tests for the 2.53 GHz antenna. Given that magnetic properties vary significantly from the MHz to GHz range, it is essential to test and distinguish different effects at higher frequencies. Additionally, their comparison was based on non-magnetic samples, despite the assumption that radiation is driven by the magnetostrictive effect. A more appropriate comparison would be between magnetostrictive and non-magnetostrictive samples rather than between magnetostrictive and non-magnetic ones. This approach would provide more direct evidence to confirm the fundamental mechanism behind multiferroic or magnetoelectric antennas. Lastly, none of the experimental setups are shown in this work.

All subsequent experimental studies have built upon this work, with no additional tests conducted, aside from my own research, which represents a key contribution. Nonetheless, I will summarize several further tests performed in other magnetoelectric antenna studies at around UHF and SHF bands.

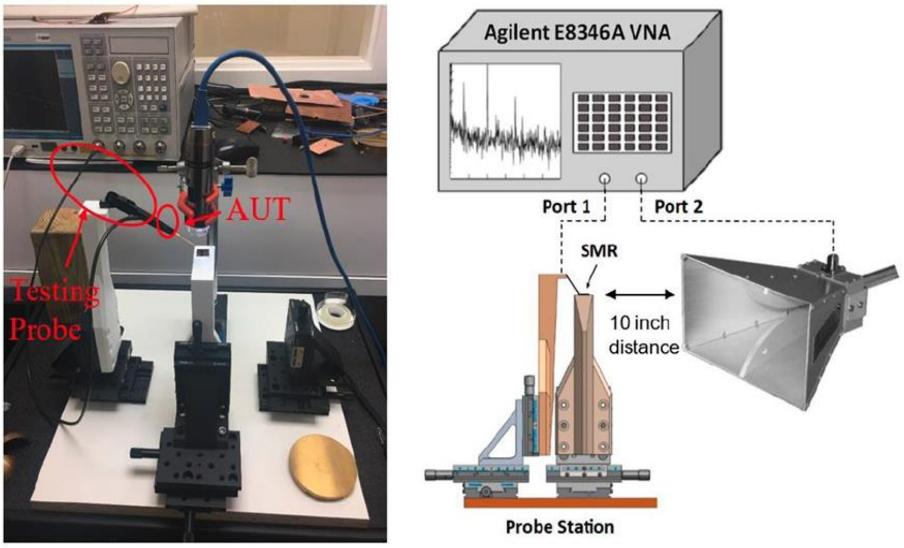

Fig. 3.5. Measurement setup for SMR ME antenna. Reproduced from [67].

In a subsequent study by Yun et al. in 2022 [66], a method for bandwidth enhancement was proposed. They achieved this by arranging resonators in parallel with different stack configurations, as shown in Fig. 3.4. Due to variations in thickness, the three regions (R1, R2, and R3) exhibited distinct yet closely spaced resonance frequencies. The approach was validated through measurements using a horn antenna and a network analyzer, followed by additional testing with a signal generator and a spectrum analyzer. However, this study did not include further validation of the underlying mechanisms. Following the initial work by Nan et al., Prof. Nian X. Sun's team continued exploring the design of solid-mounted resonators (SMR) and antenna arrays for ME antennas [67], [68].

SMR technology is widely used in BAW resonator designs, employing a Bragg reflector to replicate the boundary conditions of air cavities. The advantages of SMR include improved power handling due to enhanced heat dissipation and a more

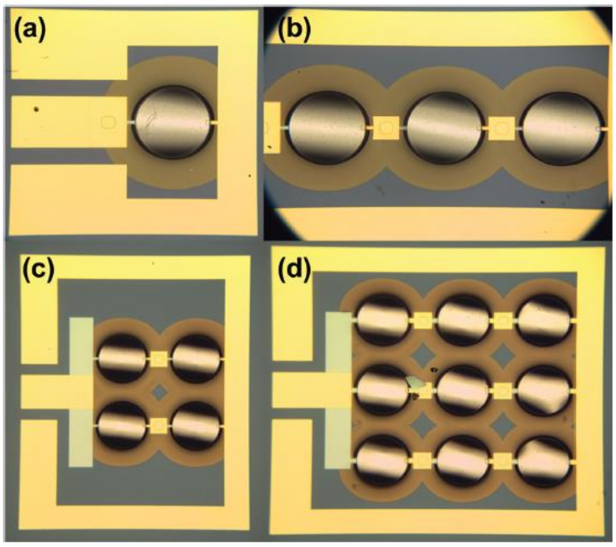

Fig. 3.6. ME antenna array. Reproduced from [68].

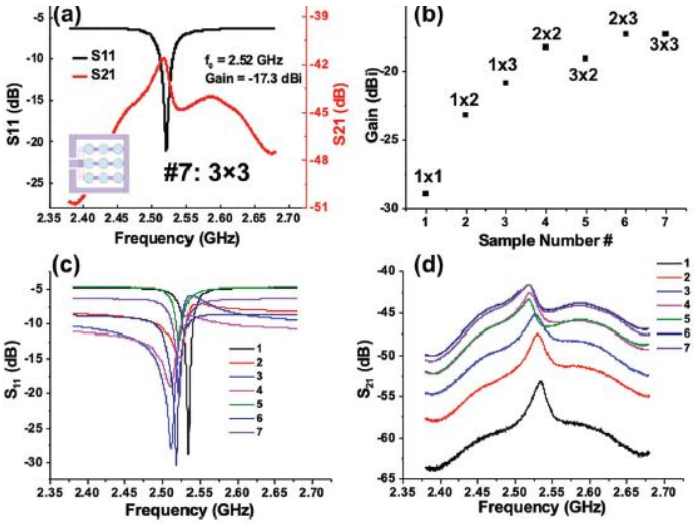

Fig. 3.7. ME antenna array measurement results. Reproduced from [68].

mechanically robust structure. In this study, the full measurement setup was finally presented in the supplementary information, as shown in Fig. 3.5. A custom-made plastic probe station was used to minimize electromagnetic interference. However, no additional validation was provided to further explain the underlying mechanisms of the device.

Another study extended ME antennas into an array configuration, as illustrated in Fig. 3.6, with the corresponding results shown in Fig. 3.7. However, for optimal

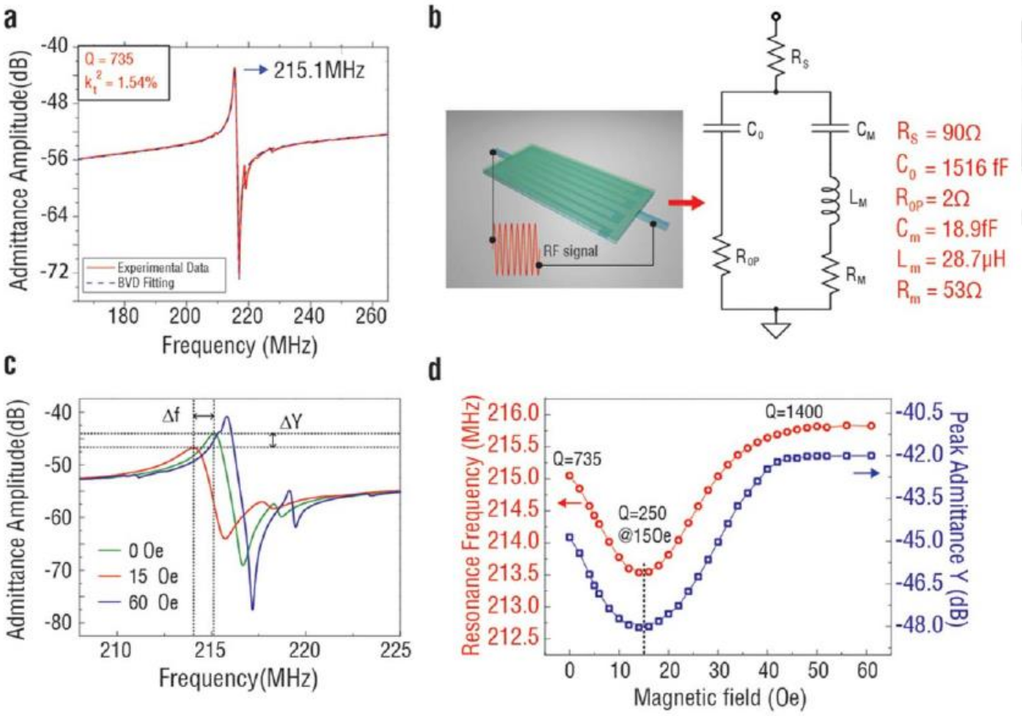

Fig. 3.8. ME sensor and measurement results. Reproduced from [70].

electromagnetic wave performance, the antenna array spacing should be designed in relation to free-space wavelengths. This study did not specify the array spacing, raising concerns about its impact on performance. Theoretically, if the spacing is too small, the array functions as a continuous structure rather than a discrete antenna array, limiting its ability to enhance gain significantly. As a result, the findings in Fig. 3.7 remain questionable regarding the claimed benefits of the array design.

The highest-frequency ME antenna design to date has been developed for 5G applications [69]. This study also utilizes an SMR design targeting 4.97 GHz operation. However, the validation approach remains the same, comparing a non-magnetic structure (Al/W/AlN) with a magnetostrictive one (FeGaB/SiO_2/AlN). Aside from the shift to a higher frequency band, the work does not introduce any new mechanisms nor insights.

3.2 Magnetic Sensors

Before the development of magnetoelectric (ME) antennas, research within the community primarily focused on magnetic sensors, particularly magnetoelectric sensors utilizing the delta-E effect. This phenomenon appears to be closely related to the results observed during our DC magnetic field response experiments. Fundamentally, the response of the device to the magnetic field is governed by the same structural configuration, and the variation of the reflection coefficient with respect to the magnetic field is examined. Nonetheless, whether the magnetoelectric (ME) antenna primarily functions as an antenna or as a sensor—and the underlying mechanisms that differentiate these roles—remains an open question. As such, this section will also briefly discuss relevant works concerning magnetic field sensors. I will summarize two key papers that represent significant contributions to magnetic sensor technology [70], [71].

The first study, conducted prior to the ME antenna work in [65], demonstrated a 215 MHz nano-plate resonator with a DC magnetic field detection limit of approximately 300 picoTesla. The admittance curve was measured using an RF probe connected to a network analyzer, as shown in Fig. 3.8. The device monitors changes in DC bias magnetic field by detecting shifts in resonance frequency. For instance, the resonance frequency varied as the magnetic field changed from 0 Oe to 15 Oe and then to 60 Oe. Continuous magnetic field sweeps are recorded in Fig. 3.8(d).

For sensitivity and linearity measurements, the ME sensor was placed under a fixed 5 Oe DC bias magnetic field while small variations in the magnetic field were introduced. As shown in Fig. 3.9, the sensor exhibited good linearity in the range of 50 picoTesla to 4 nanoTesla. However, measurement values for the admittance amplitude began to diverge below 300 picoTesla, indicating a sensitivity limit at this level.

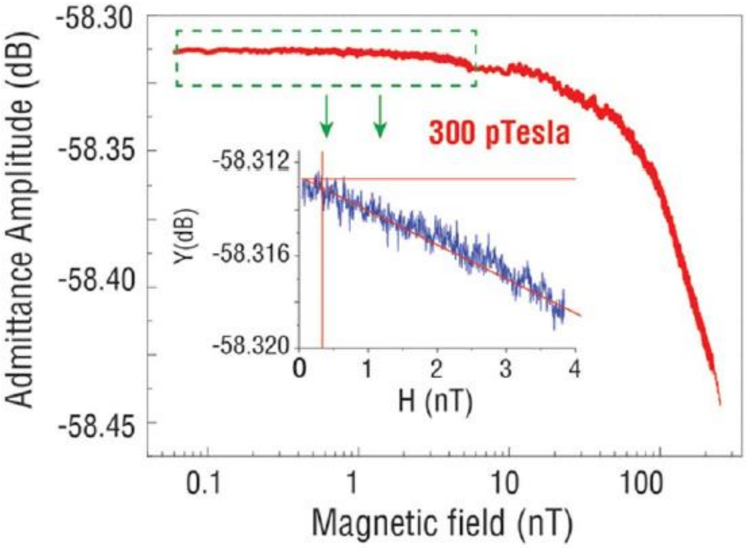

Fig. 3.9. ME sensor and sensitivity measurement. Reproduced from [70].

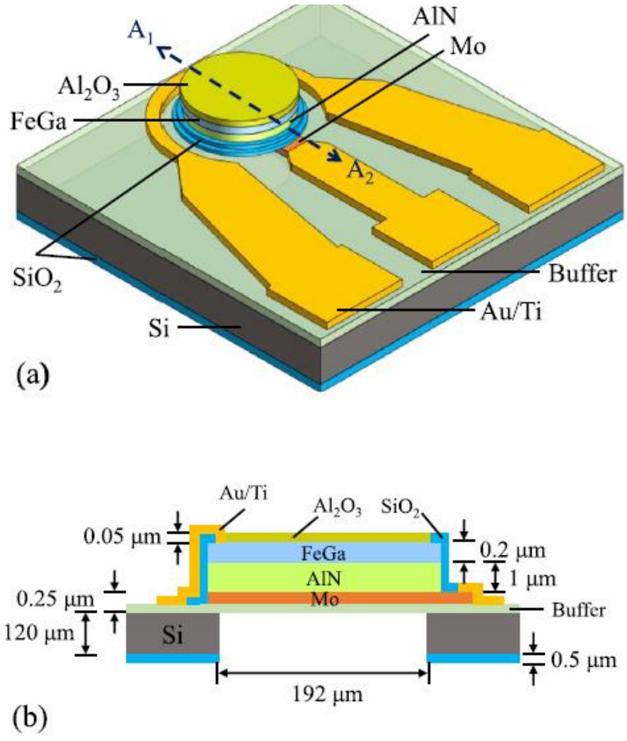

Fig. 3.10. Schematic graph of biaxial magnetic field sensors. Reproduced from [71].

A more recent study also utilized the delta-E effect. In this work, the magnetic sensor

doi:10.6342/NTU202501094

exhibited a resonant frequency shift of 1.03 MHz under a 567 Oe in-plane magnetic field and 0.2 MHz under a 720 Oe out-of-plane magnetic field, with corresponding S11 variations of 30.2 dB and 0.92 dB, respectively, as shown in Fig. 3.10 and Fig. 3.11 [71]. However, it is important to note that the observed frequency shift is relatively small. Specifically, the center frequency of approximately 2.47 GHz shifted by only 1.03 MHz when the magnetic field increased from 0 Oe to 630 Oe, corresponding to just a 4% fractional bandwidth.

In [72], the authors examined the frequency dependence of the delta-E effect and found that its magnitude either continuously decreases with increasing frequency or peaks just below the ferromagnetic resonance (FMR) frequency, depending on the damping factors. Therefore, when monitoring such small frequency shifts, careful consideration is necessary.

doi:10.6342/NTU202501094

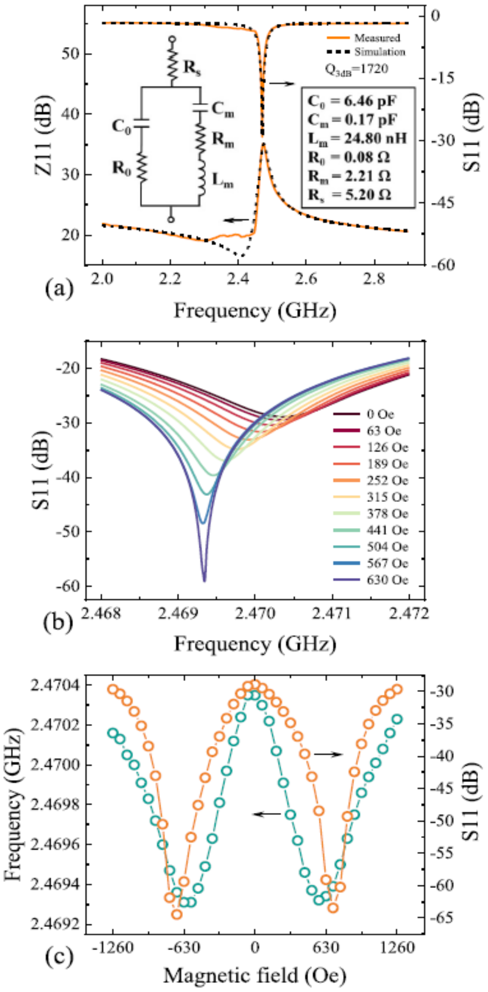

Fig. 3.11. Schematic graph of biaxial magnetic field sensors. Reproduced from [71].

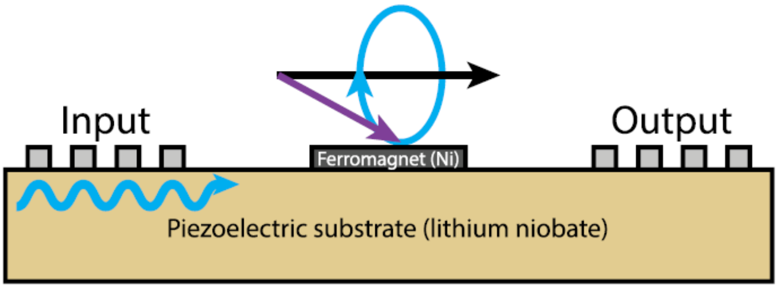

Fig. 3.12. Schematic of ADFMR experiment. Reproduced from [73].

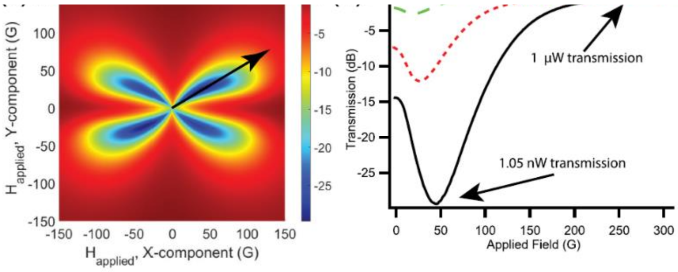

Fig. 3.13. Power absorption behavior for ADFMR. Reproduced from [73].

3.3 Acoustically Driven Ferromagnetic Resonances

A well-documented experimental phenomenon closely linked to multiferroic antennas is acoustically driven ferromagnetic resonance (ADFMR). This effect is investigated using surface acoustic waves (SAWs) as the driving mechanism. The setup consists of interdigitated transducers (IDTs) fabricated on a piezoelectric substrate, with a magnetostrictive ferromagnetic layer placed between them. When an alternating

doi:10.6342/NTU202501094

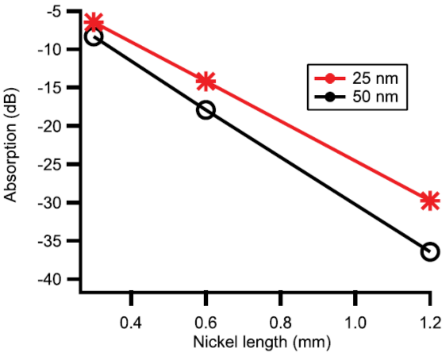

Fig. 3.14. Power absorption behavior for ADFMR compared to the device length and thickness. Reproduced from [73].

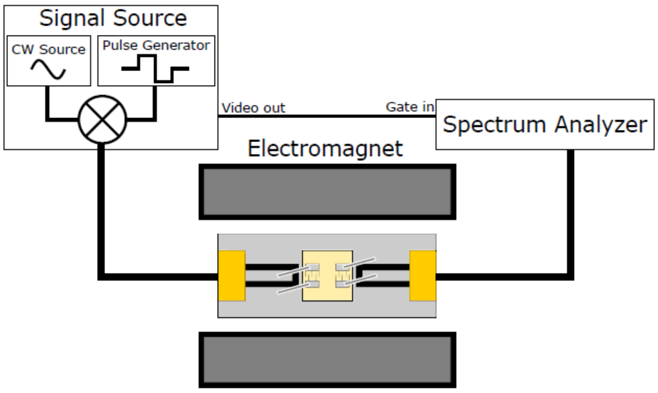

Fig. 3.15. Schematic of experimental measurement setup. Reproduced from [74].

voltage—typically in the gigahertz range—is applied to one of the IDTs, it generates a coherent elastic wave that propagates along the piezoelectric surface. This SAW interacts with the ferromagnetic layer through magnetoelastic coupling, effectively supplying an RF excitation field that triggers ferromagnetic resonance (FMR), as illustrated in Fig. 3.12 [73]. When the SAW frequency aligns with the magnet's intrinsic FMR frequency, energy is efficiently transferred via magnetoelastic interactions, resulting in resonance. By measuring the power transfer function $|S_{21}|^2$ between the input and output terminals, the magnitude of this interaction can be quantified.

Experimental observations reveal that power absorption depends on the angle relative to the SAW propagation direction, as depicted in Fig. 3.13(a). The highest

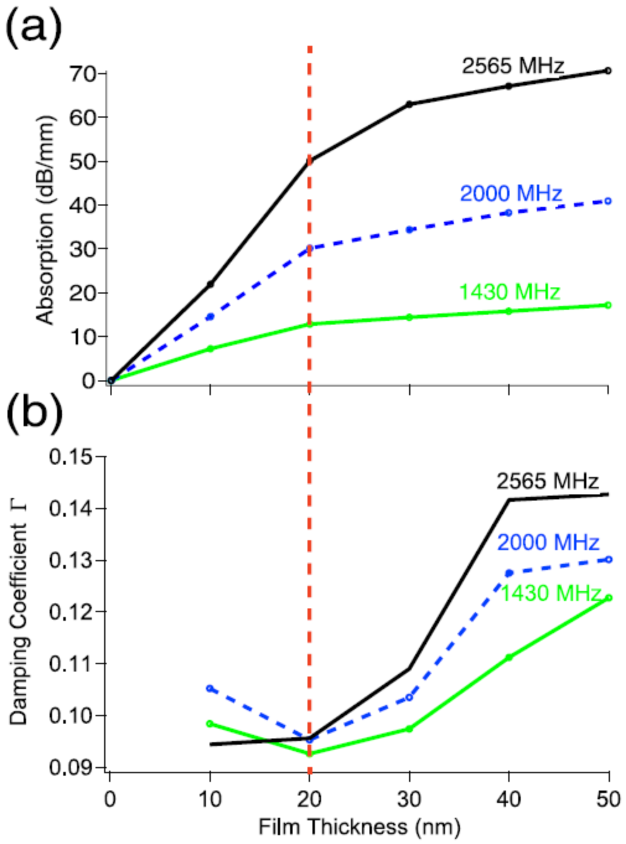

Fig. 3.16. Relation between Nickel film thickness and absorption. Reproduced from [74].

absorption occurs around 40°. This optimal angle is then used to examine the relationship between applied magnetic field and power absorption at three distinct frequencies (857 MHz, 1424 MHz, and 1992 MHz, from top to bottom), as shown in Fig. 3.13(b). The results confirm that power absorption increases with frequency, consistent with standard ferromagnetic resonance behavior. Further analysis, shown in Fig. 3.14, investigates how absorption varies with the length and thickness of the Nickel layer. Thicker films exhibit faster attenuation as length increases, and each thickness follows an exponential decay pattern in power absorption as length extends.

In summary, ADFMR presents a highly effective approach for antenna applications, as SAW devices achieve efficiency levels above 90%, while FMR reaches efficiencies

doi:10.6342/NTU202501094

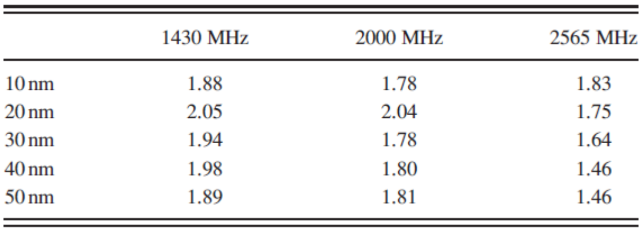

	1430 MHz	2000 MHz	2565 MHz
10 nm	1.88	1.78	1.83
20 nm	2.05	2.04	1.75
30 nm	1.94	1.78	1.64
40 nm	1.98	1.80	1.46
50 nm	1.89	1.81	1.46

Fig. 3.17. Relation between Nickel film thickness and magnetoelastic coefficients (MJ/m^3). Reproduced from [74].

exceeding 99.9%.

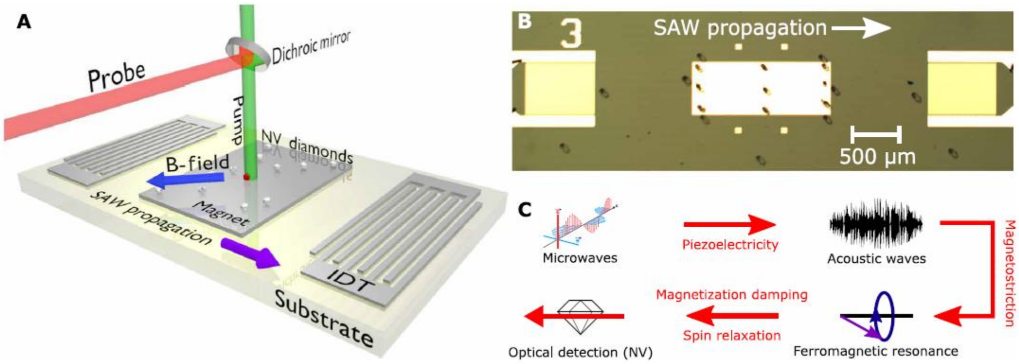

Fig. 3.18. Experimental setup and mechanism of combining ADFMR with NV diamonds. Reproduced from [75].

Again, it uses similar experimental setups as previous work, which is shown in Fig. 3.15 [75]. This work following previous one focuses on more film thickness variation analysis, which is shown in Fig. 3.16. Similarly, the maximums of the relative angle of power absorption are selected and plotted against the film thickness. The frequency corresponds to 1430 MHz (green), 2000 MHz (blue) and 2565 MHz (black). It is found that the damping parameter increases as a function of thickness of the Ni film beyond 20 nm and then saturate when it becomes thicker. Yet, the magnetoelastic coefficient is shown to be independent of excitation frequency and film thickness, as shown in Fig. 3.16.

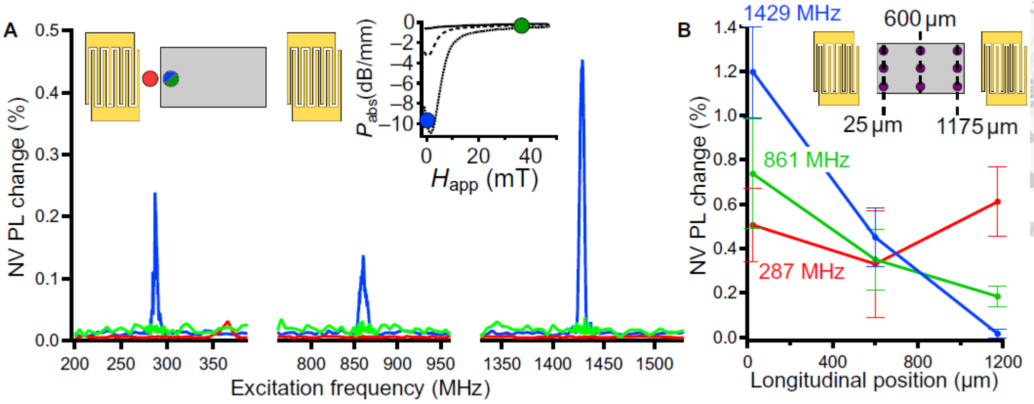

Fig. 3.19. The correlation between NV PL change and ADFMR power absorption. Reproduced from [75].

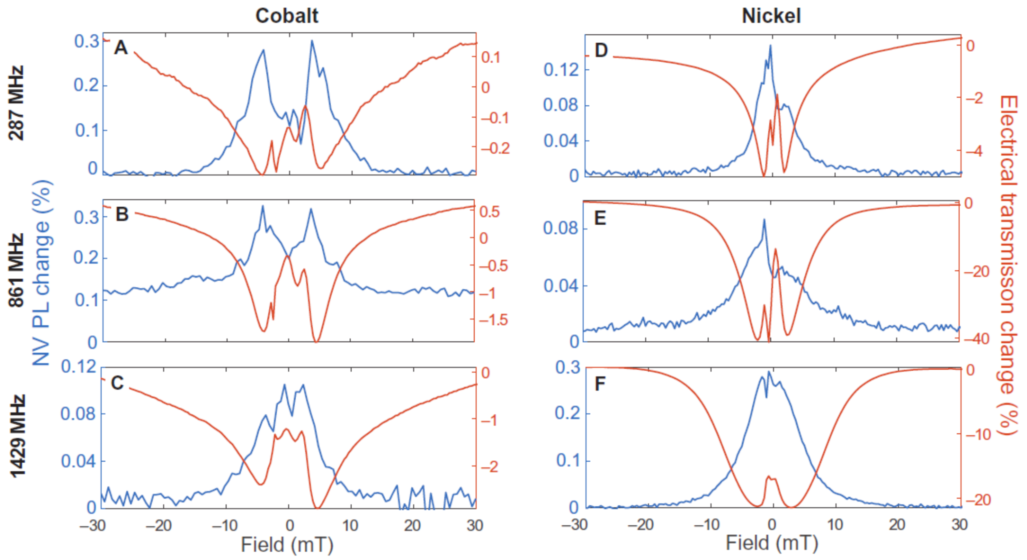

Fig. 3.20. Correlation between power absorption and NV PL change with different frequencies and bias magnetic fields for Cobalt and Nickel. Reproduced from [75].

This study expands on previous work by integrating optical detection of acoustically driven ferromagnetic resonance (ADFMR) through the use of nitrogen-vacancy (NV) centers in nanodiamonds. The experimental setup, illustrated in Fig. 3.18, consists of an ADFMR device where microfabricated resonant interdigitated transducers (IDTs) generate surface acoustic waves (SAWs) on a piezoelectric lithium niobate ($LiNbO_3$) substrate when driven by a microwave signal. A 20 nm-thick ferromagnetic layer, composed of either cobalt or nickel, is placed atop the substrate. Nanodiamonds

doi:10.6342/NTU202501094

containing NV centers are then dispersed across multiple locations on the ferromagnetic film, enabling spatially resolved optical detection of the ADFMR effect. These NV-doped regions appear as dark circular spots in the optical image.

By analyzing photoluminescence (PL) modulation, a direct correlation between ADFMR power absorption and the percentage change in NV PL intensity can be established. As depicted in Fig. 3.19(a), the peak NV PL change precisely coincides with the frequency at which ADFMR power absorption is maximized, demonstrating a direct optical recording of the resonance phenomenon. Additionally, Fig. 3.19(b) illustrates how the power attenuates as the SAW propagates toward the second port, with a corresponding decrease in NV PL change. This further confirms the direct relationship between ADFMR and NV PL response.

A comprehensive comparison of power absorption and NV PL change for both nickel and cobalt across various frequencies and applied magnetic field strengths is presented in Fig. 3.20. The results indicate that cobalt exhibits stronger coupling between ADFMR and NV centers than nickel. Despite nickel displaying higher ADFMR power absorption, the resulting NV PL change remains comparable to that of cobalt, highlighting differences in coupling efficiency between the two materials.

doi:10.6342/NTU202501094

Chapter 4 Multiferroic Antenna Validation by Composite Comparisons

In this chapter, the polarization control design based on lateral electrode excitation for the whole device is simulated, fabricated and measured. It will be shown that Nickel, a magnetoelastic material, consistently demonstrates magnetically induced radiation at both resonance frequencies. However, Permalloy ($Ni_{78}Fe_{22}$), which has significantly weaker magnetoelastic effects, exhibits similar transmission behavior at 3.67 GHz and enhanced power absorption at 6.42 GHz. Our findings suggest that the dynamic response of magnetoelastic materials in the GHz range differs from their behavior at MHz and lower frequencies. This evidence highlights the need for further investigation into the underlying mechanisms of magnetoelectric radiation.

4.1 Multiferroic Antenna Based on Lateral Electrodes Excitation

Polarization plays a vital role in antenna design, and circularly polarized antennas have been extensively studied due to their numerous benefits, including enhanced signal integrity, increased channel capacity in communication systems, and simplified installation. Traditional excitation methods primarily rely on the thickness-extensional mode using $d33$ excitation. However, achieving polarization control requires the introduction of additional excitations with specific phase differences.

In recent years, film bulk acoustic resonators (FBARs) have gained significant attention, especially in high-frequency filtering and sensing applications, where they

doi:10.6342/NTU202501094

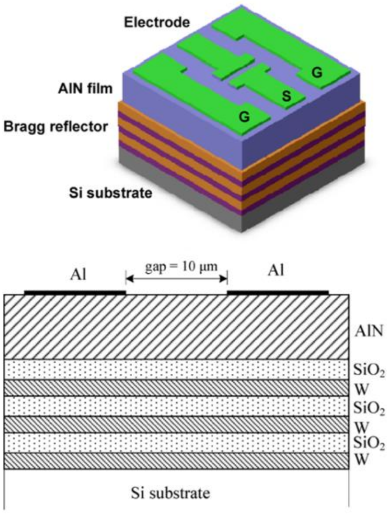

Fig. 4.1. The schematic of the AlN-based solidly mounted resonator operating in thickness-shear mode waves. Reproduced from [77].

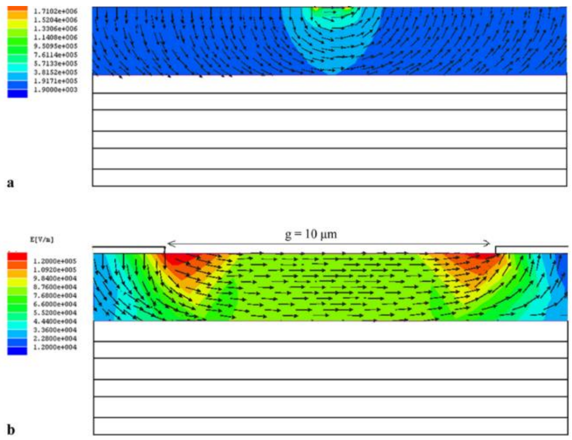

Fig. 4.2. The electric field distribution generated by electrode geometries with gap sizes of 1 μm and 10 μm. Reproduced from [77].

typically operate in the longitudinal mode. For liquid-based mass-loading sensors, thickness-shear modes (TSM) offer a higher quality factor compared to longitudinal modes. Consequently, research into TSM behavior in FBARs has been increasing, as illustrated in Fig. 4.1 and Fig. 4.2 [76], [77].

TSM waves propagate along the thickness direction of piezoelectric films but feature

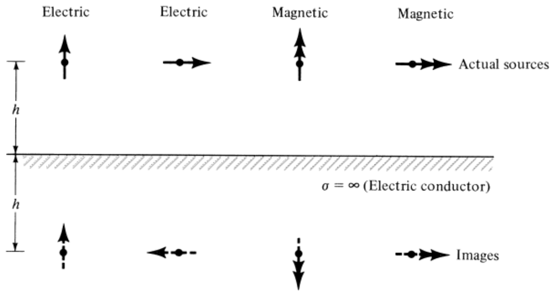

(a) Electric conductor

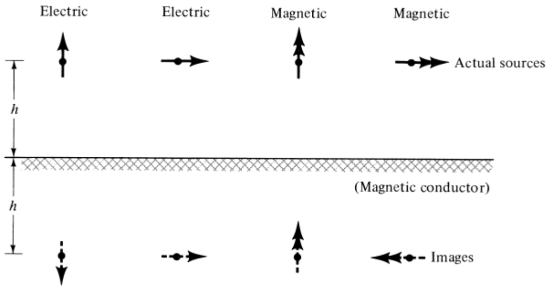

(b) Magnetic conductor

Fig. 4.3. Electric and magnetic sources and their image currents. Reproduced from [78].

particle displacement parallel to the film surface. This unique property allows TSM waves to support two orthogonal in-plane modes, making them an excellent candidate for generating circular polarization.

Additionally, because shear mode excitation occurs within an in-plane structure, it can enhance radiation instead of suppressing it when placed above a conductive surface. This is due to the unidirectional image magnetic current, as depicted in Fig. 4.3, making it more advantageous than the traditionally used longitudinal mode.

Various techniques exist for exciting TSM waves, including interdigitated electrodes (IDE) and lateral electrodes, both of which have been explored in previous studies. Among these, lateral excitation is often preferred due to its simpler implementation [78].

By leveraging lateral field excitation in bulk acoustic wave (BAW)-based multiferroic antennas, polarization states can be dynamically tuned by adjusting the control voltage.

In order to demonstrate the polarization control based on lateral electrode excitation, the modeled design of the BAW-based multiferroic antenna is illustrated in Fig. 4.4 and Fig. 4.5. It comprises three distinct material layers: a piezoelectric layer, a magnetostrictive layer, and an acoustic buffer. The piezoelectric component converts an applied AC voltage into mechanical stress waves, which then interact with the magnetostrictive material, inducing oscillatory magnetization and ultimately generating electromagnetic radiation.

In this configuration, stress fields are created using lateral electrodes. As depicted in Fig. 4.4, instead of placing electrodes on both the top and bottom surfaces, two sets of electrodes are positioned at the bottom of the structure. By applying AC voltages with a 90-degree phase difference to these electrode sets, a circularly polarized shear wave is produced, propagating along the z-axis. This wave drives circularly polarized magnetization in the magnetostrictive layer, leading to the formation of a circularly polarized magnetic current—the key source of the antenna’s circularly polarized radiation.

doi:10.6342/NTU202501094

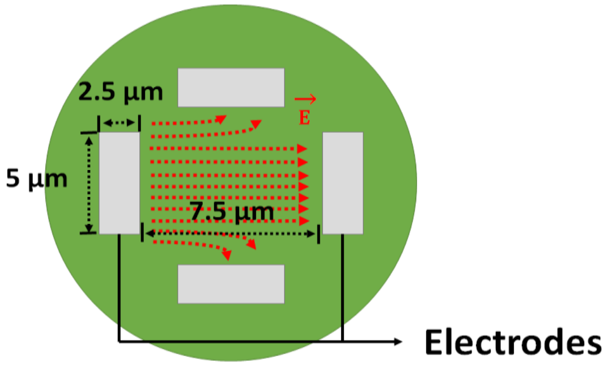

Fig. 4.4. External voltage sources with a 90-degree phase difference are applied to electrodes, generating a circularly polarized electric field at the bottom. Reproduced from [79].

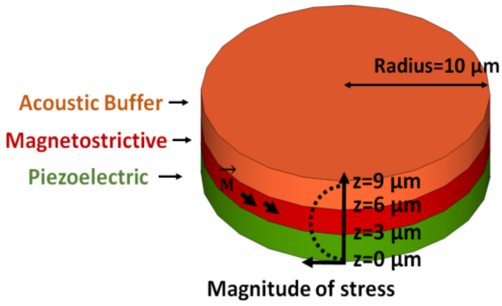

Fig. 4.5. The simulated structure of the BAW-mediated multiferroic antenna. Reproduced from [79].

Based on the analysis in [77], the presence of the TSM wave induced by lateral field excitation can be confirmed by deriving the Christoffel equation. The acoustic velocity of the thickness shear mode is given by:

$$v_s = \sqrt{\frac{c_{44} + e_{15}^2/\varepsilon_{11}}{\rho}} \tag{4.1}$$

In this context, $c44$ represents a stiffness tensor component, $e15$ corresponds to a piezoelectric coupling tensor component, $\varepsilon 11$ denotes a permittivity tensor component, and ρ signifies the material's volume density. The calculated wave velocity is

doi:10.6342/NTU202501094

approximately 6333 m/s. For a fundamental mode resonance at 2.5 GHz, the required thickness of the piezoelectric layer is around 1 μm.

Additionally, when a thickness-shear mode (TSM) wave propagates along the third axis, the stress component Txz is directly generated through excitation along the first axis, while Tyz arises from excitation along the second axis. By introducing a 90-degree phase shift between Txz and Tyz, the two orthogonal TSM waves combine to create a circularly polarized shear stress field. Since both the nickel layer and the buffer material exhibit isotropic properties, this shear wave forms a standing sinusoidal wave pattern along the z-axis.

COMSOL is a finite-element based solver that provides streamlined workflows for simulating multiphysics phenomena. We use COMSOL to model acoustic-mechanical

doi:10.6342/NTU202501094

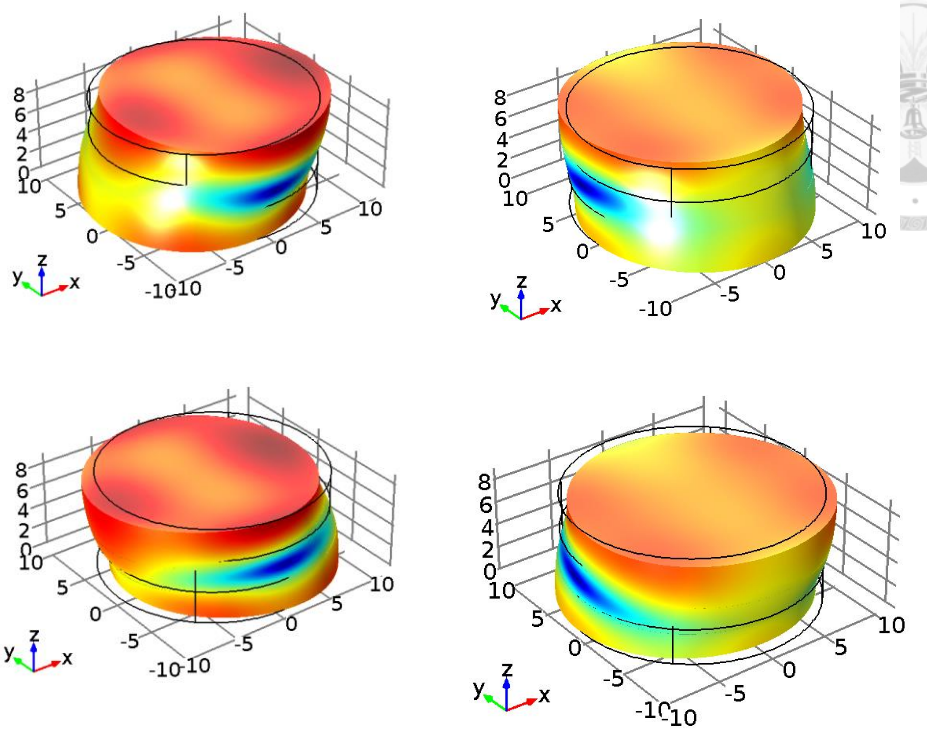

Fig. 4.6. Displacement animation at 250 MHz (with length units in μm) are shown. The frames correspond to different time instances: t=T/4 (Top-left), t=T/2 (Top-right), t=3T/4 (Bottom-left), and t=T (Bottom-right). A counterclockwise circularly polarized displacement, as viewed from the top, is clearly observed. Reproduced from [79].

resonance in a BAW-mediated multiferroic antenna, simultaneously calculating the coupling between stress and the electric field. By leveraging COMSOL, we first identify the eigenmodes of the TSM. Table 2 outlines the details of the simulation environment. Fig. 4.6 illustrates the circular motion of the BAW-mediated multiferroic device. As depicted in Fig. 4.6, the circular displacement induced by the bottom electrodes is most effective at a frequency of 250 MHz. Hence, lateral electrode excitation can not only enable radiation enhancement above conductive ground plane but also allow polarization control design for multiferroic antennas.

Table 2. Basic parameters of COMSOL simulation. Reproduced from [79].

Layer	**Materials**	**Study**	**Applied voltage**	**Boundary condition (others are free)**
Electrodes	Platinum	Electrostatics	Set 1: 1 (volt)、Set 2: 1i (volt)	N/A
Piezoelectric	Aluminum Nitride	Piezoelectric Effect	N/A	Top: form union Bottom: $u_z=0$
Magnetotrictive	Nickel	Solid mechanics	N/A	Top: form union Bottom: form union
Acoustic buffer	Silicon Nitride	Solid mechanics	N/A	Top: $u_z=0$ Bottom: form union

4.2 Device Simulation

The antenna utilizes a three-layer configuration, as illustrated in Fig. 4.7 and 4.8, which provide a schematic representation and a cross-sectional view, respectively. Additionally, a top-down microscope image is displayed in Fig. 4.9. To ensure optimal performance in high-frequency applications, aluminum nitride (AlN) is selected as the piezoelectric component due to its superior acoustic velocity, minimal material loss, and exceptional thermal conductivity. A thin 400 nm AlN film is applied to a silicon substrate and remains suspended over a precisely etched air cavity.

Beneath the AlN layer, two pairs of 50 nm-thick in-plane bilateral electrodes made of platinum (Pt) are positioned perpendicular to each other. This configuration allows for

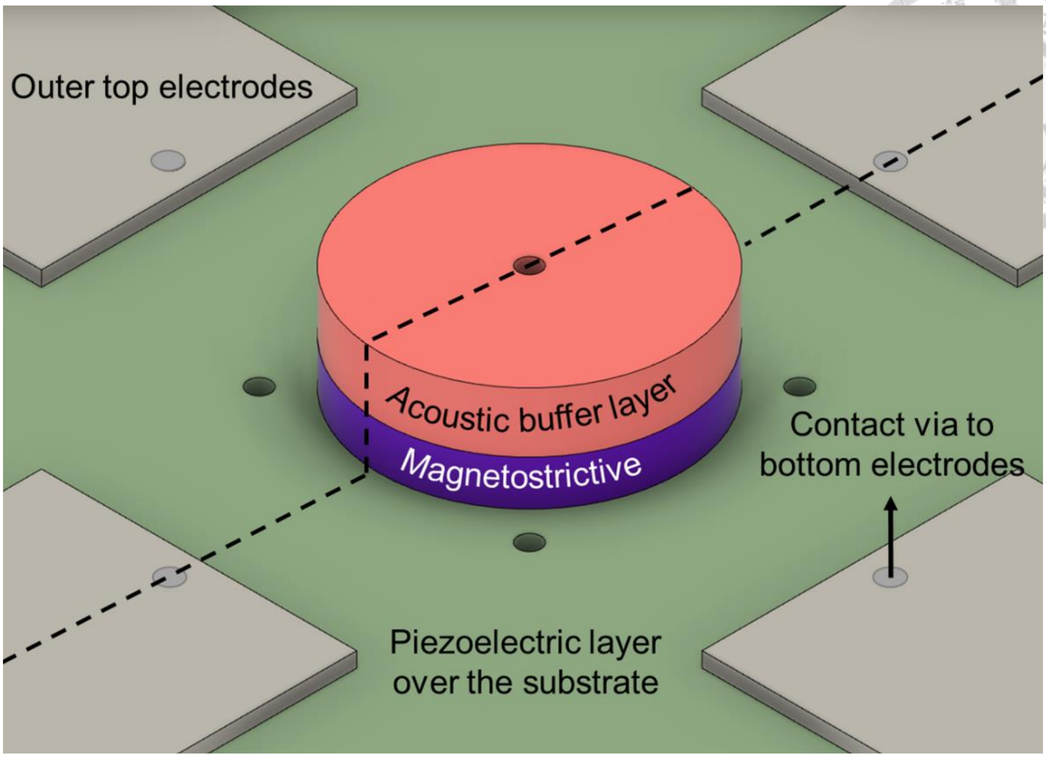

Fig. 4.7. Multiferroic antenna schematic graph. Reproduced from [80].

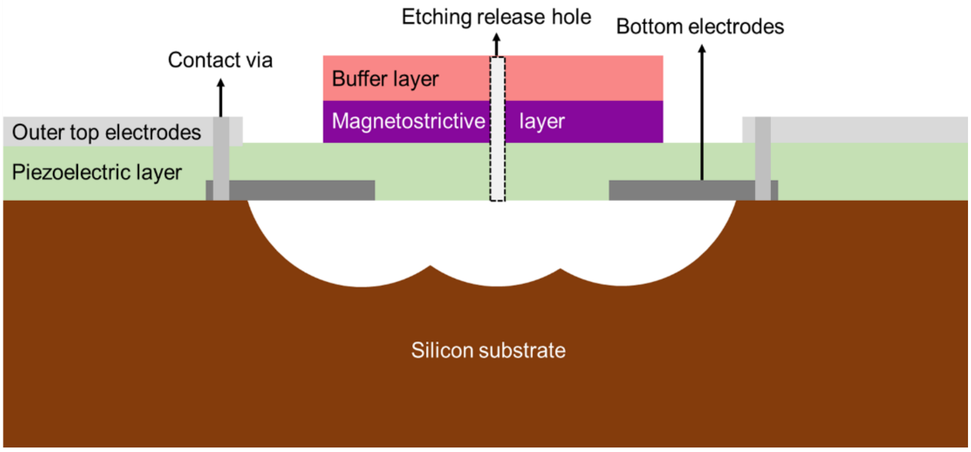

Fig. 4.8. Multiferroic antenna cross-sectional view. Reproduced from [80].

independent and symmetric excitation of the antenna, enabling polarization control. In all experiments presented, only one electrode pair is activated, while the other remains open. These in-plane bilateral electrodes excite thickness-shear modes and are connected to the outer electrodes via metallic vias. The applied input electric field induces dynamic stress, which is crucial for the subsequent coupling stage.

doi:10.6342/NTU202501094

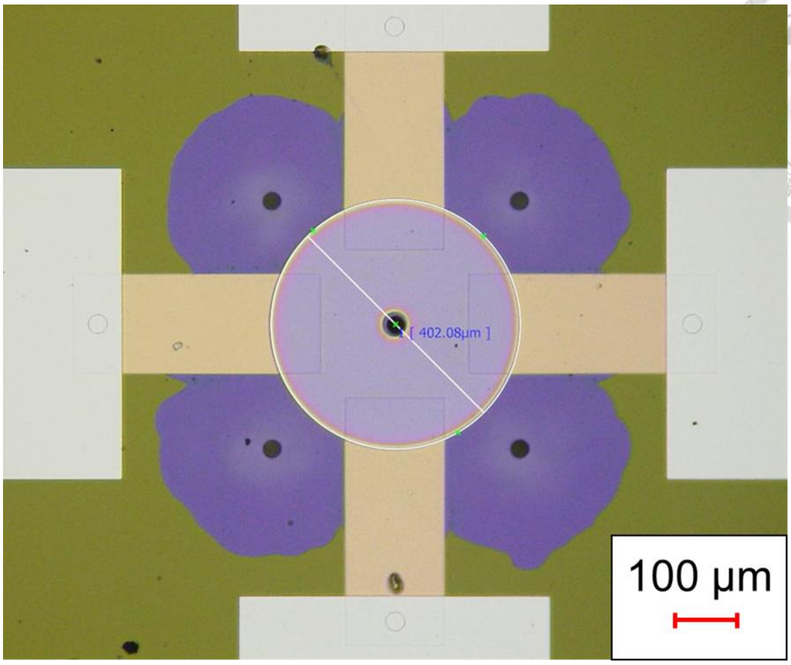

Fig. 4.9. Top-view optical microscope image of 200-μm-radius Ni test piece. Reproduced from [80].

Above the piezoelectric layer, a 300 nm-thick nickel (Ni) magnetostrictive layer is deposited in a disk shape with a 200 μm radius. This layer facilitates the coupling between dynamic stress and magnetization, serving as the expected source of electromagnetic radiation. A buffer layer of aluminum oxide (Al_2O_3) with the same disk geometry is then placed over the Ni layer to optimize the maximum amplitude within the Ni layer and provide oxidation protection.

The simulated structure for the fabricated device is shown in Fig. 4.10 and Fig. 4.11. Their difference is that Fig. 4.10 is rescaled in the thickness direction to show the layer composite structure better. The structure is based on FBAR design with 2 orthogonal sets of lateral Platinum electrodes for polarization control. The magnetostrictive layer Ni is sandwiched between piezoelectric layer AlN and acoustic buffer layer Al_2O_3. The etched cavity is made of half sphere structure below the AlN layer. The boundary conditions for

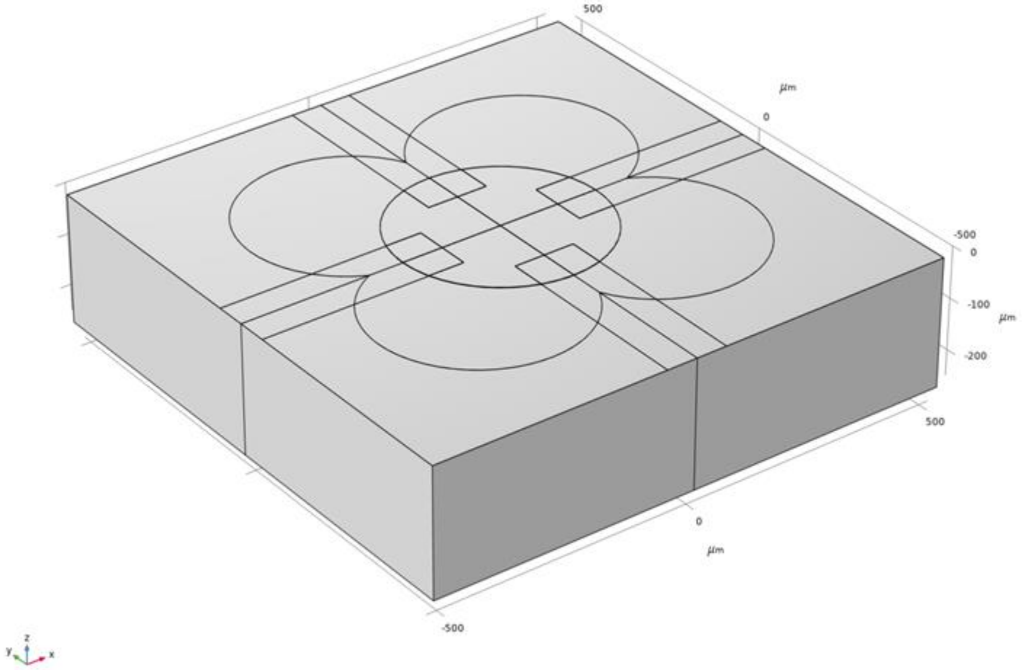

Fig. 4.10. The simulated structure of fabricated devices without rescaling.

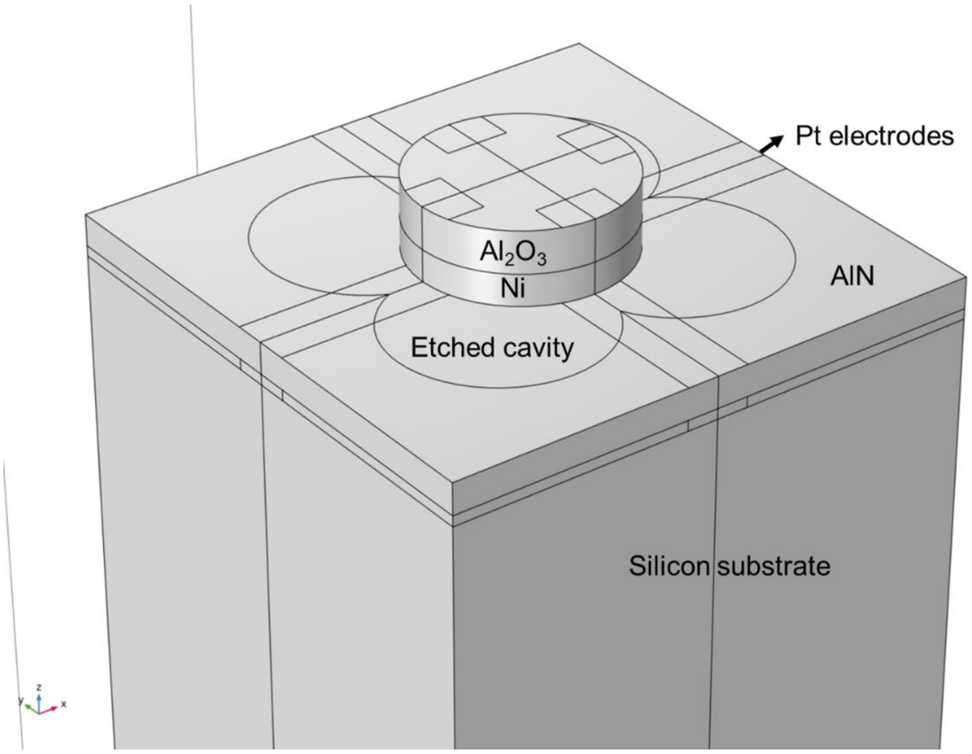

Fig. 4.11. The simulated structure of fabricated devices rescaled.

the full structures are shown in Fig. 4.12. One set of electrodes is connected to the signal

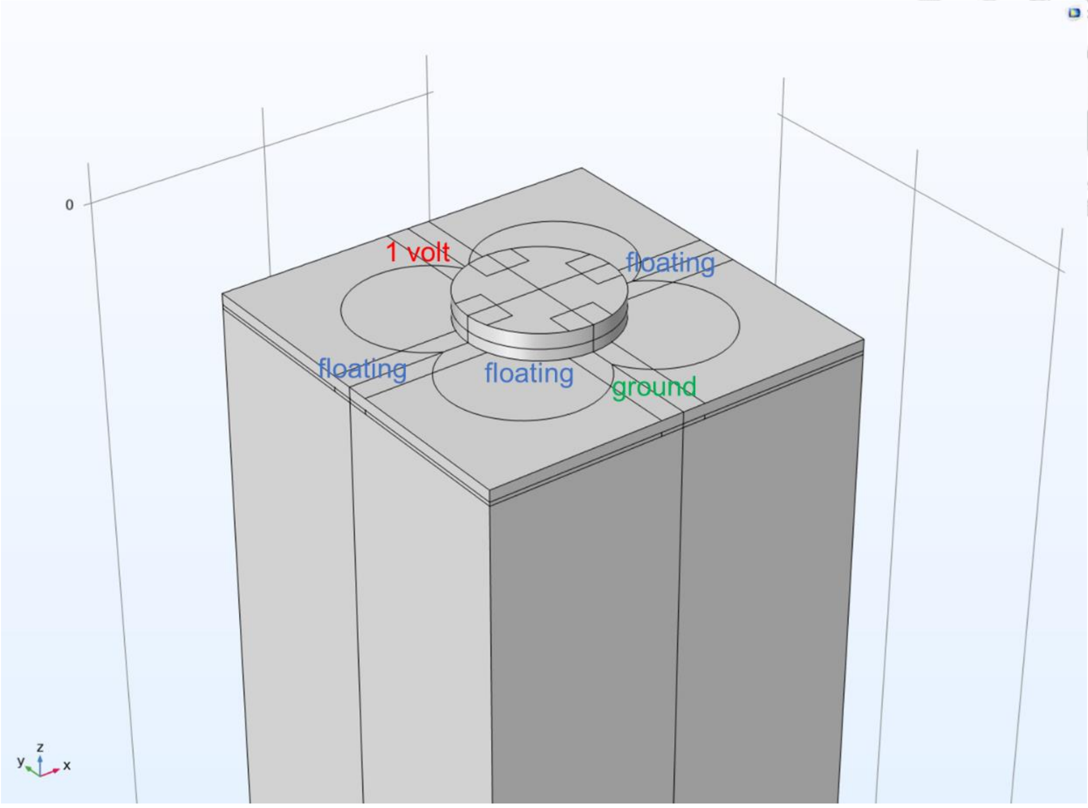

Fig. 4.12. Boundary conditions of simulated structure.

With floating potential condition applied, there are only *four modes(3.2/6.5/10.7/17.8)* below 20 GHz.

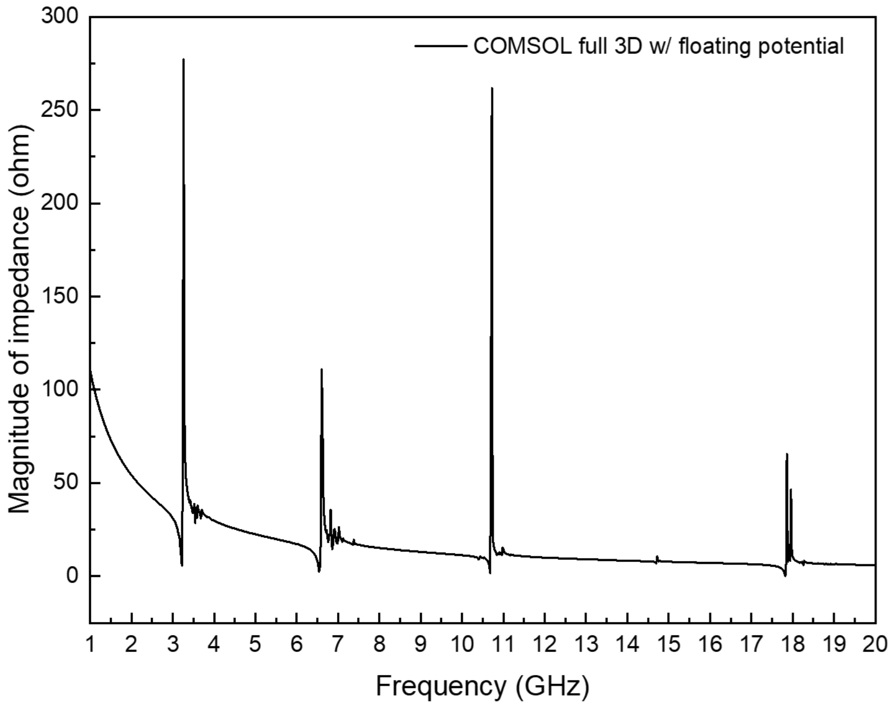

Fig. 4.13. Impedance response of the simulated structure with floating potential.

and ground. The other set of electrodes remains open and floating. In addition to the

Without floating potential condition, there are seven modes (2.3/4.4/6.6/7.7/9/11.2/20) below 20 GHz.

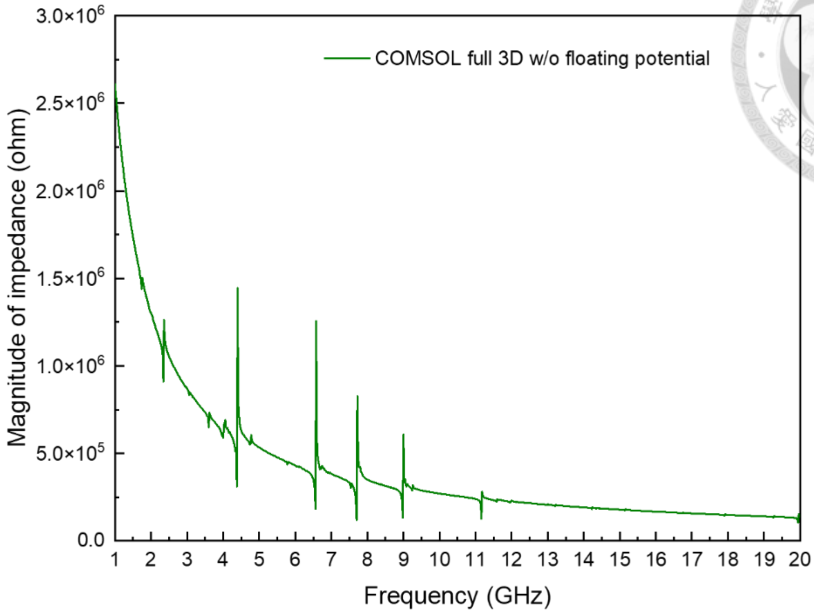

Fig. 4.14. Impedance response of the simulated structure without floating potential.

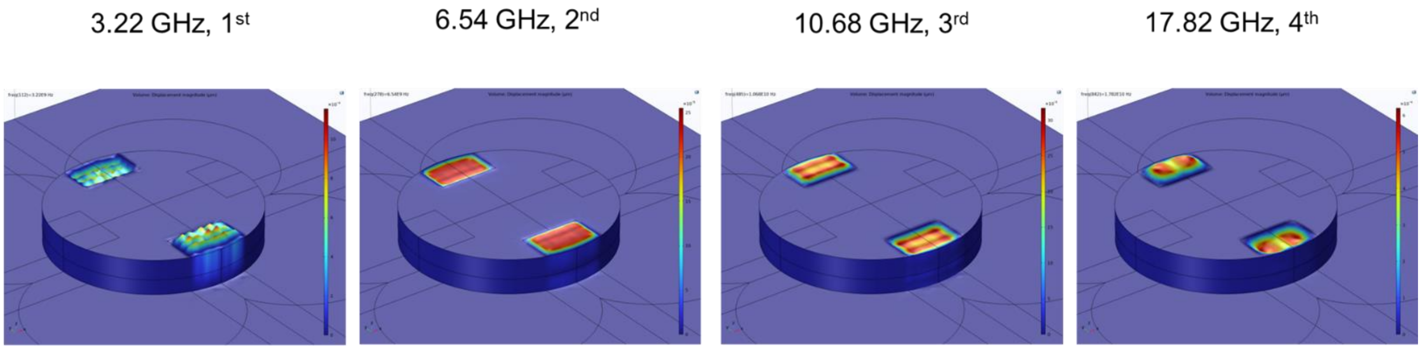

Below are same plots as top corresponding graphs but shown in half for better visualization

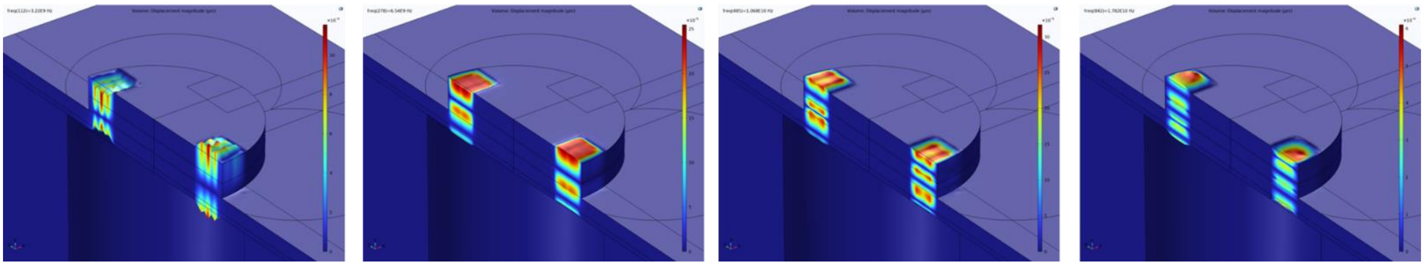

Fig. 4.15. Mode shape of the simulated structure without floating potential.

floating potential from the electrodes, since magnetostrictive layer Nikel is also metallic, it should also be considered as floating layer. The bottom surface will be attached to the PCB for the later measurement. It will be set as a fixed boundary condition. Except for

doi:10.6342/NTU202501094

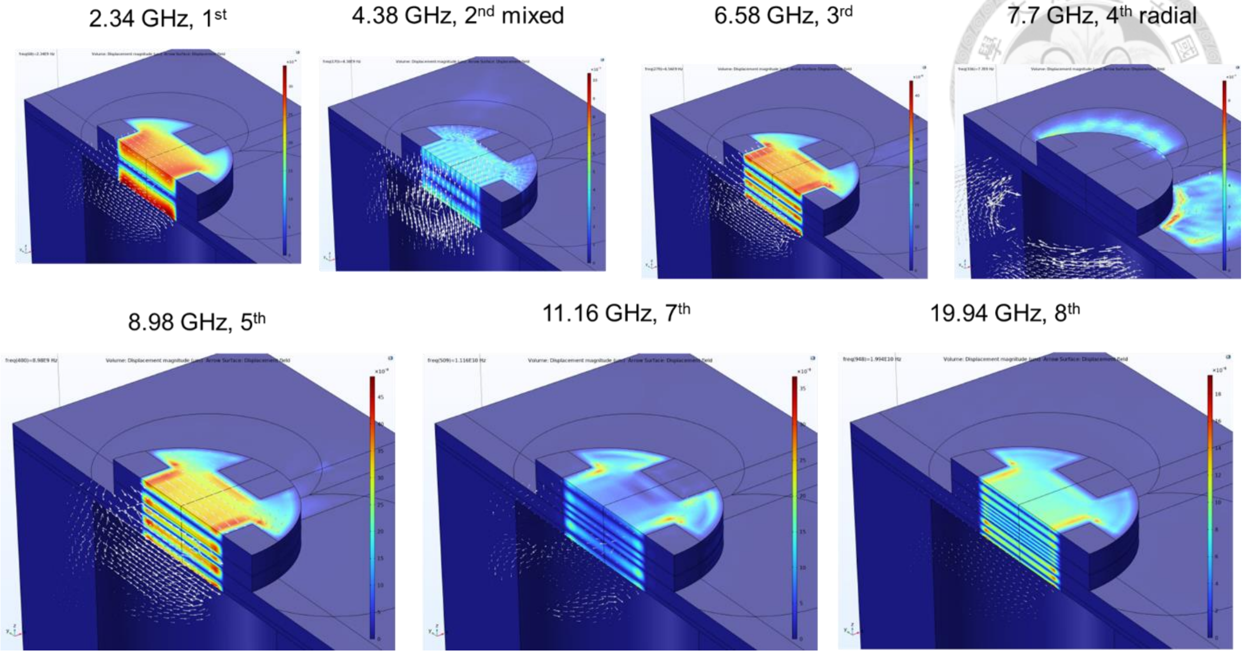
2.34 GHz, 1st
4.38 GHz, 2nd mixed
6.58 GHz, 3rd
7.7 GHz, 4th radial
8.98 GHz, 5th
11.16 GHz, 7th
19.94 GHz, 8th

Fig. 4.16. Mode shape of the simulated structure without floating potential.

these surfaces, all other structures are free. The impedance response of the simulated structure is shown in Fig. 4.13. There will be four resonance peaks around 3.2 GHz, 6.5 GHz, 10.7 GHz and 17.8 GHz. If we choose to ignore the metallic surface effect if magnetostrictive layer, the impedance response is shown in Fig. 4.14. It can be found that the impedance magnitude increases from 100 to 1000000 for the fundamental mode. Hence, it’s likely that all signals are reflected from a 50-ohm transmission line. Additionally, the resonant modes under 20 GHz becomes 7 modes with fundamental mode around 2.3 GHz. These observations lead to the conclusion that the presence of floating electrodes will mess up the electric field distribution around the excitation source. The current lateral electrodes are placed too far away, and the impedance is too high. As shown in Fig. 4.15 and Fig. 4.16, if we check the fundamental mode shape for both cases, it shows that ideal thickness shear modes can be excited only if the floating potential condition is eliminated. This further confirms that the metallic structure of magnetostrictive layer Nickel should be considered.

4.3 Fabrication Process

The step-by-step fabrication procedure is depicted in Fig. 4.18, with a breakdown of the material layers provided in Table 3. The process starts by depositing a 50 nm platinum layer onto a silicon substrate with a (100) orientation and a resistivity exceeding 104 Ω·cm. This is achieved using a CHA solution electron beam evaporator, and the platinum layer functions as the bottom electrode, patterned through a lift-off technique. Following this, a 400 nm aluminum nitride (AlN) thin film is deposited via reactive sputtering using a Tegal AMS AlN sputtering system. To create electrical connections to the bottom electrodes, the AlN layer undergoes selective wet etching using AZ 300 MIF developer and a KMPR 1005 mask.

Subsequently, a 100 nm aluminum layer is applied through evaporation with a CHA Mark 40 system to form the top electrodes and via contacts, followed by patterning through a lift-off process. A 300 nm nickel layer is then deposited using the same CHA Mark 40 system, serving as the magnetostrictive component, and is also patterned via lift-off. In certain experiments, the nickel layer is substituted with a 200 nm Permalloy (NiFe) layer, which offers distinct material properties. To improve adhesion and mitigate oxidation, a 400 nm aluminum oxide (Al_2O_3) buffer layer is incorporated. The final device geometry is shaped by plasma etching with chlorine gas, utilizing a Unaxis SLR770 ICP system and a KMPR 1005 mask.

Once fabrication is complete, the wafer is diced into individual components, and devices are released at the die level through isotropic silicon etching with XeF_2 gas in a custom system. Due to manufacturing constraints, the device radius was set at 200, 500, and 1000 μm, rather than the 9 μm specified in Chapter 4, as illustrated in Fig. 4.18 to Fig. 4.20. Additionally, an alternative version was produced using NiFe instead of Ni. This variation serves as a reference material due to its well-documented characteristics and near-zero magnetostriction, aiding in the evaluation of radiation effects.

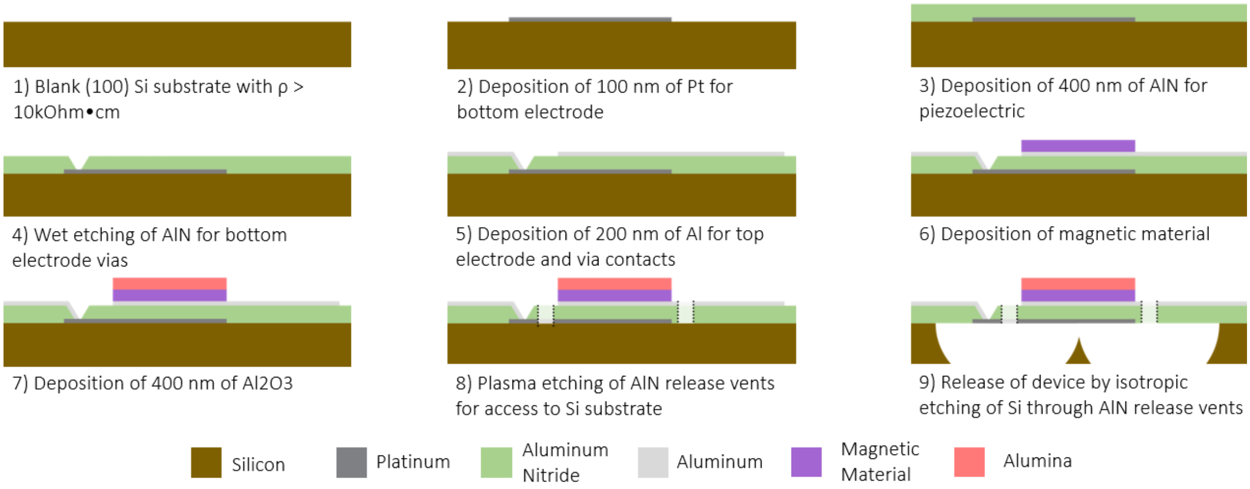

Fig. 4.17. Fabrication process of BAW antenna. Reproduced from [37].

doi:10.6342/NTU202501094

Table 3. Fabrication process of BAW antenna for each layer and action. Reproduced from [76].

Layer number	Name	Corresponding step	Action in fab
0	Si substrate	1	Blank Si substrate
1	Pt bottom electrode	2	100 nm Pt for bottom electrode
2	AlN piezoelectric	3	400 nm AlN piezoelectric
3	Al via	4	Wet etching of AlN for bottom electrode vias
4	Ni magnetic material/NiFe non-magnetoelastic testing material	6	300 nm Ni magnetic material/200 nm NiFe non- magnetoelastic testing material
5	Alumia buffer material	7	400 nm Al_2O_3
6	Al top electrode	5	200 nm Al top electrode
7	Release vents inside resonator	8, 9	1300 nm (thickness of bottom electrode, piezoelectric, magnetic material and alumia) plasma etching + isotropic etching for release vents
8	Release vents outside resonator	8, 9	700 nm (thickness of bottom electrode, piezoelectric, and alumia) plasma etching + isotropic etching for release vents

doi:10.6342/NTU202501094

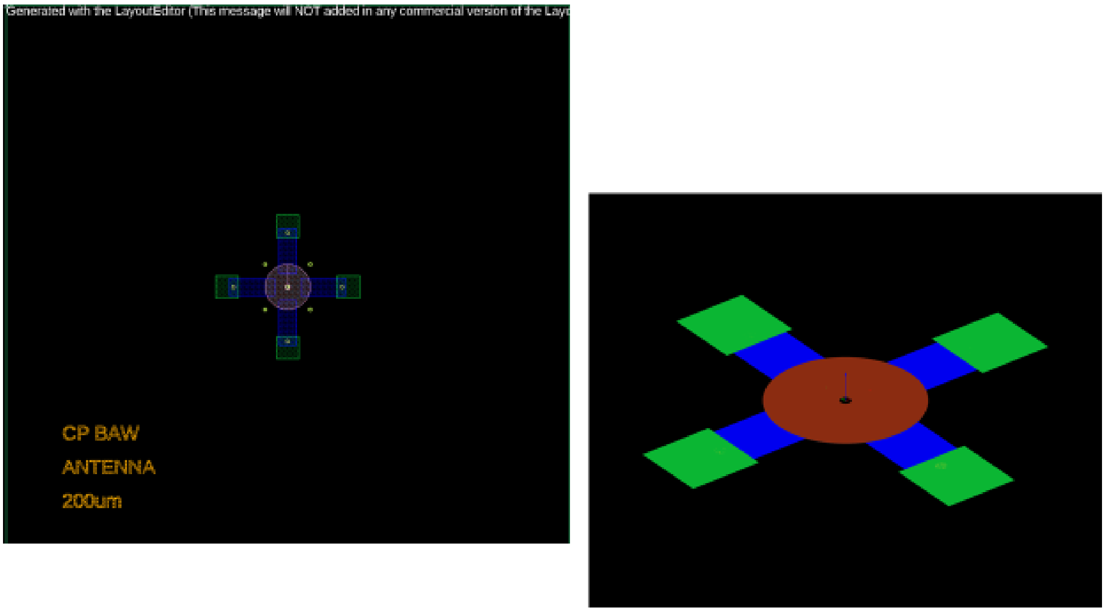

Fig. 4.18. Layout of the 200 μm circularly polarized BAW antenna. Reproduced from [79].

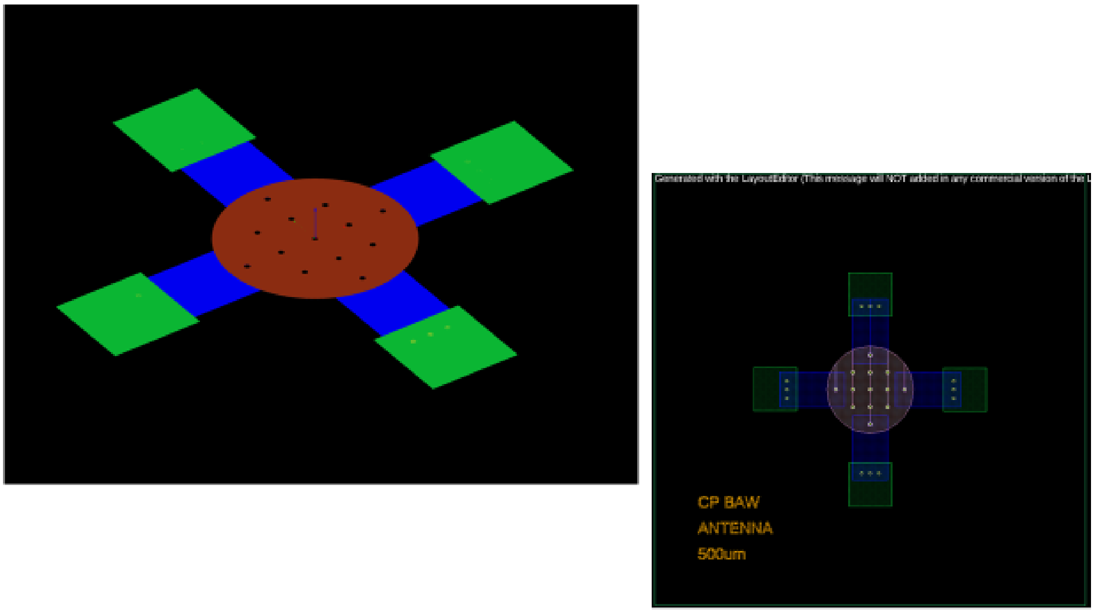

Fig. 4.19. 500 μm circularly polarized BAW antenna. Reproduced from [79].

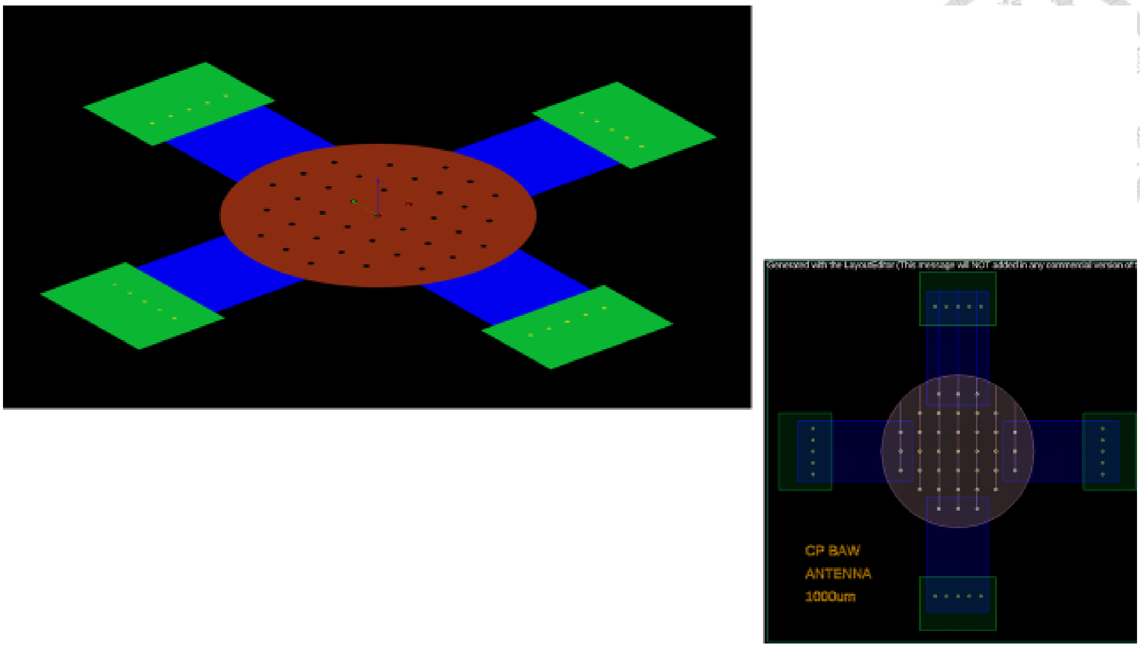

Fig. 4.20. Layout of 1000 μm CP BAW antenna. Reproduced from [79].

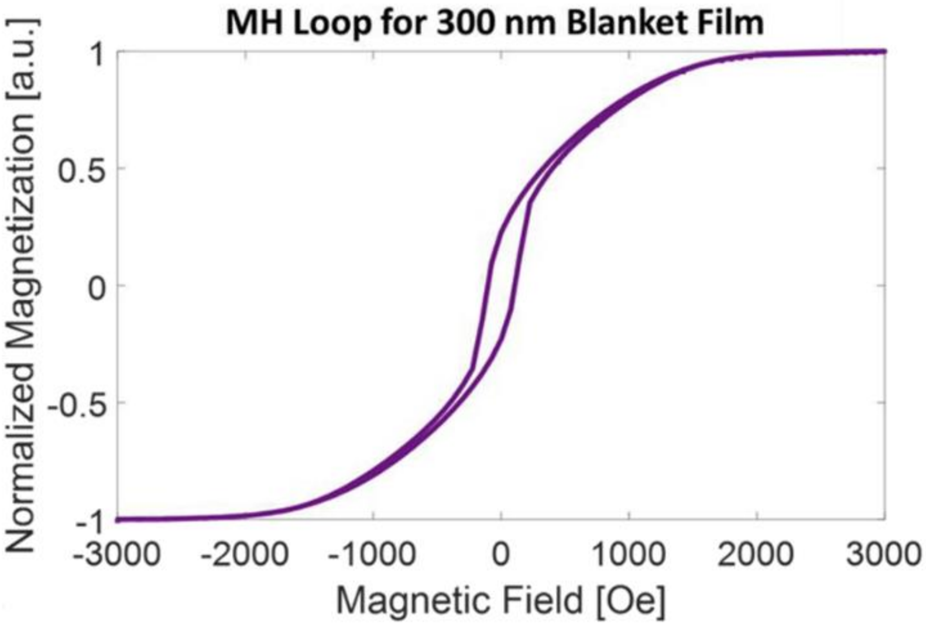

Fig. 4.21. The magnetic properties of the deposited 300 nm Ni film. Reproduced from [37].

The magnetic properties of the deposited 300 nm Ni film are characterized using a superconducting quantum interference device (SQUID). The measured hysteresis loop, shown in Fig. 4.21, indicates that the Ni film reaches saturation in fields exceeding approximately 2000 Oe.

A post-fabrication analysis of the material composition of the test pieces was conducted at the Semiconductor Fabrication Lab of the Consortia of Key Technologies and the Nano-Electro-Mechanical-System Research Center, National Taiwan University. Laser scanning optical images of the test pieces were captured using the KEYENCE VK-X200 series 3D laser scanning microscope, which provides 3D imaging capabilities for examining the structural details of the fabricated devices. To analyze the atomic composition, the Hitachi S-4800 scanning electron microscope (SEM) combined with the HORIBA EMAX x-act energy-dispersive X-ray spectroscopy (EDS) was used. The atomic composition at designated areas of each test piece was quantitatively extracted by comparing spectral data.

The analysis of a 500-μm-radius Ni test piece, with its optical image shown in Fig. 4.22, yielded the results presented in Fig. 4.23. The analysis spot, labeled "Spectrum 13," revealed that the primary atomic elements were oxygen (57.31%), aluminum (32.8%), nickel (9.02%), and silver (0.87%). The aluminum and oxygen originated from the Al_2O_3 acoustic buffer layer, while nickel constituted the middle magnetostrictive layer.

Similarly, a 500-μm-radius permalloy test piece, with its optical image shown in Fig. 4.24, was analyzed, and the results are displayed in Fig. 4.25. The analysis spot, labeled "Spectrum 9," indicated that the major atomic elements were oxygen (57.70%), aluminum (30.51%), nickel (8.35%), iron (2.46%), and silver (0.98%). As in the Ni test piece, aluminum and oxygen were attributed to the Al_2O_3 buffer layer, while nickel and iron comprised the middle layer. The Ni-to-Fe atomic ratio was approximately 77:23, closely matching the composition of standard $Ni_{78}Fe_{22}$ or $Ni_{80}Fe_{20}$ permalloy.

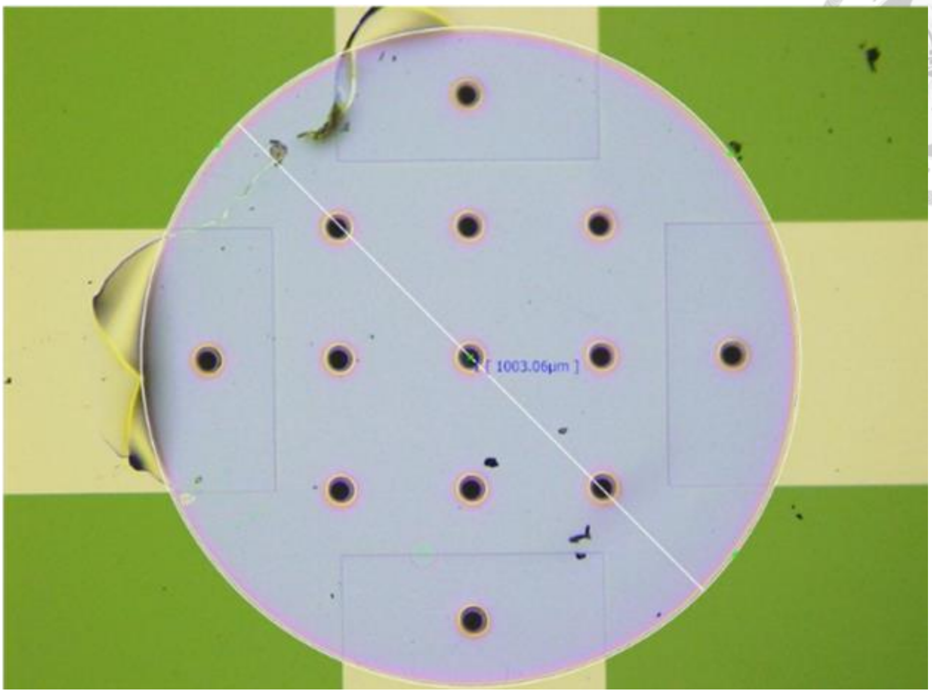

Fig. 4.22. Optical figure of 500-μm-radius Ni test piece. Reproduced from [80].

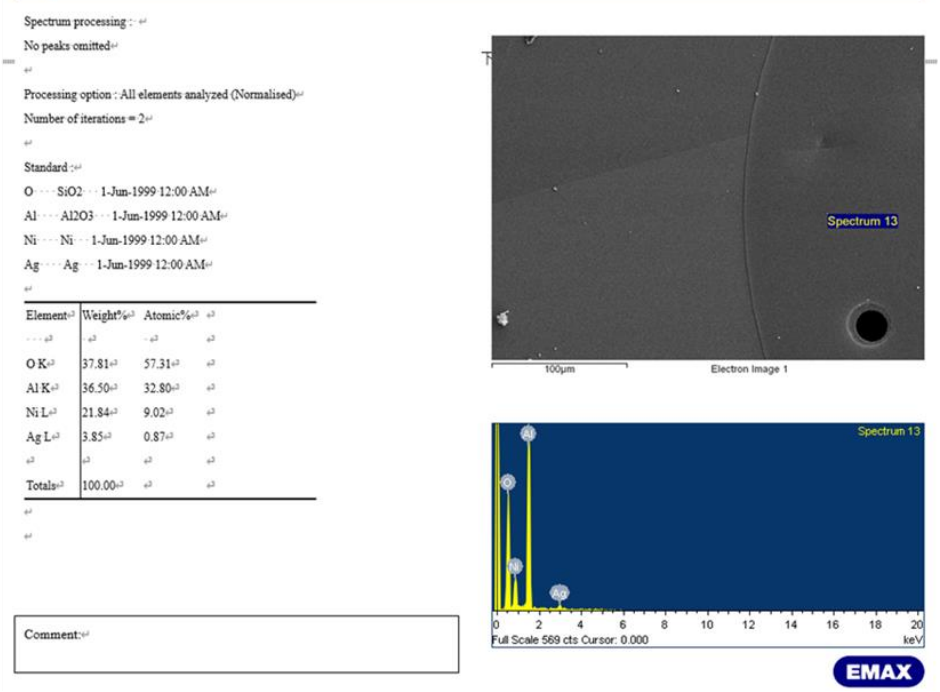

Spectrum processing :

No peaks omitted

Processing option : All elements analyzed (Normalised)

Number of iterations = 2

Standard :

O SiO2 1-Jun-1999 12:00 AM

Al Al2O3 1-Jun-1999 12:00 AM

Ni Ni 1-Jun-1999 12:00 AM

Ag Ag 1-Jun-1999 12:00 AM

Element	Weight%	Atomic%
O K	37.81	57.31
Al K	36.50	32.80
Ni L	21.84	9.02
Ag L	3.85	0.87
Totals	100.00	

Comment:

Fig. 4.23. SEM-EDS results of 500-μm-radius Ni test piece. Reproduced from [80].

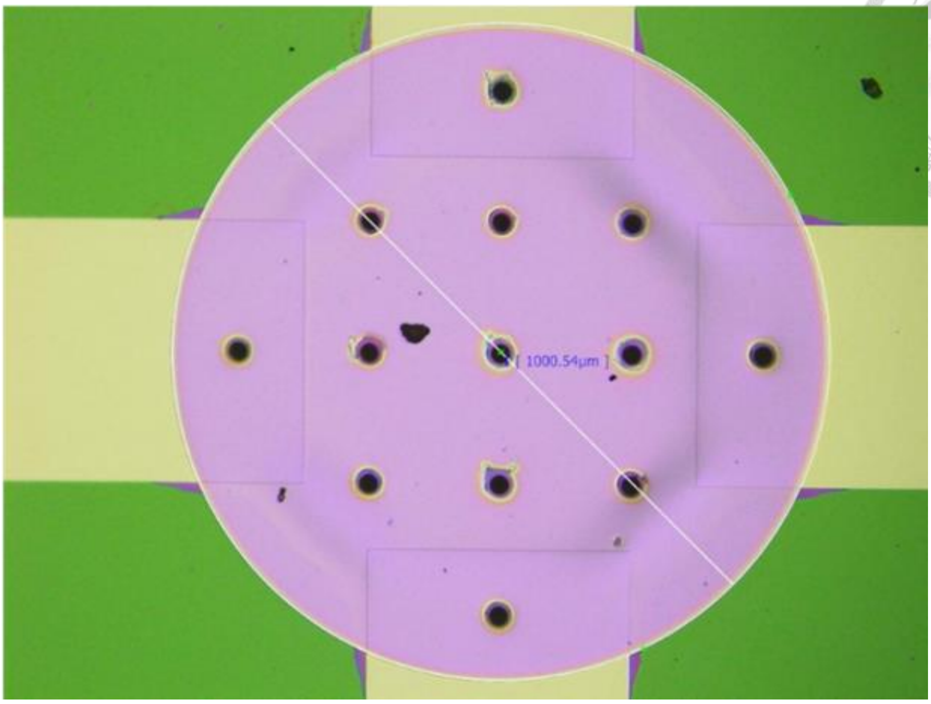

Fig. 4.24. Optical figure of 500-µm-radius NiFe test piece. Reproduced from [80].

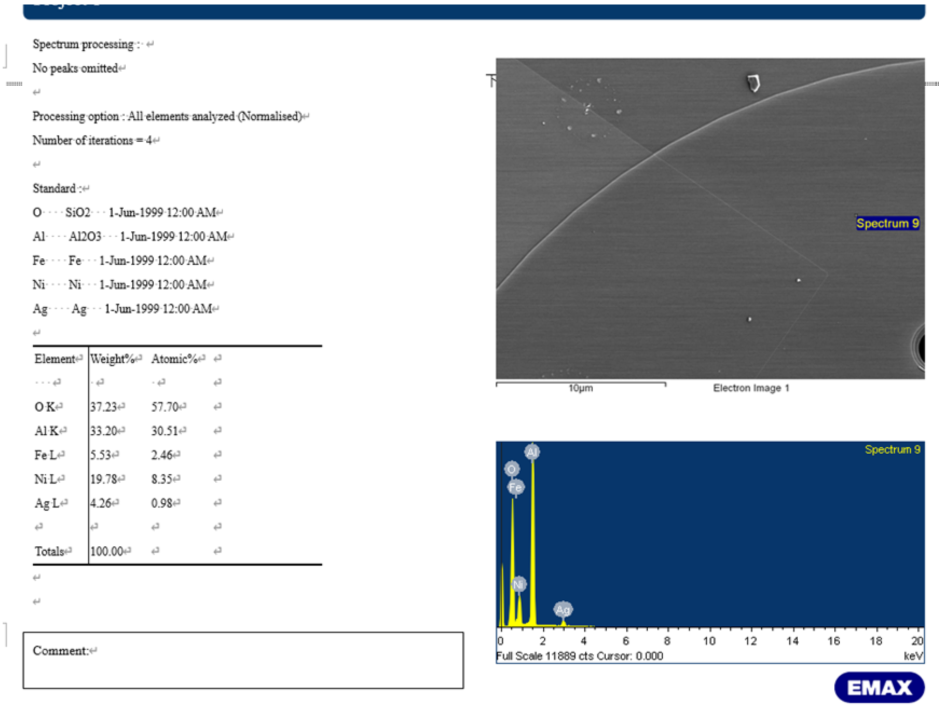

Spectrum processing :

No peaks omitted

Processing option : All elements analyzed (Normalised)

Number of iterations = 4

Standard :

O SiO2 1-Jun-1999 12:00 AM

Al Al2O3 1-Jun-1999 12:00 AM

Fe Fe 1-Jun-1999 12:00 AM

Ni Ni 1-Jun-1999 12:00 AM

Ag Ag 1-Jun-1999 12:00 AM

Element	Weight%	Atomic%
O K	37.23	57.70
Al K	33.20	30.51
Fe L	5.53	2.46
Ni L	19.78	8.35
Ag L	4.26	0.98
Totals	100.00	

Comment:

Fig. 4.25. SEM-EDS results of 500-µm-radius NiFe test piece. Reproduced from [80].

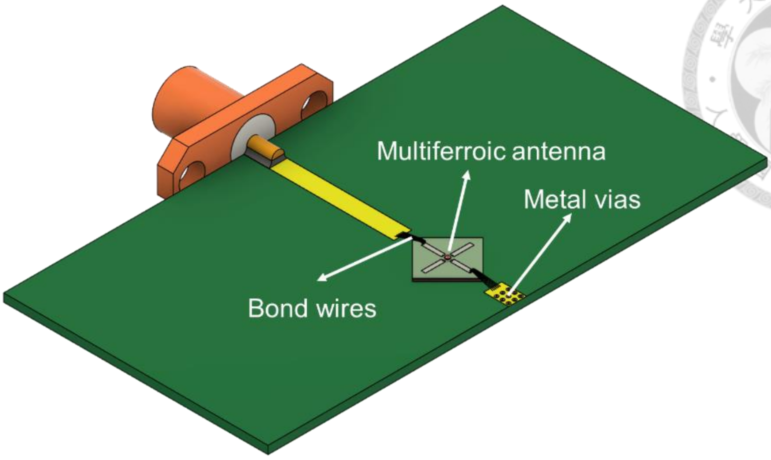

Fig. 4.26. Antenna mounted onto a printed circuit board (PCB) sample holder. Reproduced from [80].

4.4 Measurements Setup

The antenna is secured onto a printed circuit board (PCB) fixture, as shown in Fig. 4.26. To establish electrical connections, aluminum bond wires link the outer electrodes to the PCB’s copper microstrip traces. One of these microstrip traces extends to an SMA connector for signal transmission, while the other is grounded by copper vias that connect it to the bottom ground plane.

doi:10.6342/NTU202501094

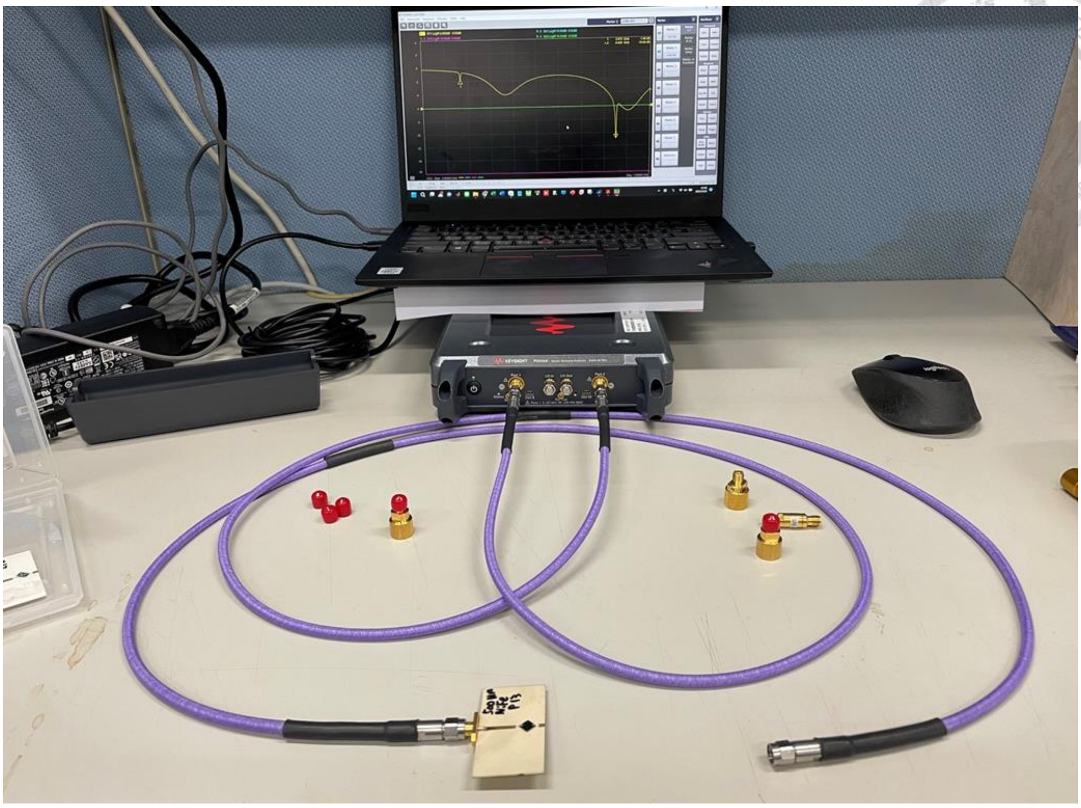

Fig. 4.27. Photograph of the experimental setup. Reproduced from [80].

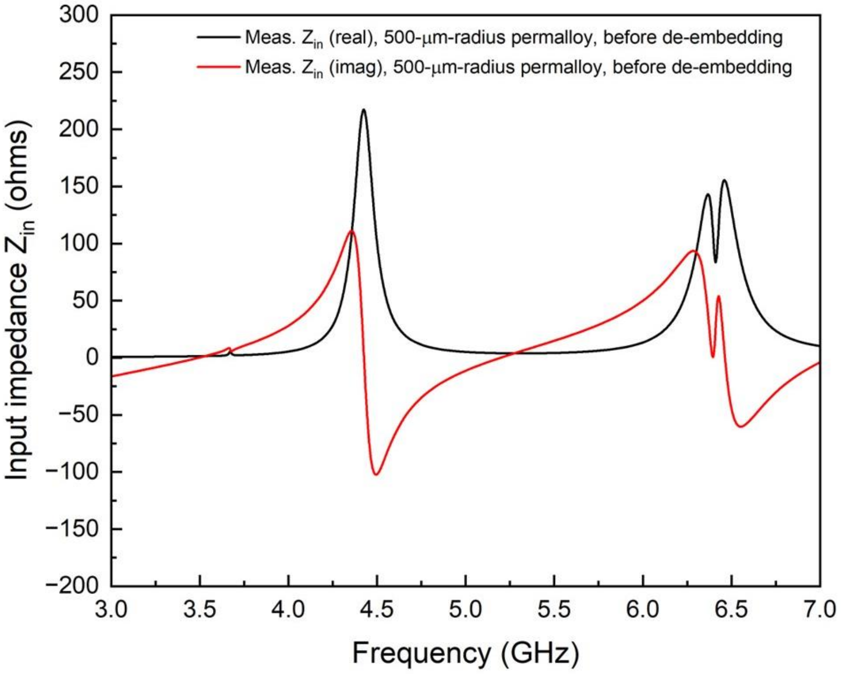

Fig. 4.28. Impedance measurement before de-embedding. Reproduced from [80].

In addition to analyzing the simulated mode shapes in the previous chapter by device

doi:10.6342/NTU202501094

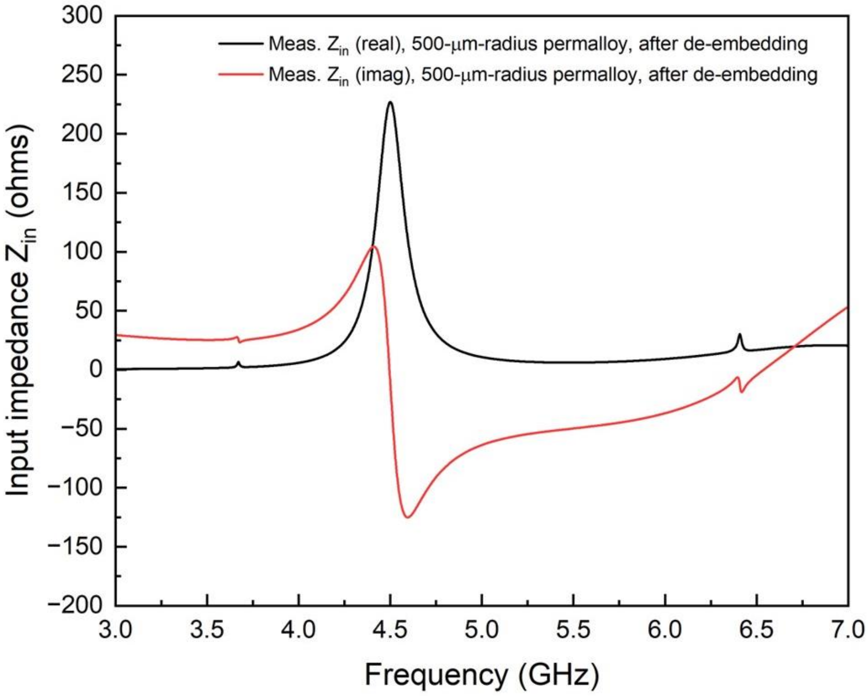

Fig. 4.29. Impedance measurement after de-embedding. Reproduced from [80].

simulation, we also employed the standard through-reflect-line (TRL) calibration technique for de-embedding to confirm the presence of mechanical resonances. A photograph of the experimental setup is shown in Fig. 4.27. The TRL calibration kits were designed to eliminate the influence of microstrip lines on the PCB sample holder.

The input impedance of the prototype antenna was measured using the TRL calibration method with the Keysight 2-port VNA P5004A, referred to as the "after de-embedding" measurement. For comparison, we also conducted an input impedance measurement using the conventional 2-port short-open-load-through (SOLT) calibration under the same setup, referred to as "before de-embedding." In this case, the measurement included the effect of the microstrip lines on the PCB sample holder. The measured results before and after de-embedding are presented in Fig. 4.28 and Fig. 4.29, respectively.

While the two mechanical resonances remained at the same frequencies, parasitic resonances were effectively removed in the "after de-embedding" measurement, demonstrating the successful elimination of the microstrip line effects on the PCB.

After comfirming the existence of mechanical resonance, we can move on to measure the radiation performance of the antenna-under-test (AUT). All measurements in this study were conducted using the two-port Keysight P5004A Streamline USB Vector Network Analyzer (VNA). The intermediate frequency (IF) bandwidth and output power of the VNA were set to 1 kHz and –10 dBm, respectively. The frequency range spanned from 2 to 8 GHz, with a total of 6001 frequency points and a frequency step of 1 MHz. The standard two-port Short-Open-Load-Through (SOLT) calibration was performed using the Agilent 85052D mechanical calibration kit.

A linearly polarized double-ridged broadband horn antenna (WavePro Inc. DRH0118) was selected due to its 10–12 dBi gain across the 2–8 GHz band. The antenna under test (AUT) and the horn antenna were connected to the VNA using GORE PHASEFLEX 2.92 mm RF cables. The horn antenna had a maximum linear dimension of 28.7 cm, while the shortest free-space wavelength in the measurement band was 3.75 cm at 8 GHz. Accordingly, the minimum radiating near-field distance for the horn antenna was calculated as 49.2 cm using the formula $0.62\sqrt{\frac{D^3}{\lambda}}$.

For the AUT, considering the 200-μm-radius Ni case, the maximum resonating area was 400 μm—significantly smaller than the shortest wavelength (3.75 cm at 8 GHz). As a result, the AUT qualified as an electrically small antenna, with a far-field distance

doi:10.6342/NTU202501094

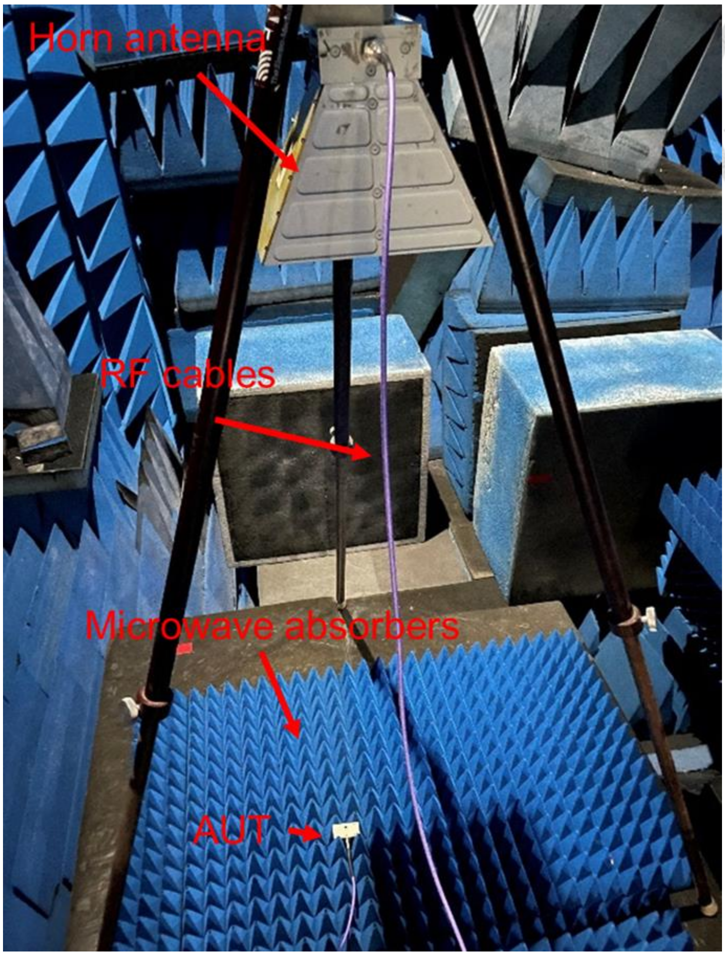

Fig. 4.30. Photographs of the experimental setup. Reproduced from [80].

approximated as $\frac{\lambda_{max}}{2\pi} \cong 2.4\ cm$, where λ_{max} = 15 cm (corresponding to 2 GHz). Even when including the PCB sample holder, the minimum radiating near-field distance for the AUT was estimated at $0.62\sqrt{\frac{D^3}{\lambda}} \cong 5.4\ cm$, and the far-field distance was approximately 17 cm using $\frac{2D^2}{\lambda_{min}} \cong 17\ cm$, where the PCB's maximum dimension was 5.66 cm. To ensure both near-field and far-field conditions were met, the spacing between the AUT and the horn antenna was set to 130 cm—well beyond the required distances.

Measurements of the reflection and transmission coefficients ($|S_{11}|$ and $|S_{21}|$) were performed inside the microwave anechoic chamber at National Taiwan University.

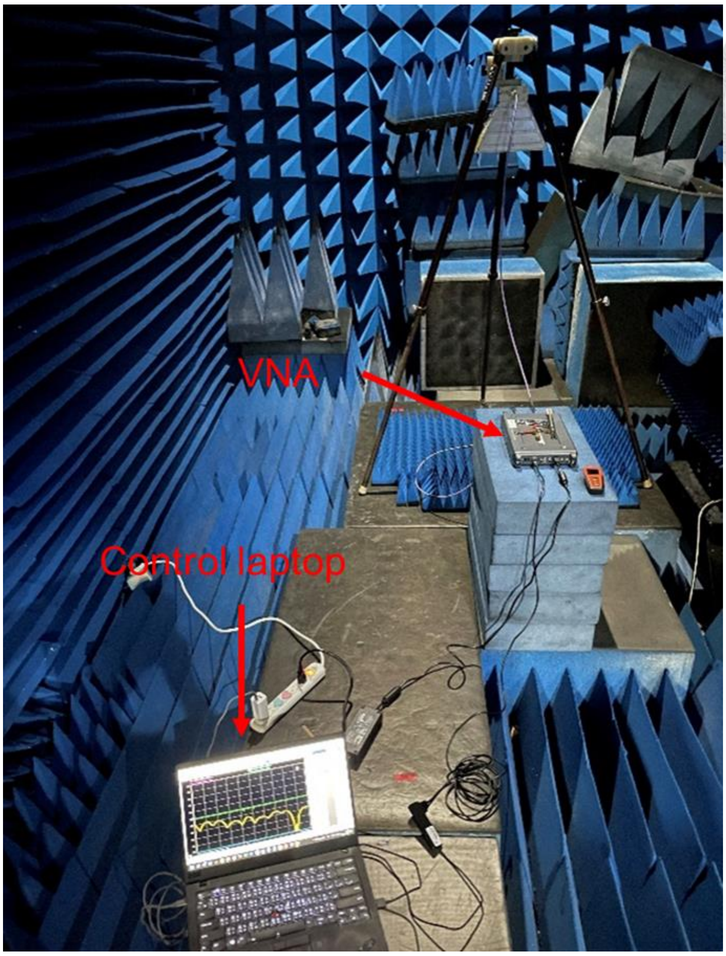

Fig. 4.31. Photographs of the experimental setup. Reproduced from [80].

Photographs of the experimental setup are provided in Fig. 4.30 and Fig. 4.31. The receiving horn antenna was mounted on a non-metallic tripod, while the AUT, acting as the transmitting antenna, was placed on microwave absorbers to minimize floor reflections. The AUT-horn antenna spacing was fixed at 130 cm. The common two-port SOLT calibration was performed, with reference planes set at the connectors of both the horn antenna and the AUT. To measure the co-polarized (co-pol) transmission coefficient $|S_{21}|$, the polarization of the horn antenna and AUT was aligned. Cross-polarization (x-pol) measurements were taken by rotating the AUT 90°. To assess the environmental noise level, the AUT was replaced with a broadband matched load, as depicted in Fig. 4.32. This load absorbed the incident VNA signal, resulting in a transmission coefficient

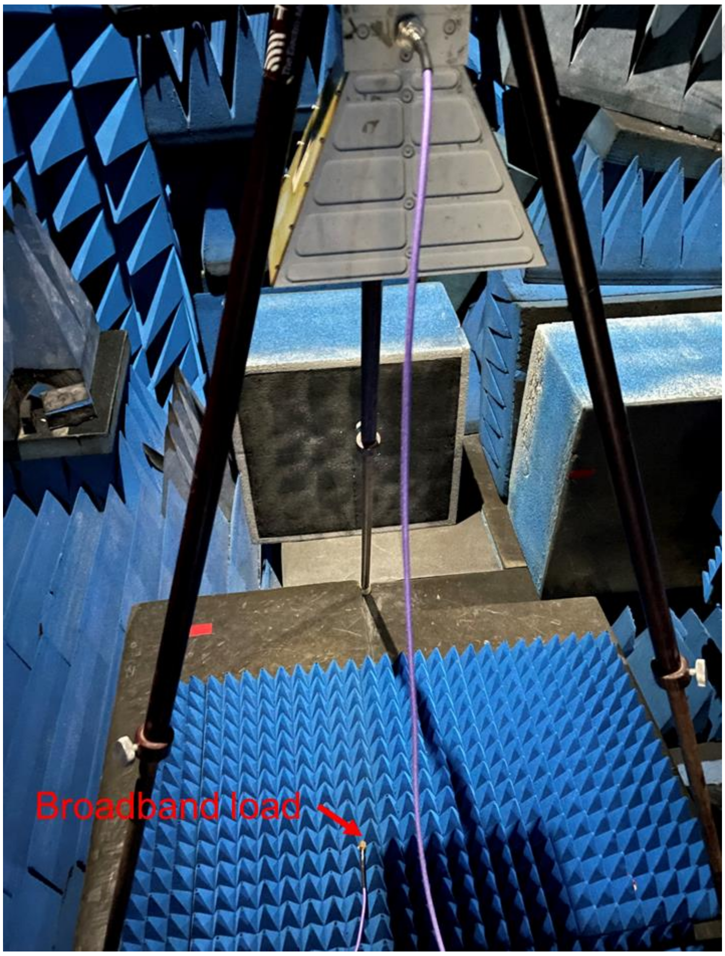

Fig. 4.32. Photographs of the experimental setup. Reproduced from [80].

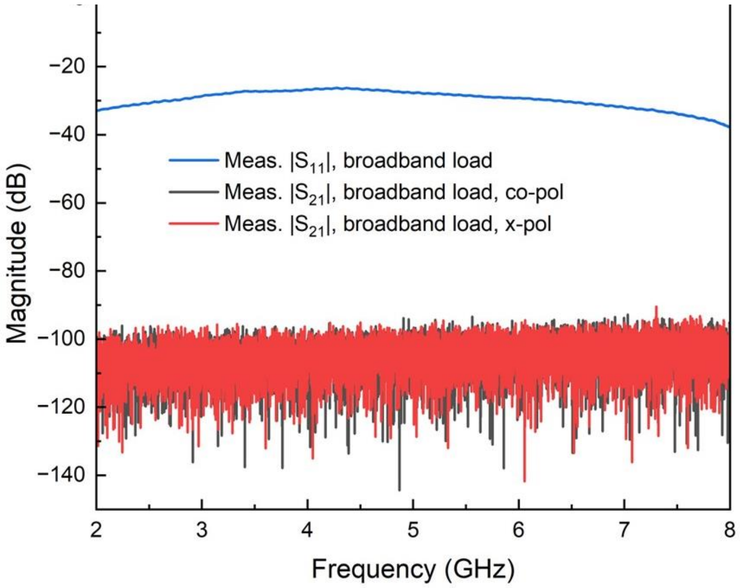

Fig. 4.33. Photographs of the experimental setup. Reproduced from [80].

$|S_{21}|$ overwhelmed by noise, as shown in Fig. 4.33. The $|S_{21}|$ responses for both co-pol and

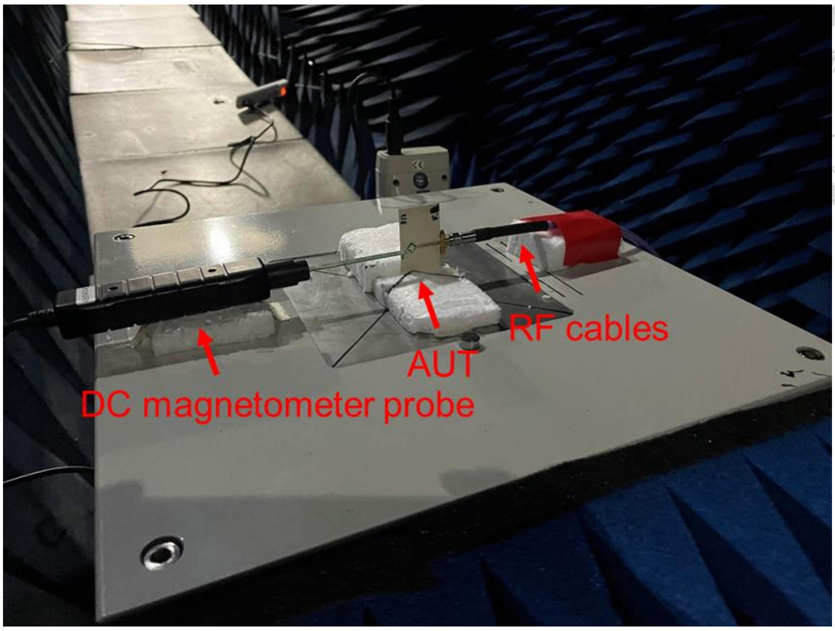

Fig. 4.34. Photographs of the experimental setup. Reproduced from [80].

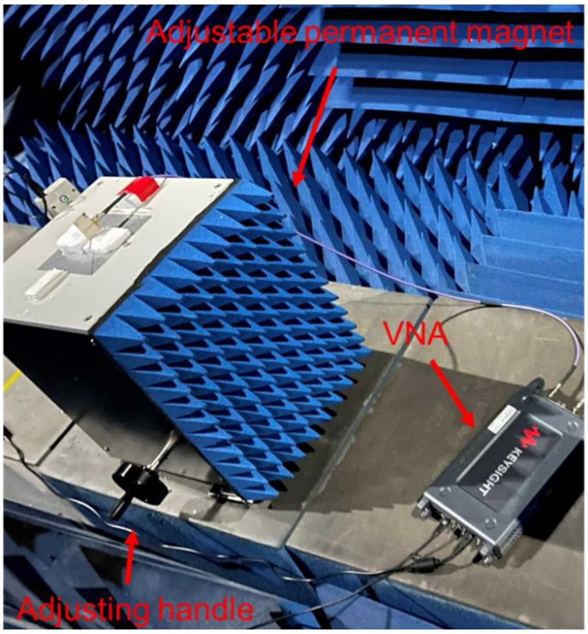

Fig. 4.35. Photographs of the experimental setup. Reproduced from [80].

x-pol configurations were similar, both showing a noise floor of approximately -100 dB.

To measure the bias static magnetic field applied during the experiments, a Lutron MG-3003SD magnetic meter was used. A Hall sensor probe was fixed near the multi-layered disk region of the AUT to continuously monitor and record the applied static magnetic field for each test. The bias field was supplied by a magnetoelectric unipolar

doi:10.6342/NTU202501094

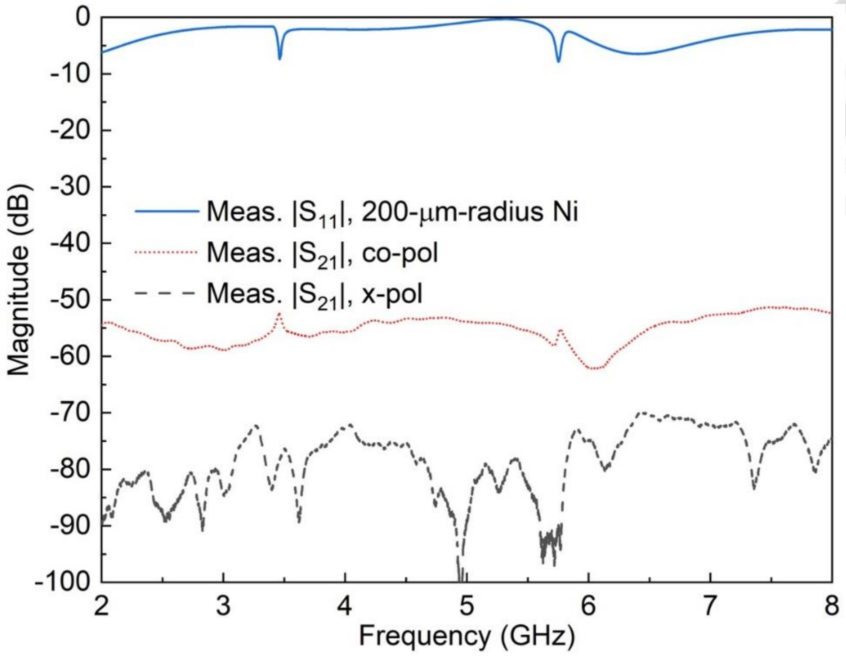

Fig. 4.36. The measured scattering parameters. Reproduced from [80].

adjustable magnetic field generator from Changchun Yingpu Magnetoelectric Technology Development Co., Ltd., which allowed for precise adjustment of the field strength.

Photographs of the experimental setup for bias static magnetic field measurement are shown in Fig. 4.34 and Fig. 4.35. The applied static magnetic field was adjusted by rotating the handle of the unipolar magnetic field generator. The Hall sensor probe was initially placed near the AUT to record the applied field and then removed before measurement to prevent interference. Once the static magnetic field was set and recorded, the reflection coefficient $|S_{11}|$ of the AUT under the applied field was measured using the VNA.

4.5 Results and Discussions

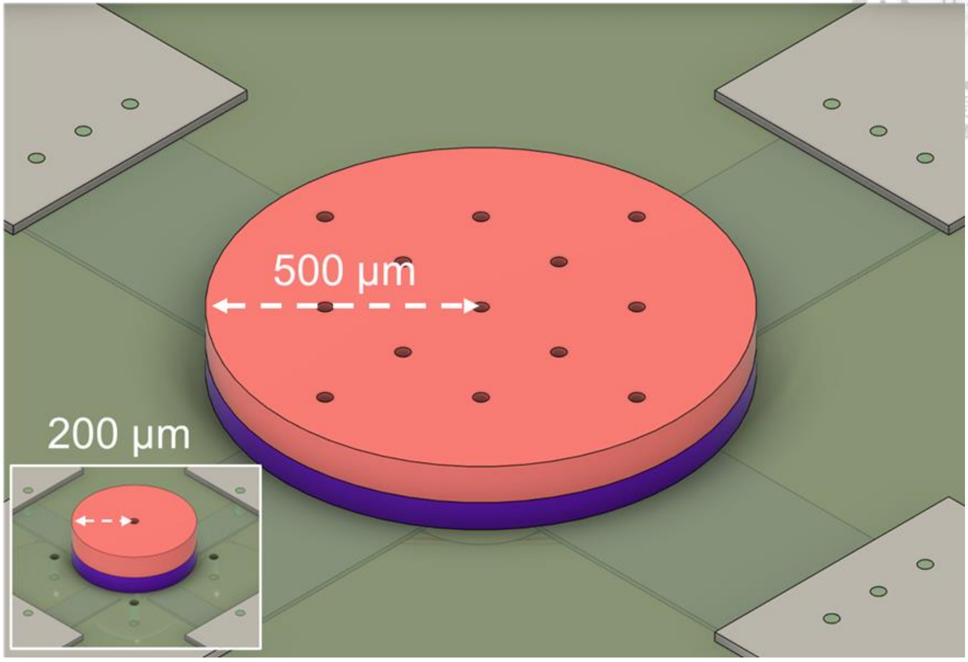

Fig. 4.37. 500-μm multiferroic disk. Reproduced from [80].

Fig. 4.36 presents the measured scattering parameters, with insets depicting the mode shapes of two distinct mechanical resonances. Consistent with previous findings, the co-polarized transmission $|S_{21}|$ exhibits peaks at 3.459 GHz and 5.768 GHz, which align with the narrow-band mechanical resonances identified by dips in the reflection $|S_{11}|$. Notably, no external static magnetic field is applied to induce or amplify radiation. A comparison between co-polarized and cross-polarized transmission responses reveals that the dominant radiation from the antenna under test (AUT) is linearly polarized along the electrode pair responsible for excitation. The gain from the AUT can be estimated by the Friis equation. We know that the distance is 1.3 m, the freqnecy is 3.462 GHz, $|S_{21}|$ is -52.43 dB and the gain from SGA is 10.07 dBi. The cable losses have already been calibrated so they don't need to be considered. Finally, the gain is estimated to be -17.03 dBi.

doi:10.6342/NTU202501094

The analysis then shifts to the magnetostrictive layer. In low-frequency applications, $Ni_{80}Fe_{20}$ or $Ni_{78}Fe_{22}$ (Permalloy) is commonly used due to its negligible magnetostriction.

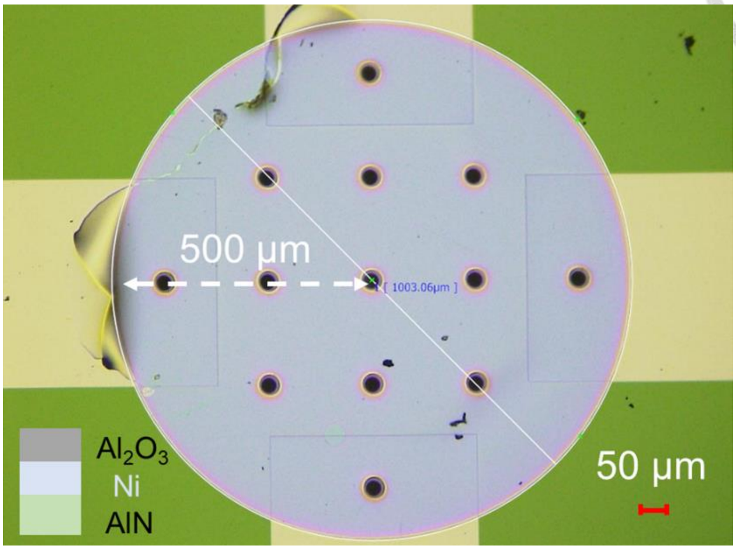

Fig. 4.38. 500-μm Ni multiferroic disk. Reproduced from [80].

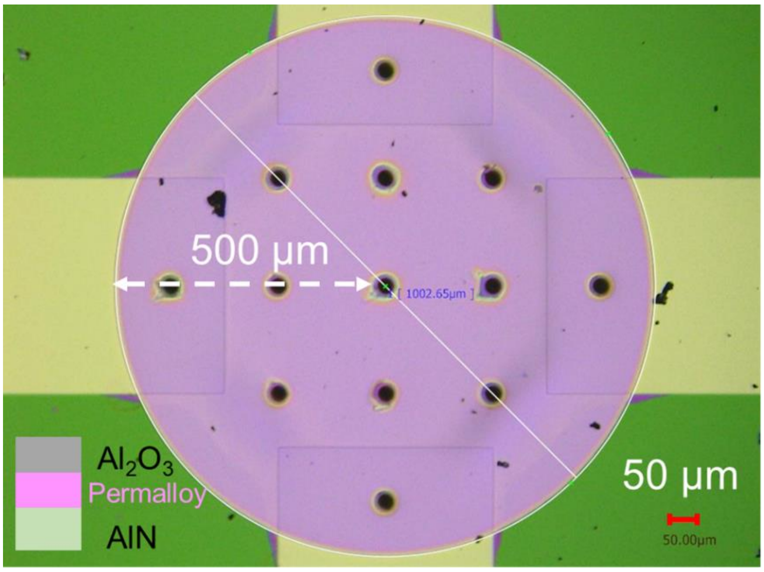

Fig. 4.39. 500-μm NiFe multiferroic disk. Reproduced from [77].

Rather than replacing the magnetostrictive layer with a non-magnetic metal, Permalloy—a magnetic but non-magnetoelastic material—is selected to assess its radiation characteristics. For consistency, both the experimental and control devices utilize the same three-layer structure. The only modification is an increase in the central multiferroic disk radius from 200 μm to 500 μm, as illustrated in Fig. 4.37.

doi:10.6342/NTU202501094

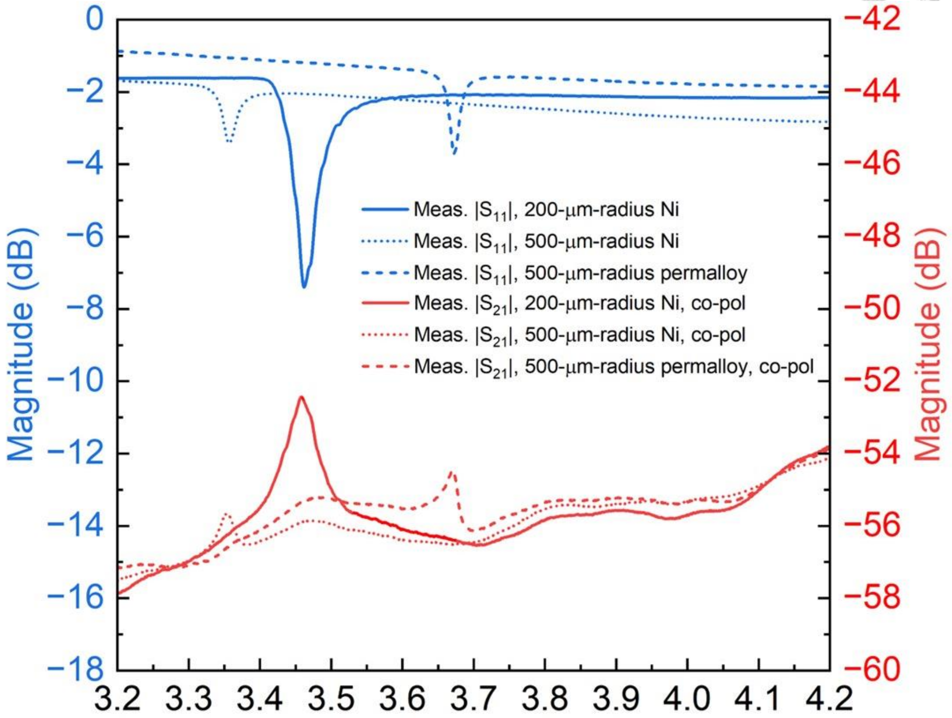

Fig. 4.40. 500-μm measured scattering parameters at lower resonance. Reproduced from [80].

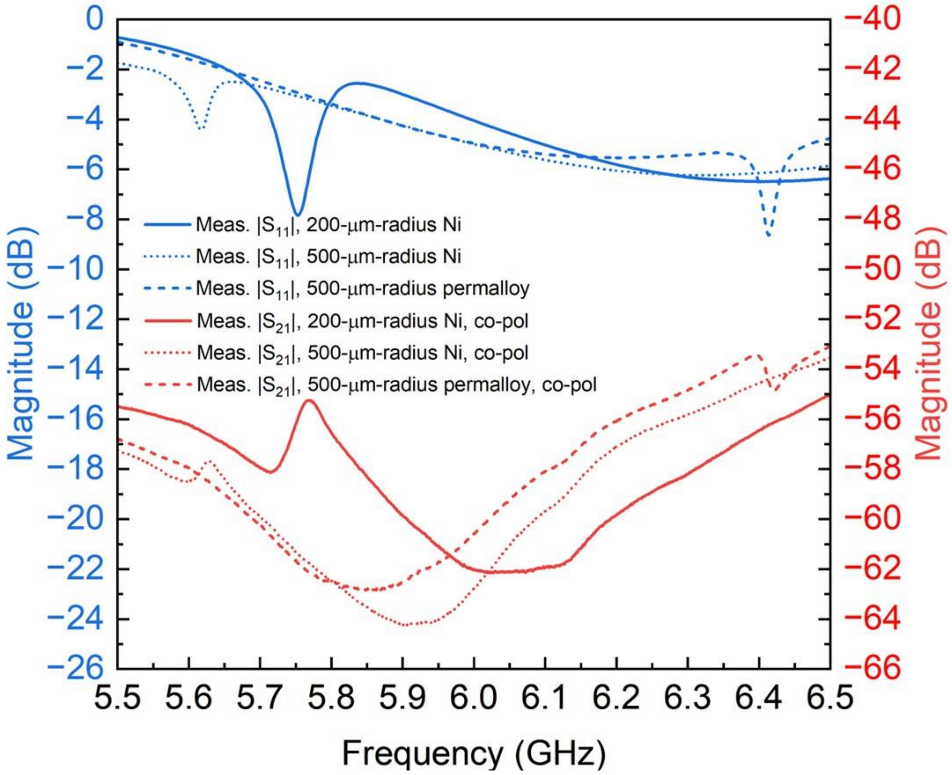

Fig. 4.41. 500-μm measured scattering parameters at higher resonance. Reproduced from [80].

For the device with a 500-μm-radius Ni layer, the consistency of mechanical

doi:10.6342/NTU202501094

resonance frequencies suggests that thickness plays a dominant role in defining resonant modes, particularly for thickness-shear vibrations. In the fabricated multiferroic devices, the Ni layer is 300 nm thick, whereas in the experimental 500-μm-radius permalloy device, the permalloy layer is reduced to 200 nm to compensate for its lower Young's modulus. This adjustment ensures that the resonant frequencies remain as close as possible to those of the control device. Microscope images comparing the control device and the experimental non-magnetoelastic magnetic device are provided in Fig. 4.38 and Fig. 4.39. The atomic composition analysis indicates that the device in Fig. 4.38 has a Ni-to-Fe ratio of approximately 77:23, while the control device in Fig. 4.39 contains no detectable Fe. Both devices are mounted on a PCB fixture, and their transmission and reflection responses are measured using an identical setup.

Fig. 4.40 and Fig. 4.41 compare the transmission characteristics of three devices—200-μm-radius Ni, 500-μm-radius Ni, and 500-μm-radius permalloy—at resonance frequencies near 3.5 GHz and 6 GHz. Several key observations emerge from the data. First, the mechanical resonance strength is lower in both 500-μm-radius Ni and permalloy devices compared to the 200-μm-radius Ni device. Second, the thinner permalloy layer in the 500-μm-radius NiFe device leads to a slight increase in resonant frequency. However, the resonant frequencies of the 200-μm and 500-μm-radius Ni devices remain relatively close, reinforcing the idea that device thickness, rather than lateral dimensions, primarily dictates resonance behavior. Third, all three configurations successfully operate as transmitting devices. This confirms that Ni, as a magnetoelastic material, consistently produces magnetically induced radiation at the 3.5-GHz resonance. Interestingly, despite its significantly weaker magnetoelastic properties, permalloy exhibits a comparable behavior at the lower resonance frequency.

doi:10.6342/NTU202501094

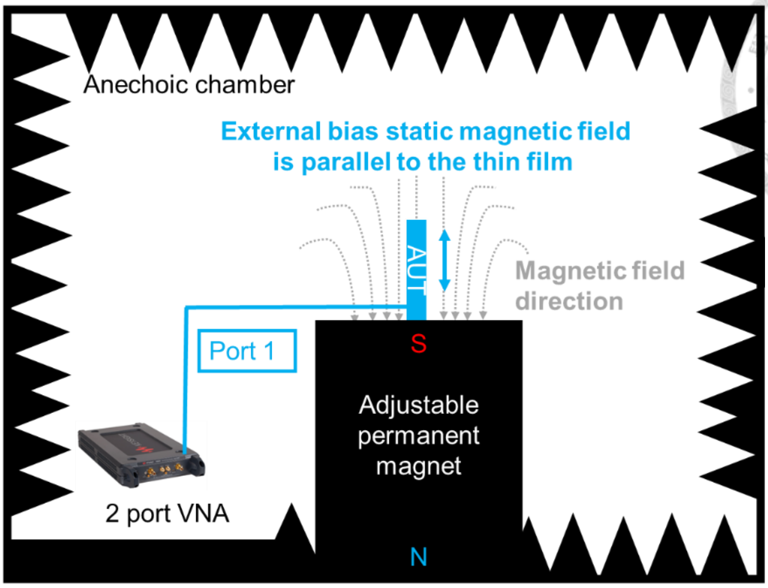

Fig. 4.42. Measurement setup for bias magnetic field test. Reproduced from [80].

For the higher resonant frequency at around 6 GHz, as shown in Fig. 4.41, the Ni devices again exhibit magnetically induced radiation, while the permalloy case demonstrates damped power absorption behavior. The distinct behavior of the 500-µm-radius Ni and permalloy cases at this higher frequency suggests that the observed radiation is influenced by the magnetoelastic properties rather than parasitic resonances, as the two devices are otherwise identical except for their magnetic layers.

To further verify this behavior, the effect of an external bias static magnetic field on all three devices is examined. An adjustable permanent magnet is used to provide the bias static magnetic field. Due to the thin-film nature of the devices, the out-of-plane demagnetizing field component is dominant. Thus, the focus is on applying the bias static magnetic field along the in-plane direction, which allows for easier magnetization of the magnetic layer (Ni or permalloy). The measurement setup is schematically depicted in Fig. 4.42.

doi:10.6342/NTU202501094

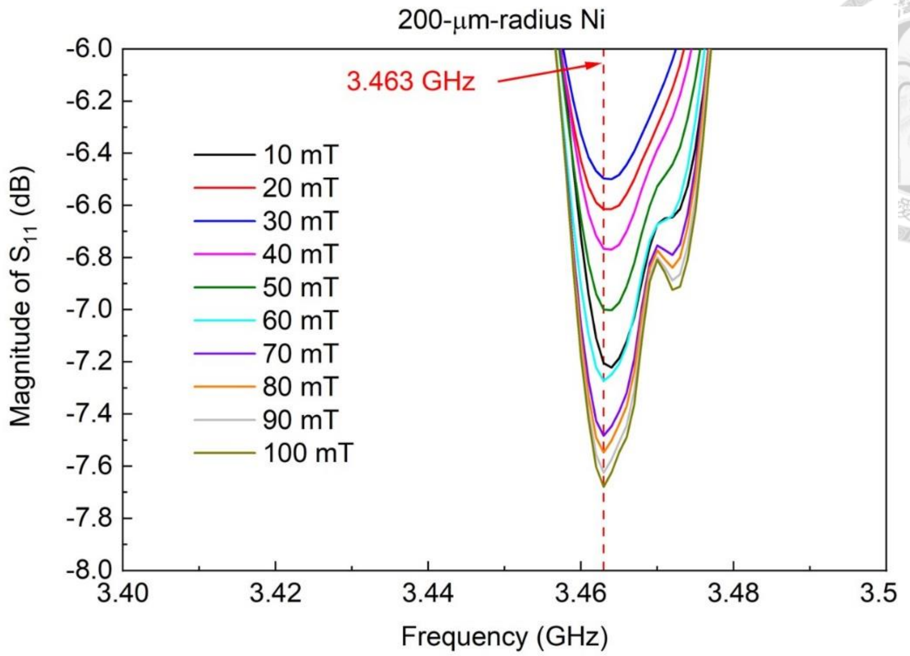

Fig. 4.43. Bias magnetic field test for lower resonance. Reproduced from [80].

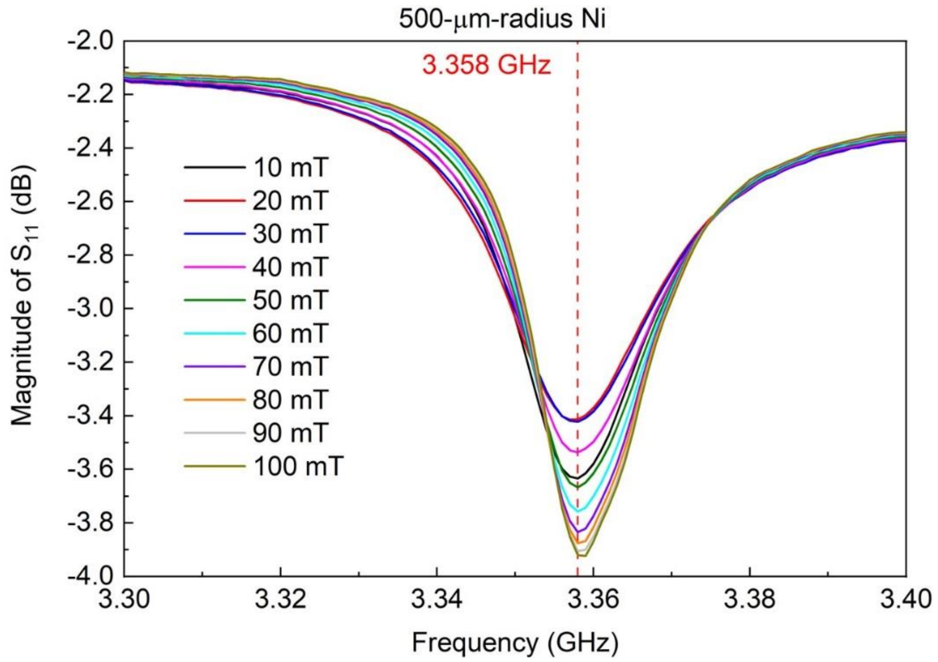

Fig. 4.44. Bias magnetic field test for lower resonance. Reproduced from [80].

During testing, the antenna under test (AUT)—whether the 200-μm-radius Ni, 500-μm-radius Ni, or 500-μm-radius permalloy device—is connected to port one of the vector

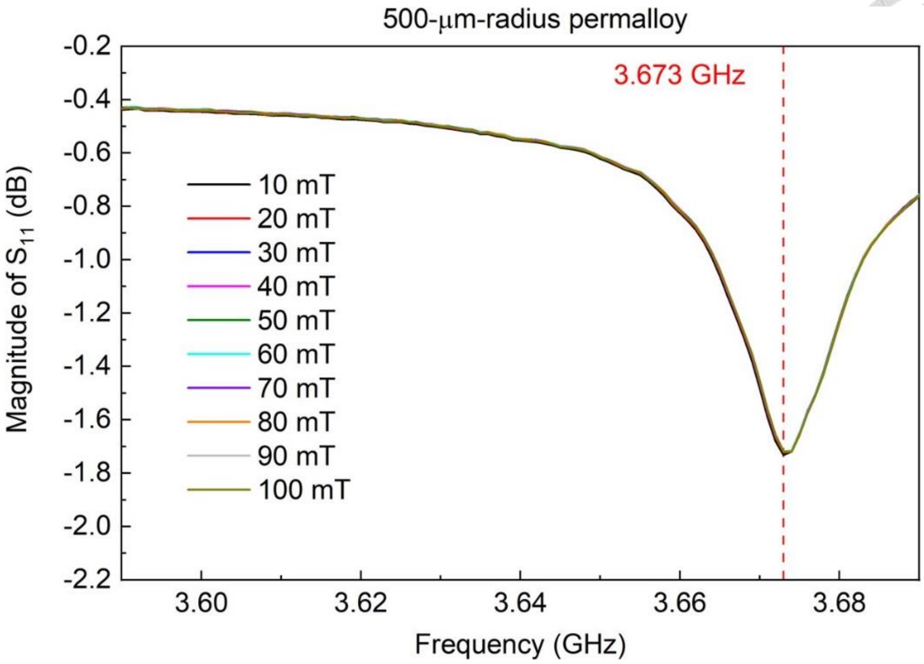

Fig. 4.45. Bias magnetic field test for lower resonance. Reproduced from [80].

network analyzer (VNA) and placed above an adjustable permanent magnet. This setup ensures that the applied static magnetic field aligns parallel to the in-plane direction of the thin-film magnetic layer. A Hall sensor probe is positioned close to the AUT to measure the static magnetic field strength, which is then removed before capturing the reflection coefficient $|S_{11}|$ responses under various field conditions. The $|S_{11}|$ measurements corresponding to the lower resonance frequency are displayed in Fig. 4.43 through Fig. 4.45, while those for the higher resonance frequency are provided in Fig. 4.46 through Fig. 4.48.

It is important to note that for all devices, the measured responses remain unchanged when the applied magnetic field exceeds 100 mT, and thus, data beyond this range are omitted for clarity. For fields ranging from 10 to 100 mT, the Ni test pieces (200-μm and

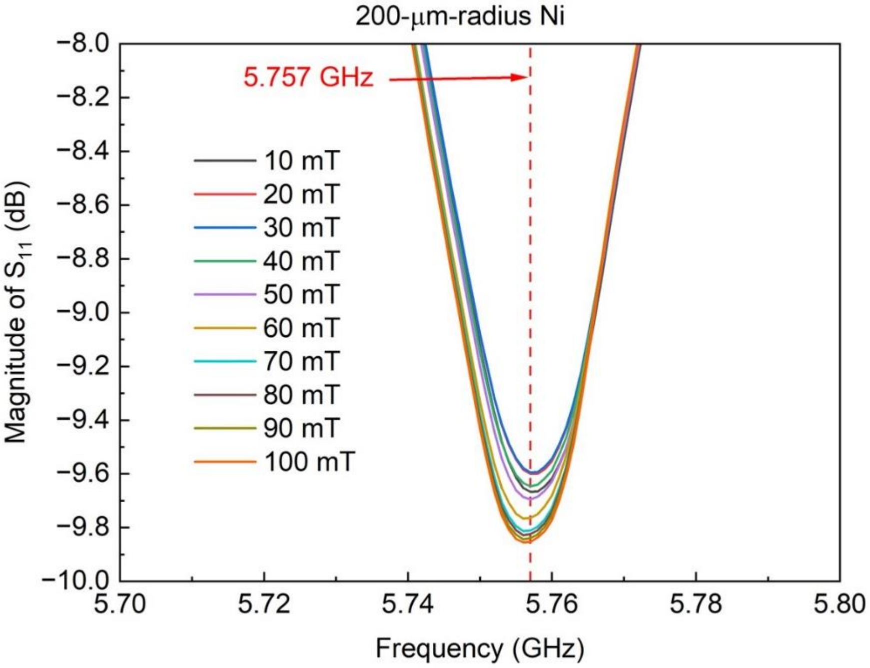

Fig. 4.46. Bias magnetic field test for higher resonance. Reproduced from [80].

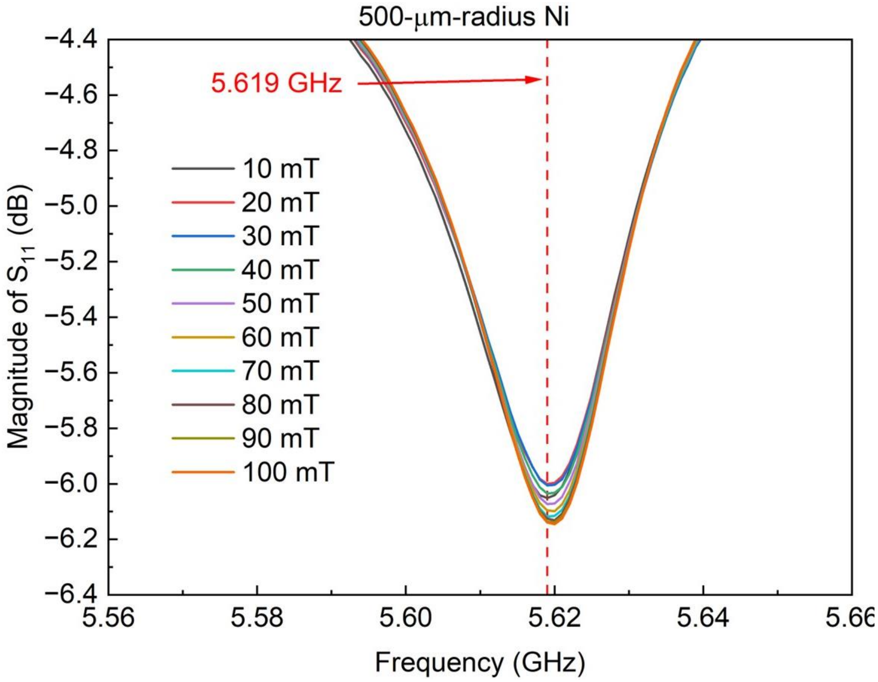

Fig. 4.47. Bias magnetic field test for higher resonance. Reproduced from [80].

500-μm radius) exhibit distinct behavior compared to the 500-μm-radius permalloy device. As expected, the mechanical resonance of the permalloy device remains

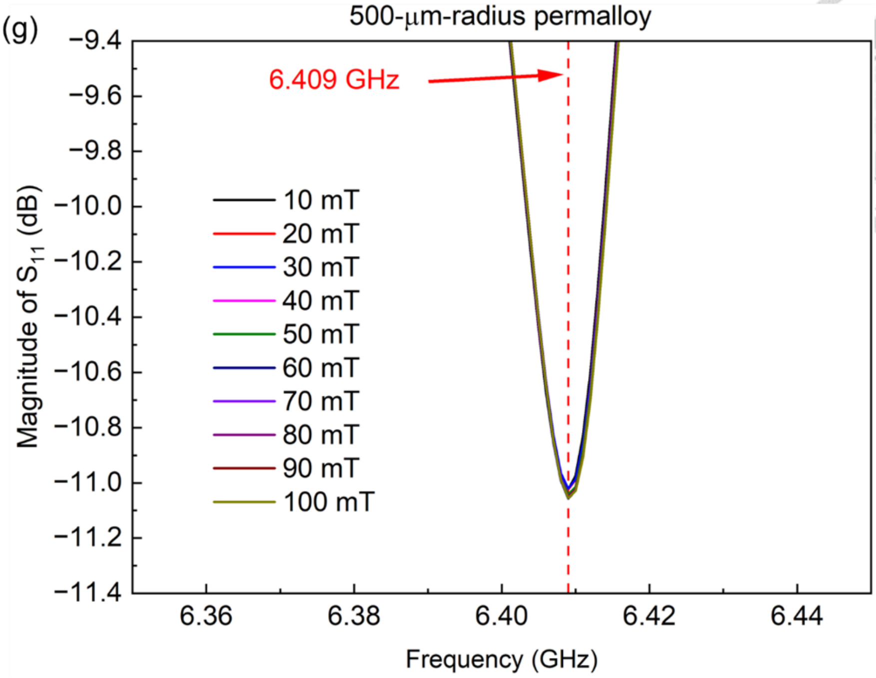

Fig. 4.48. Bias magnetic field test for higher resonance. Reproduced from [80].

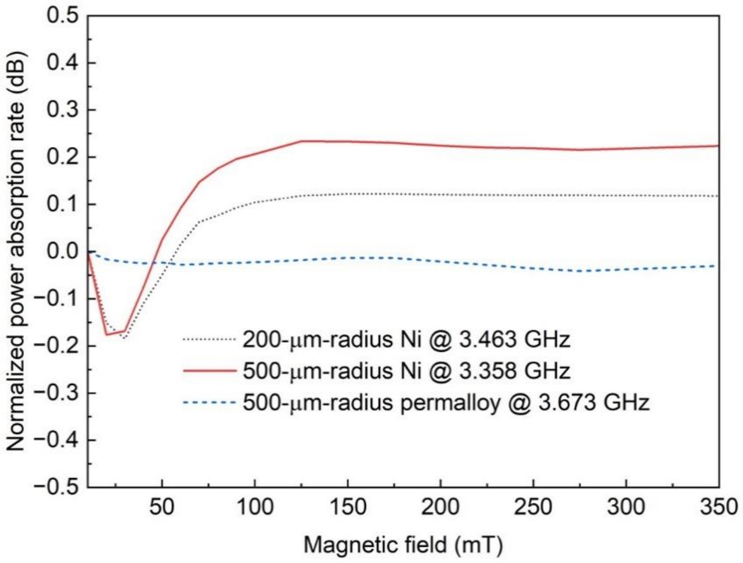

Fig. 4.49. Bias magnetic field test for lower resonance. Reproduced from [80].

unaffected by variations in the bias static magnetic field, owing to its non-magnetoelastic nature.

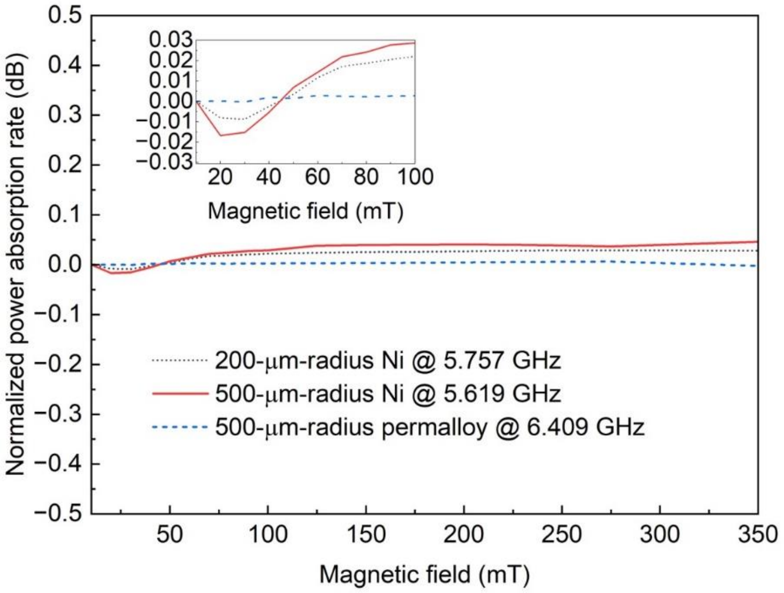

Fig. 4.50. Bias magnetic field test for higher resonance. Reproduced from [80].

To investigate how the devices respond to different bias static magnetic fields, the minimum $|S_{11}|$ value from each curve in Fig. 4.43 to Fig. 4.48 is extracted and converted into a power absorption rate using the formula $1-|S_{11}|^2$. To facilitate comparison, these values are normalized relative to their measurements at 10 mT. The resulting normalized power absorption rates, plotted against the bias static magnetic field, are shown in Fig. 4.49 and Fig. 4.20 for the lower and higher resonance frequencies, respectively.

As illustrated in Fig. 4.49, both the 200-µm and 500-µm-radius Ni devices exhibit a similar trend at the lower resonance frequency near 3.5 GHz. Their power absorption rates initially decline as the bias field increases from 10 to 30 mT, then steadily rise beyond 30 mT before reaching saturation around 100 mT. In contrast, the 500-µm-radius permalloy device shows little to no change in power absorption across the entire range of applied magnetic fields. A comparable trend is observed at the higher resonance frequency near 6 GHz, though the Ni devices exhibit a less pronounced variation in power absorption.

doi:10.6342/NTU202501094

The minimal response of the permalloy device is attributed to the nearly zero magnetostriction of $Ni_{78}Fe_{22}$, which results in negligible mechanical strain variations under the applied bias field. Consequently, unlike the Ni-based devices, the permalloy structure exhibits only slight fluctuations in power absorption. These distinct $|S_{11}|$ variations highlight the fundamental differences in dynamic behavior between magnetoelastic materials like Ni, which exhibit field-induced mechanical coupling, and non-magnetoelastic materials like permalloy, which remain largely unaffected by external magnetic fields.

Chapter 5 Multiferroic Materials for Antenna Application at GHz Band

Chapter 5 covers the experimental validation of multiferroic antenna. We also test multiferroic antenna power absorption behavior under bias magnetic field. In this chapter, a more comprehensive device test will be proposed. By adjusting the layer thickness and layer composition, related effects can be investigated more thoroughly. Due to the fabrication process constraint, the FBAR structure based on PZT materials will be considered.

5.1 Device Simulation

The multiferroic antenna is designed as a three-layer structure, with its 2D enlarged view shown in Fig. 5.1 and real scale shown in Fig. 5.2. The device simulation begins with 2D simulation to optimize the stress integration. Here the lateral size of silicon substrate is selected to the real value. The only boundary condition is the fixed one at the bottome of the susbstrate. The terminal with 1 volt is applied at the bottom of the Pt layer and ground is assigned to the Al metal. In Fig. 5.3, the simulation sweep is shown. We know that the total radiaded power of a magnetic dipole is from its magnetic moment. Since the total radiated power is propotional to the integral of magnetization over the entire Ni volume, we can optimize the radiated power by selecting maximum intetral of z-component of stress tensor, supposing that the z componenet of stress tensor T_{33} is also propotional to the magnetization M_z and z-component of stress tensor is much larger than x- and y-component.

$$P_{rad} = \frac{\mu_0}{4\pi}\frac{\omega^4}{3c^3}|m_0|^2 \qquad (6.1)$$

$$m_0 \propto abs\left(\iiint M_z \, dV\right) \propto abs\left(\iiint T_{33} dxdydz\right) \tag{6.2}$$

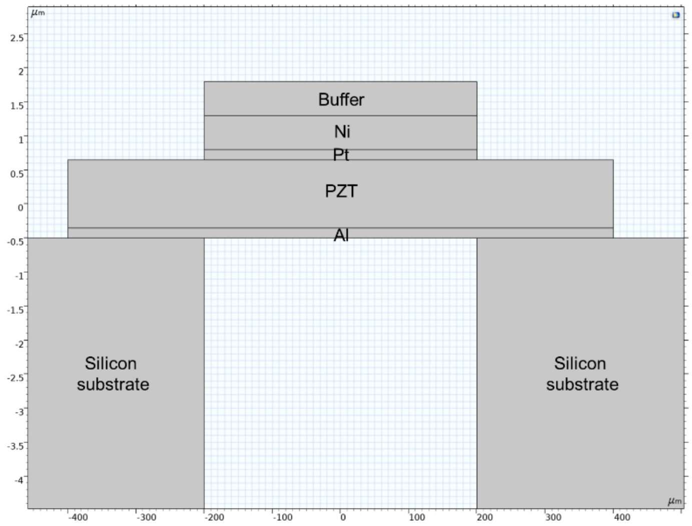

Fig. 5.1. 2D simulation model of multiferroic antenna with enlarged vertical scale.

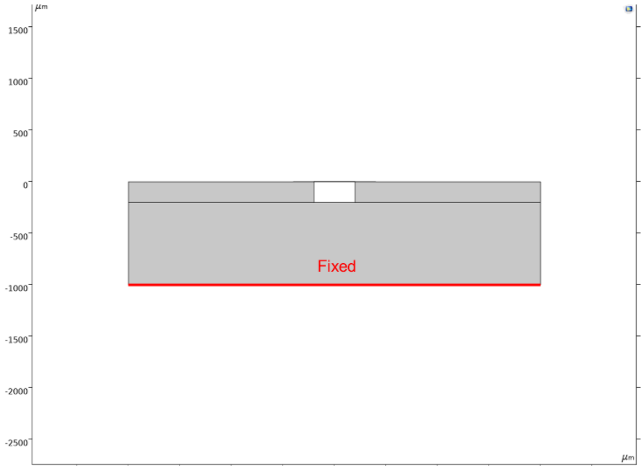

Fig. 5.2. 2D simulation model of multiferroic antenna.

From (6.1), we need to maximize the magnetic moment by maximizing the stress tensor in z-directions. At the same time, the larger the frequency the stronger the radiaed power will be. Hence, we need to select the case with highest stress integration value as well as higher resonances.

The thickness of PZT is fixed at 3 µm due to fabricaiton process limit. We sweep different combinations of Ni and buffer layer both in the range of [0.2 µm, 4 µm] at the step size of 0.2 µm with the frequency range of [0.1 GHz, 2 GHz] at th step size of 10

PZT (μm)	Ni (μm)	Buffer (μm)	Resonant frequency (MHz)	Stress integration
3	4	1.4	610	4.78906
3	3.8	1.8	610	4.63508
3	3.8	0.4	670	4.4345
3	4	2.4	310	3.86302
3	**3**	**1**	**730**	**3.7712**
3	2.6	1.8	730	3.64955
3	2.6	1.2	770	3.41173
3	2.4	1.6	770	3.18331
3	2	3.4	690	2.55448

Fig. 5.3. Thickness sweep from 0.2 μm to 4 μm.

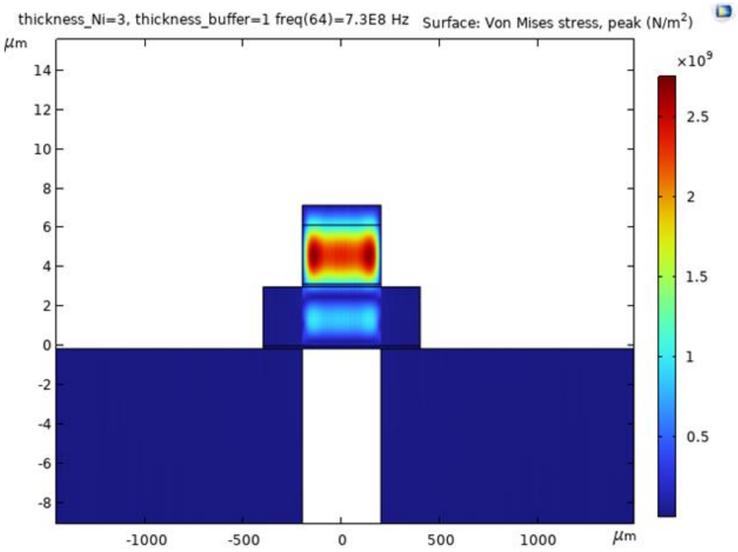

Fig. 5.4. Modal response of 730 MHz with the thickness combination of 1/3/3 μm.

MHz. Then, the peak integral results of z-component of stress tensor is identified for its mode shape, as shown in Fig. 5.3. The fifth high combinations with Buffer/Ni/PZT is 1 μm/3 μm/3 μm to resonate at 730 MHz. The modal response is shown in Fig. 5.4. This mode is the first harmonic of thickness extensional mode. It can be observed that indeed the stress is conentrated in the Ni layer to the highest stress intetration. This layer ratio is selected for its acceptable frequency and high stress integration value.

Next, we will also do the 3D simulation to validate the modal response. The simulated 3D structure is shown in Fig. 5.5 and Fig. 5.6. The symmetric boundary

doi:10.6342/NTU202501094

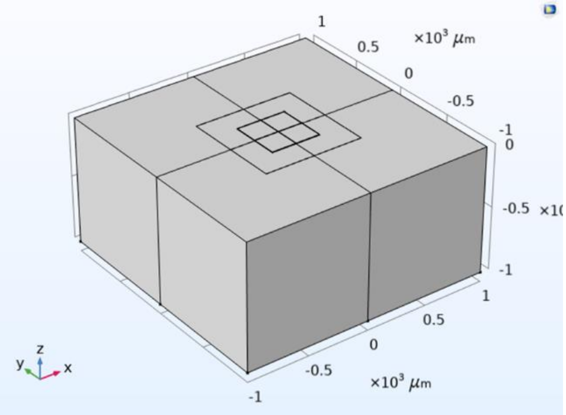

Fig. 5.5. Simulated full 3D structure in real scale.

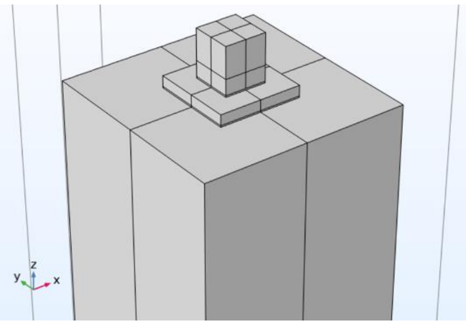

Fig. 5.6. Simulated full 3D structure in enlarged scale.

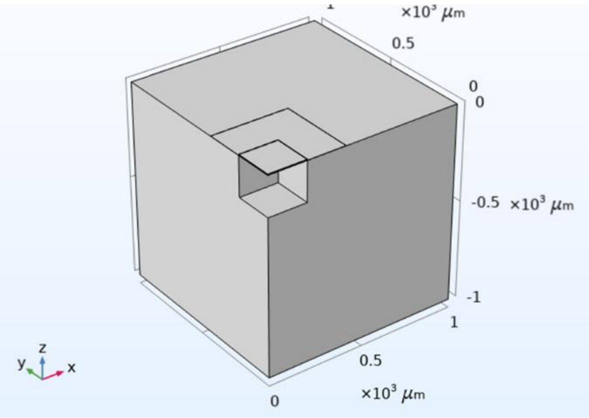

Fig. 5.7. Simulated one-fourth 3D structure in real scale.

conditions are applied at x and y plane cut. Hence, the device can be simulated in one-fourth structure to save computation resources, as shown in Fig. 5.7. The impedance respose of its magnitude and phase is shown in Fig. 5.8 and corresponding stress profile in Fig. 5.9. Indeed, the stress accumulation behavior as 2D case can be observed in 3D simulation.

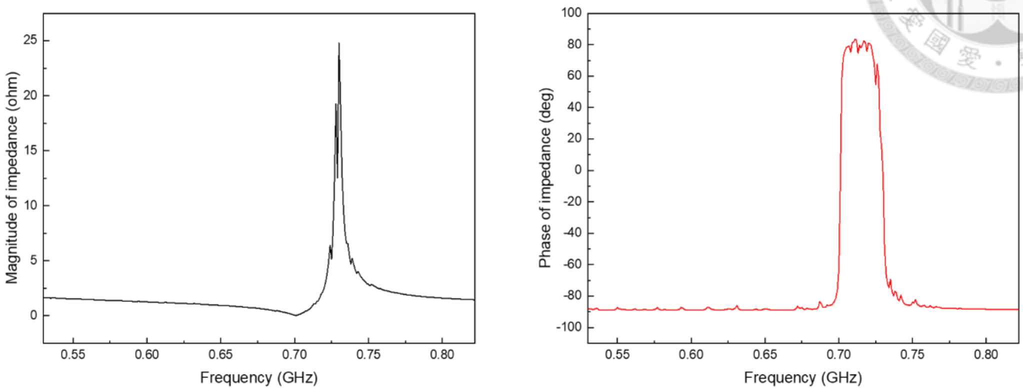

Fig. 5.8. The impedance magnitude and phase of simulated one-fourth 3D structure.

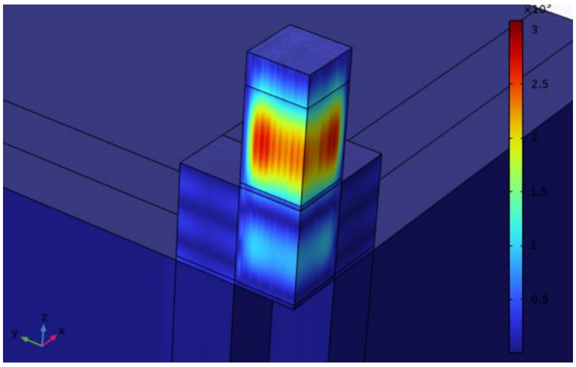

Fig. 5.9. The stress response of simulated one-fourth 3D structure.

doi:10.6342/NTU202501094

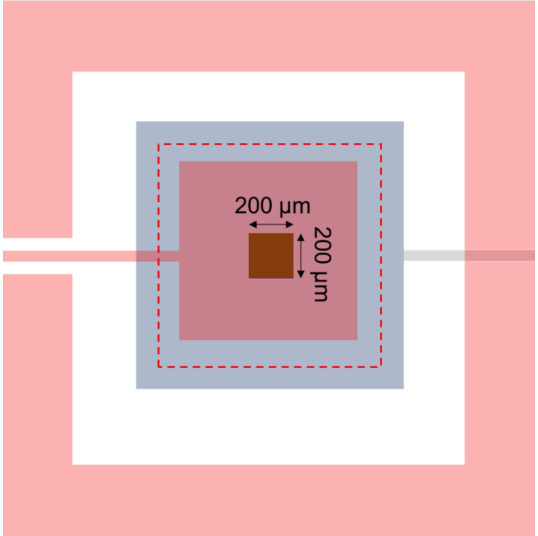

Fig. 5.10. The schematic plot of resonator design.

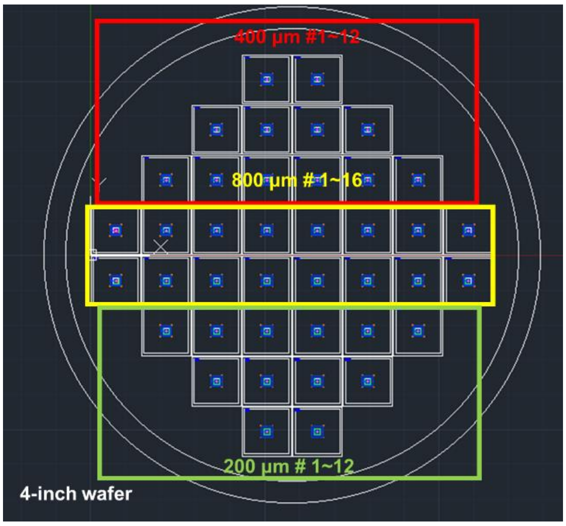

Fig. 5.11. All the testing device layout on a 4-inch wafer.

5.2 Fabrication Process

The lateral plot of resonator schematic is shown in Fig. 5.10. The pink ring is connected to GSG electrodes. The central signal is extended into top electrodes made by Pt. The ground is shorted to the grey bottom electrodes made by Pt. The light blue indicates the PZT layer and below the PZT layer indicated by the red dashed line will be the air cavity to release the device. On top of the top electrode layer will be Ni and

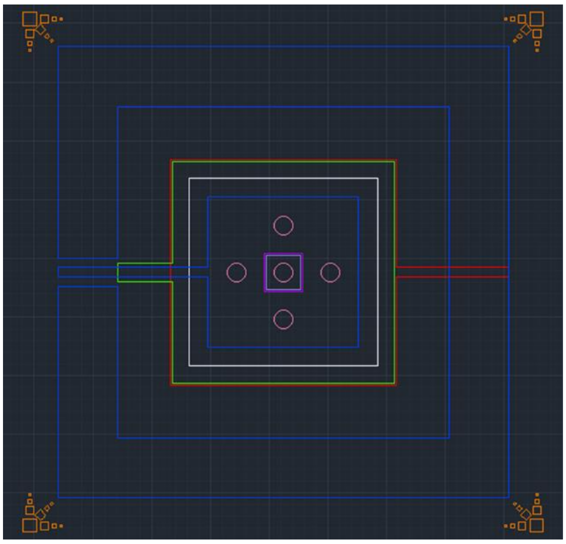

Fig. 5.12. 200 μm DUT with alignment key. The green line is the PZT layer with extra tail to prevent short circuit between signal and bottom electrode.

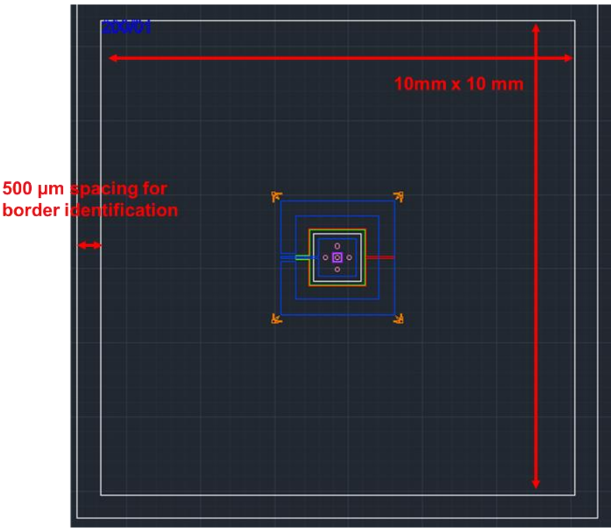

Fig. 5.13. 200 μm DUT with exterior boundary being indicated. 500 μm spacing is reserved for border identification for later mask alignment.

acoustic buffer Al_2O_3. There will be 3 versions of lateral sizes including diameters of 200 μm, 400 μm and 800 μm. The chip layout is prepared by using AutoCAD. There are several design rules to follow:

1. Misalignment uncertainty requires an extra 10 μm spacing between layers
2. Alignment key needs to be placed at four corners
3. 300 μm spacing for chip dicing

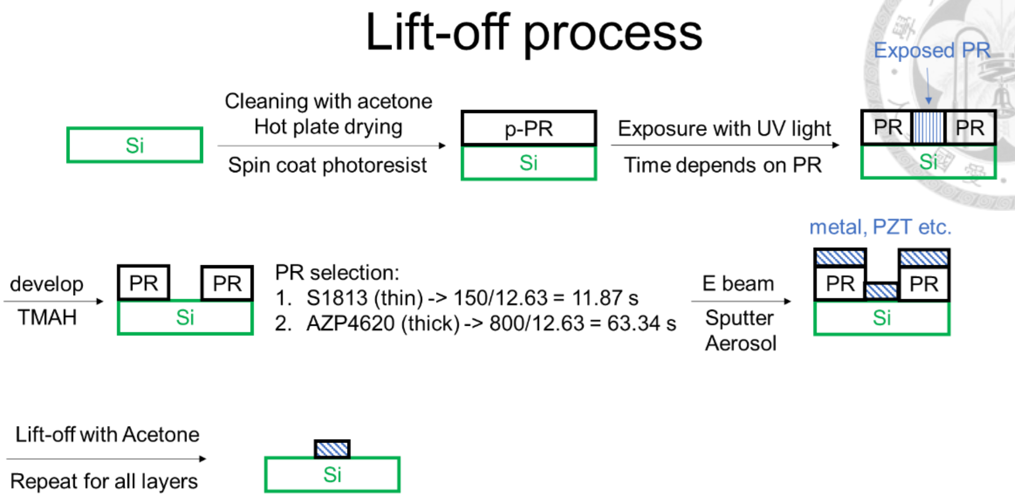

Fig. 5.14. Schematic of overall fabrication process.

4. Release via hole is reserved for possible cavity etching
5. Be careful about possible electrodes shorting contact
6. 500 μm spacing for bare silicon border identification
7. Mainly using substrate bonding for cavity formation

The finished chip on a four-inch wafer is shown in Fig. 5.11. There are 12 200-μm devices, 12 400-μm devices and 16 800-μm devices.

The overall fabrication process is based on lift-off process. The basic concept of lift-off process is shown in Fig. 5.14. The detailed process is summarized in Table 4.

Table 4. The whole lift-off process flows

#	Process step	Notes
1	Wafer cleaning (Acetone)	Put 4-inch wafer into acetone and use ultrasonic cleaner to clean for 5 minutes
2	Dehydration with N2 air gun	Make sure there is no residual water

doi:10.6342/NTU202501094

3	Dehydration on hotplate	100 degrees Celsius in 2-3 minutes
4	Spin coating with S1813 2U (recipe number 73) or AZP4620 10U (recipe number 77)	Use thinner photoresist for thinner deposited layer and thicker one for thicker deposited layer; the quantity of photoresist needs to cover at least 1/3 of overall areas
5	Soft bake the photoresist on hotplate in 110 degrees Celsius (90 seconds for S18132U and 3 minutes for AZP462010U)	
6	Attach the plastic mask and load the substrate	
7	Align and expose S1813(2u) with 12 seconds and AZP4620(10u) with 63 seconds	
8	Put the exposed dies into TAMH developer. Rinse the substrate.	S1813(2u) with 30 seconds and AZP4620(10u) with 150

doi:10.6342/NTU202501094

		seconds
9	Clean with DI water and dehydrate with N2 air gun	
10	Hard bake 3 minutes in 80 degrees Celsius	
11	Use Ebeam or Sputter to deposit metals	
12	Use Acetone to do lift-off process	
13	Repeat for the next layer	

Initially, the Pt is deposited onto the photoresist and later the Ti using S1813(2u). There are two issues found, as shown in Fig. 5.15. The Pt will crack during lift-off process due to unequal heat expansion. Also, there will be photoresist residue onto silicon substrate. Hence, the thicker AZP4620(10u) needs to be used. An additional Ti layer to connect the photoresist and Pt is needed. After applying both treatments, there will be clean and nice bottom electrode left, as shown in Fig. 5.16. Then, the Inductively Coupled Plasma Etching (ICP-RIE) will be used to etch the silicon substrate first. Additional thicker silicon will be bonded to the etched cavity, as shown in Fig. 5.17. In this way, the release via hole for the cavity etching can be prevented.

doi:10.6342/NTU202501094

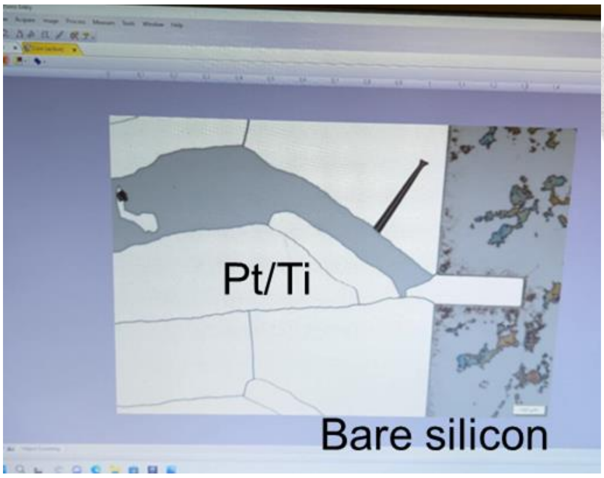

Fig. 5.15. The cracked bottom electrodes and photoresist residue.

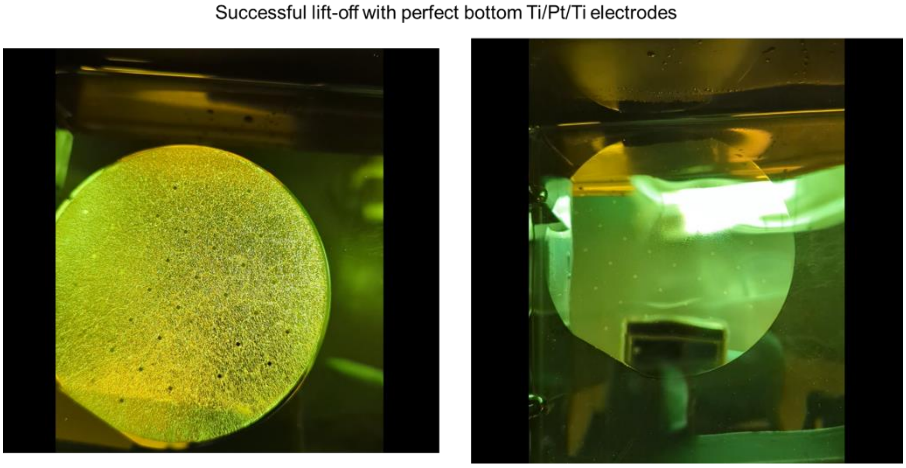

Fig. 5.16. The successful lift-off process.

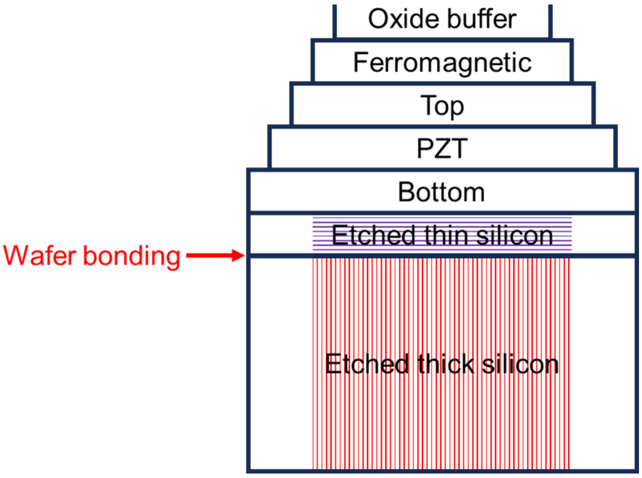

Fig. 5.17. The wafer bonding process.

5.3 Measurements

After the fabrication of multiferroic resonator, each die will be cut from silicon substrate. There will be 5 kinds of tests to be performed. First, we need to take 3D laser confocal microscope to check 3D structures. Second, SEM-EDS instruments will be performed. The composition of Ni and Permalloy will be examined again. Third, the magnetic hysterisis curve of Ni and Permalloy layer will be measured by using SQUID. We need to make sure both layers exhibit ferromagnetic behavior. Fourth, the RF probing will be used to record S parameter response with minimal parasitic effect. Finally, the DUT will be bondwired to the assembled PCB to measure the radiation pattern and its respose to the bias magnetic field.

Chapter 6 Conclusions and Future Works

The effects of replacing the magnetoelastic layer with a non-magnetoelastic (but still magnetic) material provide key insights into the fundamental mechanism of multiferroic antenna. At 3.67 GHz, the transmission characteristics remain largely unchanged, whereas at 6.42 GHz, the power absorption is noticeably reduced. Since the only structural modification is the substitution of the magnetostrictive layer, this change at 6.42 GHz can be directly attributed to the absence of magnetoelastic coupling.

If magnetoelastic interactions were the sole driver of magnetoelectric (ME) radiation, the 500-μm-radius permalloy device would not exhibit comparable transmission behavior at 3.67 GHz. This observation implies that ME radiation is influenced by factors beyond just magnetoelastic effects, though the real mechanisms require further study. Additionally, the permalloy-based device remains unaffected by variations in the applied static magnetic field, in contrast to its Ni-based counterparts. These findings suggest that the GHz-range dynamic response of magnetoelastic materials may deviate significantly from their behavior at lower frequencies. This highlights the need for deeper investigation into the fundamental mechanisms governing magnetoelectric radiation in high-frequency regimes.

The fundamental mechanism of multiferroic antenna or magnetoelectric antenna should be clarified. Fig. 6.1 illustrates the schematic of fundamental material stacking

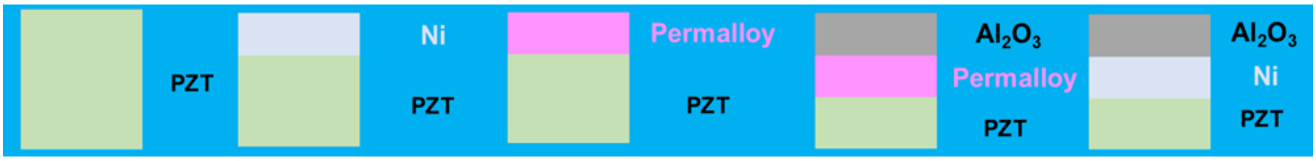

Fig. 6.1. Materials stacking combinations.

combinations currently under investigation. By adjusting the thickness, similar resonant frequencies can be achieved. This approach allows for distinguishing the effects of magnetic enhancement, parasitic influences, multiferroic radiation, and piezoelectric radiation by analyzing their transmission and reflection characteristics.

Beyond material stacking, additional factors such as electrode configuration, array design, feed-in method, and resonant modes should also be considered in future device design optimization.

References

[1] J. L. Volakis, C.-C. Chen, and K. Fujimoto, *Small antennas: miniaturization techniques & applications*. New York: McGraw-Hill, 2010.

[2] H. A. Wheeler, “Fundamental Limitations of Small Antennas,” *Proceedings of the IRE*, vol. 35, no. 12, pp. 1479-1484, 1947, doi: 10.1109/jrproc.1947.226199.

[3] L. J. Chu, “Physical Limitations of Omni-Directional Antennas,” *Journal of Applied Physics*, vol. 19, no. 12, pp. 1163-1175, 1948, doi: 10.1063/1.1715038.

[4] D. Nikolayev, M. Zhadobov, L. L. Coq, P. Karban, and R. Sauleau, “Robust Ultraminiature Capsule Antenna for Ingestible and Implantable Applications,” *IEEE Transactions on Antennas and Propagation*, vol. 65, no. 11, pp. 6107-6119, 2017, doi: 10.1109/TAP.2017.2755764.

[5] A. K. Skrivervik, “Implantable antennas: The challenge of efficiency,” presented at the 7th European Conference on Antennas and Propagation (EuCAP), Gothenburg, Sweden, Apr. 8-12, 2013.

[6] A. K. Skrivervik, M. Bosiljevac, and Z. Sipus, “Fundamental Limits for Implanted Antennas: Maximum Power Density Reaching Free Space,” *IEEE Transactions on Antennas and Propagation*, vol. 67, no. 8, pp. 4978-4988, 2019, doi: 10.1109/TAP.2019.2891697.

[7] S. A. Cummer, “Modeling electromagnetic propagation in the Earth-ionosphere waveguide,” *IEEE Transactions on Antennas and Propagation*, vol. 48, no. 9, pp. 1420-1429, 2000, doi: 10.1109/8.898776.

[8] H. Kaushal and G. Kaddoum, “Underwater Optical Wireless Communication,” *IEEE Access*, vol. 4, pp. 1518-1547, 2016, doi: 10.1109/ACCESS.2016.2552538.

[9] E.-M. Newman, “The Biggest Little Antenna in the World: The Navy’s VLF

antenna at Cutler Maine," Nov. 14, 2012. [Online]. Available: https://arlassociates.net/Newman%20AP%20Presentation.pdf

[10] J. S. McLean, "A re-examination of the fundamental limits on the radiation Q of electrically small antennas," *IEEE Transactions on Antennas and Propagation*, vol. 44, no. 5, p. 672, 1996, doi: 10.1109/8.496253.

[11] D. F. Sievenpiper et al., "Experimental Validation of Performance Limits and Design Guidelines for Small Antennas," *IEEE Transactions on Antennas and Propagation*, vol. 60, no. 1, pp. 8-19, Jan 2012, doi: 10.1109/tap.2011.2167938.

[12] A. D. Yaghjian and S. R. Best, "Impedance, bandwidth, and Q of antennas," *IEEE Transactions on Antennas and Propagation*, vol. 53, no. 4, pp. 1298-1324, 2005, doi: 10.1109/TAP.2005.844443.

[13] J. A. Bickford, A. E. Duwel, M. S. Weinberg, R. S. McNabb, D. K. Freeman, and P. A. Ward, "Performance of Electrically Small Conventional and Mechanical Antennas," *IEEE Transactions on Antennas and Propagation*, vol. 67, no. 4, pp. 2209-2223, 2019, doi: 10.1109/TAP.2019.2893329.

[14] Z. Yao, Y. E. Wang, S. Keller, and G. P. Carman, "Bulk Acoustic Wave-Mediated Multiferroic Antennas: Architecture and Performance Bound," *IEEE Transactions on Antennas and Propagation*, vol. 63, no. 8, pp. 3335-3344, 2015, doi: 10.1109/TAP.2015.2431723.

[15] Z. Yao et al., "Modeling of Multiple Dynamics in the Radiation of Bulk Acoustic Wave Antennas," *IEEE Journal on Multiscale and Multiphysics Computational Techniques*, vol. 5, pp. 5-18, 2020, doi: 10.1109/JMMCT.2019.2959596.

[16] Ting-Ta Yen, "High-Q Aluminum Nitride RF MEMS Lamb Wave Resonators and Narrowband Filters," Ph.D dissertation, College of Eng., Univ. of California, Berkeley, 2012. [Online]. Available: https://escholarship.org/uc/item/2q120220

[17] Shih-Yung Pao, Class Lecture, Waves in Piezoelectric Crystals and Acoustic Wave Devices, Institute of Applied Mechanics, National Taiwan University, Taipei, Taiwan, May. 2017.

[18] V. Kochervinskii, “Piezoelectricity in crystallizing ferroelectric polymers: Poly (vinylidene fluoride) and its copolymers (A review),” *Crystallography Reports*, vol. 48, pp. 649-675, 2003.

[19] J. F. Rosenbaum, *Bulk Acoustic Wave Theory and Devices*: Artech House, Inc., 1988.

[20] COMSOL Multiphysics. (6.0). COMSOL Inc. Accessed: Jan. 6, 2025.

[21] S. B. Krupanidhi, N. Maffei, M. Sayer, and K. Elassal, “RF planar magnetron sputtering and characterization of ferroelectric Pb(Zr, Ti)O3 films,” *Journal of Applied Physics*, vol. 54, pp. 6601-6609, 1983.

[22] Y. Sakashita, T. Ono, H. Segawa, K. Tominaga, and M. Okada, “Preparation and electrical-properties of MOCVD-deposited PZT thin-films,” *Journal of Applied Physics*, vol. 69, pp. 8352-8357, Jun 15 1991.

[23] M. Schreiter, R. Gabl, D. Pitzer, R. Primig, and W. Wersing, “Electro-acoustic hysteresis behaviour of PZT thin film bulk acoustic resonators,” *Journal of the European Ceramic Society*, vol. 24, pp. 1589-1592, 2004.

[24] T. Ikeda, *Fundamentals of Piezoelectricity*: Oxford University Press, 1990.

[25] H. Morkoç and Ü. Özgür, *Zinc Oxide: Fundamentals, Materials and Device Technology*: Wiley-VCH, 2009.

[26] S. Mishin and Y. Oshmyansky, Thin Films Deposition for BAW Devices in K. Hashimoto, *RF Bulk Acoustic Wave Filters for Communications*: Artech House, 2009.

[27] J. A. Vanvecht, “Quantum dielectric theory of electronegativity in covalent systems .3. pressure temperature phase-diagrams, heats of mixing, and distribution

coefficients," *Physical Review B*, vol. 7, pp. 1479-1507, 1973.

[28] L. I. Berger, *Semiconductor Materials*: CRC Press, 1997.

[29] R. Ruby, "Review and comparison of bulk acoustic wave FBAR, SMR technology," presented at IEEE Ultrasonics Symposium, 2007, pp. 1029-40.

[30] R. Ruby, "Review and comparison of bulk acoustic wave FBAR, SMR technology," in *Proc. IEEE Ultrasonics Symposium*, Oct. 2007.

[31] G. Piazza, P. J. Stephanou, and A. P. Pisano, "One and two port piezoelectric higher order contour-mode MEMS resonators for mechanical signal processing," *Solid-State Electronics*, vol. 51, pp. 1596-1608, Nov-Dec 2007.

[32] H. Campanella, *Acoustic Wave and Electromechanical Resonators: Concept to Key Applications*: Artech House, 2010.

[33] R. Jin, Z. Cao, M. Patel, B. Abbott, D. Molinero, and D. Feld, "An Improved Formula for Estimating Stored Energy in a BAW Resonator by its Measured S11 Parameters," presented at IEEE International Ultrasonics Symposium (IUS), Xi'an, China, Sept. 11-16, 2021.

[34] J. Larson III, P. Bradley, S. Wartenberg, R. Ruby, "Modified Butterworth-Van Dyke Circuit for FBAR Resonators and Automated Measurement System," in *Proceedings of IEEE Ultrasonics Symposium*, Oct. 22-25, 2000.

[35] K.M. Lakin, "Equivalent Circuit Modeling of Stacked Crystal Filters", in *Proc. 35th Ann. Freq. Control Symposium*, USAERADCON, Ft. Monmouth, NJ 07703, May 1981.

[36] D. Feld, R. Parker, R. Ruby, P. Bradley, S. Dong, "After 60 Years: A New Formula for Computing Quality Factor is Warranted", in *Proceedings of IEEE Ultrasonics Symposium*, Mar. 2-5, 2008.

[37] Sidhant Tiwari, "Dynamics of Multiferroic Coupling," Ph.D dissertation, College

doi:10.6342/NTU202501094

of Electrical and Computer Engineering, Univ. of California, Los Angeles, 2020. [Online]. Available: https://escholarship.org/uc/item/1s30r1kj

[38] R. C. O'Handley, *Modern Magnetic Materials: Principles and Applications*. John Wiley & Sons, Inc., 2000.

[39] H. Sohn et al., "Electrically driven magnetic domain wall rotation in multiferroic heterostructures to manipulate suspended on-chip magnetic particles," *ACS Nano*, vol. 9, no. 5, pp. 4814–4826, May 2015, doi: 10.1021/nn5056332.

[40] M. Kläui et al., "Direct observation of spin configurations and classification of switching processes in mesoscopic ferromagnetic rings," *Phys. Rev. B - Condens. Matter Mater. Phys.*, vol. 68, no. 13, p. 134426, Oct. 2003, doi: 10.1103/PhysRevB.68.134426.

[41] J. Raabe, C. Quitmann, C. H. Back, F. Nolting, S. Johnson, and C. Buehler, "Quantitative analysis of magnetic excitations in landau flux-closure structures using synchrotron-radiation microscopy," *Phys. Rev. Lett.*, vol. 94, no. 21, p. 217204, Jun. 2005, doi: 10.1103/PhysRevLett.94.217204.

[42] S. Wintz et al., "Magnetic vortex cores as tunable spin-wave emitters," *Nat. Nanotechnol.*, vol. 11, no. 11, pp. 948–953, Nov. 2016, doi: 10.1038/nnano.2016.117.

[43] H. Sohn et al., "Deterministic multi-step rotation of magnetic single-domain state in Nickel nanodisks using multiferroic magnetoelastic coupling," *J. Magn. Magn. Mater.*, vol. 439, pp. 196–202, Oct. 2017, doi: 10.1016/j.jmmm.2017.04.077.

[44] V. G. Harris, "Modern microwave ferrites," *IEEE Trans. Magn.*, vol. 48, no. 3, pp. 1075–1104, 2012, doi: 10.1109/TMAG.2011.2180732.

[45] J. D. Adam, L. E. Davis, G. F. Dionne, E. F. Schloemann, and S. N. Stitzer, "Ferrite devices and materials," *IEEE Trans. Microw. Theory Tech.*, vol. 50, no. 3, pp. 721–

737, Mar. 2002, doi: 10.1109/22.989957.

[46] W. Palmer, D. Kirkwood, S. Gross, M. Steer, H. S. Newman, and S. Johnson, “A Bright Future for Integrated Magnetics: Magnetic Components Used in Microwave and mm-Wave Systems, Useful Materials, and Unique Functionalities,” *IEEE Microw. Mag.*, vol. 20, no. 6, pp. 36–50, Jun. 2019, doi: 10.1109/MMM.2019.2904381.

[47] T. Kampfrath et al., “Coherent terahertz control of antiferromagnetic spin waves,” *Nat. Photonics*, vol. 5, no. 1, pp. 31–34, Jan. 2011, doi: 10.1038/nphoton.2010.259.

[48] V. G. Harris, “Modern microwave ferrites,” *IEEE Trans. Magn.*, vol. 48, no. 3, pp. 1075–1104, 2012, doi: 10.1109/TMAG.2011.2180732.

[49] J. D. Adam, L. E. Davis, G. F. Dionne, E. F. Schloemann, and S. N. Stitzer, “Ferrite devices and materials,” *IEEE Trans. Microw. Theory Tech.*, vol. 50, no. 3, pp. 721–737, Mar. 2002, doi: 10.1109/22.989957.

[50] W. Palmer, D. Kirkwood, S. Gross, M. Steer, H. S. Newman, and S. Johnson, “A Bright Future for Integrated Magnetics: Magnetic Components Used in Microwave and mm-Wave Systems, Useful Materials, and Unique Functionalities,” *IEEE Microw. Mag.*, vol. 20, no. 6, pp. 36–50, Jun. 2019, doi: 10.1109/MMM.2019.2904381.

[51] D. M. Pozar, *Microwave engineering*, 4th ed. Hoboken, NJ: Wiley, 2012.

[52] T.-J. Hwang, J. Lee, K. H. Kim, and D. H. Kim, "Magnetic properties and high frequency characteristics of FeCoN thin films," *AIP Advances*, vol. 6, no. 5, 2016, doi: 10.1063/1.4943358.

[53] L. Nian et al., "Demonstration of Thin Film Bulk Acoustic Resonator Based on AlN/AlScN Composite Film with a Feasible Keff2," *Micromachines*, vol. 13, no. 12, p. 2044, 2022.

[54] M. S. Sodha and N. C. Srivastava, *Microwave Propagation in Ferrimagnetics*. New York: Springer, 1981.

[55] A. G. Gurevich and G. A. Melkov, *Magnetization Oscillations and Waves*. CRC press, 1996.

[56] D. Jiles, *Introduction to Magnetism and Magnetic Materials*, 2nd ed. London, UK: Chapman & Hall, 1998.

[57] R. Eisberg and R. Resnick, *Quantum Physics of Atoms, Molecules, Solids, Nuclei, and Particles*, 2nd ed. John Wiley & Sons, Inc., 1985.

[58] G. F. Dionne, “Magnetic Relaxation and Anisotropy Effects on High-Frequency Permeability,” *IEEE Trans. Magn.*, vol. 39, no. 5 II, pp. 3121–3126, Sep. 2003, doi: 10.1109/TMAG.2003.816026.

[59] B. D. Cullity and C. D. Graham, *Introduction to Magnetic Materials*, 2nd ed. Hoboken, New Jersey: John Wiley & Sons, Inc., 2009, pp. 241-273, pp. 463-466.

[60] Z. Yao et al., “Modeling of Multiple Dynamics in the Radiation of Bulk Acoustic Wave Antennas,” *IEEE Journal on Multiscale and Multiphysics Computational Techniques*, vol. 5, pp. 5-18, 2020, doi: 10.1109/JMMCT.2019.2959596.

[61] Z. Yao, S. Tiwari, J. Schneider, R. N. Candler, G. P. Carman, and Y. E. Wang, "Enhanced Planar Antenna Efficiency Through Magnetic Thin-Films," IEEE Journal on Multiscale and Multiphysics Computational Techniques, vol. 6, pp. 249-258, 2021, doi: 10.1109/jmmct.2021.3136877.

[62] X. Cai et al., “Finite Element Analysis and Optimization of Acoustically-actuated Magnetoelectric Microantennas,” *IEEE Transactions on Antennas and Propagation*, pp. 1-1, 2023, doi: 10.1109/TAP.2023.3260651.

[63] J. P. Domann and G. P. Carman, “Strain powered antennas,” *Journal of Applied Physics*, vol. 121, no. 4, 2017, doi: 10.1063/1.4975030.

doi:10.6342/NTU202501094

[64] L. C. Ippet-Letembet, R. F. Xu, R. Jeanty, Z. Yao, R. N. Candler, and S. Y. Chen, “Modeling of Multiferroic Antennas in the Akhiezer Regime: Effects of Acoustic Resonator Excitation and Topology on Radiation,” *IEEE Transactions on Antennas and Propagation*, pp. 1-1, 2024, doi: 10.1109/TAP.2024.3481651.

[65] T. Nan et al., “Acoustically actuated ultra-compact NEMS magnetoelectric antennas,” *Nature Communications*, vol. 8, 2017, doi: 10.1038/s41467-017-00343-8.

[66] X. Yun et al., “Bandwidth-enhanced magnetoelectric antenna based on composite bulk acoustic resonators,” *Applied Physics Letters*, vol. 121, no. 3, 2022, doi: 10.1063/5.0098323.

[67] X. Liang et al., “Mechanically Driven Solidly Mounted Resonator-Based Nanoelectromechanical Systems Magnetoelectric Antennas,” *Advanced Engineering Materials*, vol. 15, no. 21, 2023, doi: https://doi.org/10.1002/adem.202300425.

[68] B. Luo, X. Liang, H. Chen, N. Sun, H. Lin, and N.-X. Sun, “Gain Enhancement and Ground Plane Immunity of Mechanically Driven Thin-Film Bulk Acoustic Resonator Magnetoelectric Antenna Arrays,” *Advanced Functional Materials*, vol. 34, no. 39, 2024, doi: https://doi.org/10.1002/adfm.202403244.

[69] M. Ma et al., “High-Frequency Magnetoelectric Antenna by Acoustic Excitation for 5G Communication,” *IEEE Antennas and Wireless Propagation Letters*, vol. 23, no. 5, pp. 1518-1522, 2024, doi: 10.1109/LAWP.2024.3360947.

[70] T. Nan, Y. Hui, M. Rinaldi, and N. X. Sun, “Self-Biased 215MHz Magnetoelectric NEMS Resonator for Ultra-Sensitive DC Magnetic Field Detection,” *Scientific Reports*, vol. 3, no. 1, 2013, doi: 10.1038/srep01985.

[71] X. Yun et al., “Biaxial film bulk acoustic resonator magnetic sensor based on the

Fe80Ga20 anisotropic ΔE effect," *Journal of Physics D: Applied Physics*, vol. 55, no. 13, p. 135002, 2022, doi: 10.1088/1361-6463/ac4452.

[72] B. Spetzler, E. V. Golubeva, C. Müller, J. McCord, and F. Faupel, "Frequency Dependency of the Delta-E Effect and the Sensitivity of Delta-E Effect Magnetic Field Sensors," *Sensors*, vol. 19, no. 21, p. 4769, 2019. [Online]. Available: https://www.mdpi.com/1424-8220/19/21/4769.

[73] D. Labanowski, A. Jung, and S. Salahuddin, "Power absorption in acoustically driven ferromagnetic resonance," *Applied Physics Letters*, vol. 108, no. 2, p. 022905, 2016, doi: 10.1063/1.4939914.

[74] D. Labanowski, A. Jung, and S. Salahuddin, "Effect of magnetoelastic film thickness on power absorption in acoustically driven ferromagnetic resonance," *Applied Physics Letters*, vol. 111, no. 10, 2017, doi: 10.1063/1.4994933.

[75] D. Labanowski et al., "Voltage-driven, local, and efficient excitation of nitrogen-vacancy centers in diamond" *Science Advances*, vol. 4, no. 9, 2018, doi: doi:10.1126/sciadv.aat6574.

[76] D. Milyutin, S. Gentil, and P. Muralt, "Shear mode bulk acoustic wave resonators based on c-axis oriented AlN thin film," *J. Appl. Phys.*, vol. 104, Oct. 2008.

[77] D. Chen, J. Wang, D. Li, L. Zhang and X. Wang, "The c-axis oriented AlN solidly mounted resonator operated in thickness shear mode using lateral electric field excitation," *Appl. Phy. A*, vol. 100, pp. 239-244, Mar. 2010.

[78] C. A. Balanis, *Antenna Theory: Analysis and Design*. New Jersey, USA: John Wiley & Sons, 2005.

[79] R.-F. Xu, "Broadband Polarization Control of Bulk Acoustic Wave-Mediated Multiferroic Antenna Based on Thickness Shear Modes," M.S. thesis, College of Elec. Eng. and Comput. Sci., National Taiwan Univ., Taipei, 2019.

[80] R.-F. Xu et al., “Experimental validation of multiferroic antennas in GHz frequency range,” *Applied Physics Letters*, vol. 123, no. 16, 2023, doi: 10.1063/5.0165393.

doi:10.6342/NTU202501094